PERFUSION IMAGING USING POWER DOPPLER ULTRASOUND WITHOUT CONTRAST ENHANCEMENT TO DIAGNOSE PERIPHERAL ARTERY DISEASE

BY

SOMAYE BABAEI

DISSERTATION

Submitted in partial fulfillment of the requirements
for the degree of Doctor of Philosophy in Bioengineering
in the Graduate College of the
University of Illinois Urbana-Champaign, 2024

Urbana, Illinois

Doctoral Committee:

Professor Michael Insana, Chair
Professor Brad Sutton
Professor Wawrzyniec Dobrucki
Associate Professor Heidi Phillips
Assistant Professor Fan Lam
Teaching Professor Jenny Amos

Abstract

This thesis delves into the exploration of non-contrast Power-Doppler ultrasound (PD-US) for monitoring blood perfusion in peripheral tissues, with a specific focus on its ability to track spatiotemporal changes in muscle perfusion. The research initiates with a thorough investigation of spatial registration techniques combined with Principal Components Analysis (PCA)-based clutter filtering. This approach substantially improves the efficiency of narrowing the eigen-spectrum of tissue clutter, optimizing the efficacy of PCA filters. It is imperative to note that the success of the clutter filter hinges on the spatial patterns of blood cell motion. The results demonstrate a successful reduction of in-plane clutter motion, enhancing the overall precision of the imaging process. However, challenges associated with out-of-plane movement persist, resulting in clutter-filter leakage. These issues can be addressed through simple adjustments in scanning techniques and implementing spatial averaging procedures.

The scope of the study expands to validate PD-US measurements through a comparative analysis with laser speckle contrast imaging (LSCI) in pre-clinical rodent studies. The combination of spatial registration and clutter filtering techniques enables consistent tracking of blood perfusion in skeletal muscle while modulating hindlimb blood flow. The research encompasses invasive and non-invasive studies, with PD-US measurements compared with LSCI under various conditions, including short-term arterial clamping and prolonged hindlimb ischemia induction. Simultaneous B-mode imaging and PD-US are employed to assess flow-mediated dilation (FMD) of the femoral artery and downstream muscle perfusion, quantifying reactive hyperemia (RH). Measurements are conducted on adult male and female mice and rats, including those subjected to exercise conditioning, to explore potential biological variables. The results validate the efficacy of non-contrast PD-US through comparisons with LSCI, revealing no significant differences between sexes or fitness levels in FMD or RH estimates. Encouragingly, post-ischemic perfusion improvements are observed with exercise conditioning, suggesting variations in hyperemic responses between the conduit and resistive vessels.

The research further examines the effectiveness of PD-US for monitoring shifts in muscle perfusion over time, emphasizing changes relevant to biological variables, specifically diabetes. Experiments include the induction of short and long-term ischemia in healthy and type II diabetic male and female mice, with and without exercise. Perfusion measurements are taken during and after 5-minute ischemic periods and throughout four-week recovery phases following irreversible femoral ligation. The results reveal differences in perfusion recovery times between diabetic and non-diabetic mice. Additionally, measurements of FMD in conduit arteries and the RH index in resistive vessels indicate a decline in sedentary diabetic mice compared to sedentary non-diabetic mice. The reproducibility of perfusion measurements is primarily affected by the ability to consistently select the same muscle region and effectively filter out tissue clutter. This study underscores the capability of PD-US measurements to accurately track site-specific changes in skeletal muscle perfusion over time, particularly in the context of diabetes. These findings offer promise in addressing the

crucial need for techniques to monitor atherosclerotic changes leading to ischemic cardiovascular pathologies regularly.

Extending beyond murine models, this research adopts a translational approach with porcine subjects. The method utilizes a low-frequency ultrasound pulse and a handheld transducer to explore muscle perfusion at greater depths. An ischemia model induced by an ameroid ring constrictor (ARC) is introduced, emphasizing gradual arterial constriction, resembling the extended development of atherosclerosis in peripheral artery disease (PAD) patients, in contrast to the acute ligation often used in murine models. The results confirm that PD-US, without contrast enhancement, effectively monitors temporal changes in a human-scale phantom using low-frequency probes.

In conclusion, these findings support the advancement of non-contrast PD-US as a robust tool for assessing blood perfusion alterations and enhancing patient care in the context of peripheral artery disease.

To my parents and my husband.

Acknowledgments

I am overwhelmed with gratitude for my incredible journey, and I owe a debt of appreciation to so many who've been a part of it.

First and foremost, I want to express my deepest thanks to Professor Michael Insana, my research advisor. His support and guidance have been the bedrock of my academic journey. His passion and encouragement have been more than just words; they've been a profound source of inspiration that has enriched my perspective on this research. His mentorship has been nothing short of transformative, shaping me into the researcher I am today. To my committee members, Professors Brad Sutton, Wawrzyniec Dobrucki, Heidi Philips, Fan Lam, and Jenny Amos, I extend my sincere gratitude. Their insights, challenging questions, and thought-provoking discussions have significantly improved my thesis research quality. Prof. Craig Abbey at the University of California Santa Barbara deserves special mention. His thoughtful advice has been a guiding light during my research journey.

My fellow lab mates, past and present, have been an invaluable part of this journey. Dr. Cameron Hoerig, Dr. Yang Zhu, Dr. Yiliang Wang, Bingze Dia, and Will Newman have been more than just colleagues; they've provided continuous support and helped foster an inspiring and innovative lab environment. Denise Medina Almora, Yamenah Ambreen, Leopold Pinot, Michael Nelappana, and Lainey Nielsen in the Molecular Imaging Lab have been instrumental in my research with their unwavering help and support. Special thanks to Mingxiao Zhang in the Magnetic Resonance Functional Imaging Lab for his assistance with MRI segmentation. Our collaboration has made every day in the lab unforgettable. I'm grateful to my friends who've shared in the joys and challenges of this journey. Your camaraderie has been a treasured part of my life.

I owe my deepest gratitude to my family – my parents, Alimohammad and Mahvash, and my siblings, Fatameh, Zahra, and Mohammadreza. Your love, smiles, and encouraging words have been a constant source of positivity. I deeply respect and love each one of you. Last but not least, I extend heartfelt thanks to my beloved husband, Abbas. His unwavering love and support have been my anchor during the highs and lows of the past several years.

I would like to acknowledge the invaluable assistance of Grammarly and ChatGPT in editing and refining this thesis.

Research reported in this publication was supported by the National Institutes of Health (NIH) under Award Numbers R01 HL148664.

Table of contents

List of Abbreviations

ABI	Ankle Brachial Index.
AUC	Area Under the curve.
ANCOVA	Analysis OF Covariance.
ARC	Ameroid Ring Constrictor.
BPM	Beat Per Minute.
BTCR	Blood To Clutter Ration
CF	Color Flow.
CTA	Computed Tomographic Angiography.
CV	Coefficient of Variation.
DE	Diabetic Exercised.
DS	Diabetic Sedentary.
DV	Dependent Variable.
ENV	Envelope.
FMD	Flow Mediated Dilation.
fps	Frames Per Second.
HFD	High Fat Diet.
HE	Healthy Exercised.
HS	Healthy Sedentary.
IM	Intramuscular.
IQ	In-phase and Quadrature.
IDV	Independent Variable.
IV	Intravenously.
LSCI	Laser Speckle Contrast Imaging.
MRA	Magnetic Resonance Angiography.
NIR	Near Infrared.

NO	Nitric Oxide.
NOS	Nitric Oxide Synthase.
PAD	Peripheral Artery Disease.
PCA	Principal Component Analysis.
PD	Power Doppler.
PD-US	Power Doppler Ultrasound.
PRF	Pulse Repetition Frequency
RBC	Red Blood Cell.
RH	Reactive Hyperemia.
RH-PAT	Peripheral Arterial Tonometry.
RF	Radio Frequency.
ROI	Region of Interest.
RR	Respiratory Rate
SD	Standard Deviation.
SE	Standard Error.
SVD	Singular Value Decomposition.
SNR	Signal to Noise Ratio.
SSF	Spatial Sensitivity Function.
STZ	Streptozotocin.
US	Ultrasound.

List of Symbols

α	Scaling Factor.
β	Scattering Amplitude for Blood.
c	Speed Of The Sound.
d	Displacement.
δ	Dirac Delta Function.
D	Diameter of the Vessel.
Δ_k	Axial Displacements.
Δ_l	Lateral Displacements.
ϵ_{klm}	Band-pass White Gaussian Noise.
f	Object Function.
g_{klm}	Sampled Time Series.
h_G	Gabor Approximation.
h_s	Spatial Sensitivity Function.
K_X	Temporal Covariance.
λ	Eigenvalues.
M	Echo Frames.
p	Tissue Reflector.
q	Blood Reflector.
ρ	Correlation Coefficient.
σ_x	Lateral Pulse Width.
σ_z	Axial Pulse Width.
t	Time.
t_k	Fast Time Variable.
τ	Scattering Amplitude for Tissue.
θ	Doppler Angle.

u_0	Carrier Frequency.
u	Doppler Frequency.
v_p	Tissue Velocity.
v_q	Blood Velocity.
φ	Phase.
Ω	Imaging Region.
$\mathcal{F}\{\cdot\}$	Forward Fourier Transform.
$\mathcal{F}^{-1}\{\cdot\}$	Inverse Fourier Transform.

Chapter 1

Introduction

1.1 Motivation

Blood flow patterns play a crucial role in the diagnostic landscape of cardiovascular disorders, providing profound insights into the underlying pathophysiological mechanisms. Employing advanced methodologies such as Doppler ultrasound (US), computed tomographic angiography (CTA), and magnetic resonance angiography (MRA), medical practitioners and researchers acquire the capability to intricately analyze blood flow characteristics encompassing velocity, direction, and turbulence within the cardiovascular system. A significant contribution is made toward identifying a diverse spectrum of clinical conditions by consistently and longitudinally monitoring these dynamic circulatory alterations. This range encompasses not only metabolic disorders like diabetes but also regional ischemia, systemic cardiovascular afflictions, and the progression of tumors. This discerning assessment of flow patterns empowers healthcare professionals with the essential instruments to identify emerging disease states promptly, customize patient-specific treatment approaches, and diligently oversee the evolution of cardiovascular pathologies. Inadequate blood flow within the lower limbs (ischemia) manifests as pain, an early indication of Peripheral Artery Disease (PAD) [1].

1.1.1 Peripheral Artery Disease (PAD)

PAD arises from atherosclerosis, culminating in obstructions within the arteries and arterioles of the lower extremities [2]. This condition is closely linked to risk factors such as smoking, diabetes, hyperlipidemia, and hypertension [3], each of which contributes to the development of endothelial dysfunction, fostering atherogenic processes. The global prevalence of PAD surpasses 200 million individuals [4] and exhibits a pronounced correlation with coronary artery disease, stroke, and cardiovascular mortality [5][6][7]. Treatment approaches span a spectrum contingent upon PAD severity, ranging from lifestyle adjustments to peripheral vascular bypass surgery. Due to the gradual advancement of initial PAD symptoms, often resembling other prevalent conditions among elderly individuals, a demand arises for efficient, noninvasive methodologies to image perfusion within the upper and lower limb musculature.

1.1.2 Contemporary Diagnostic Approaches for PAD

Currently, conducting a comprehensive clinical evaluation of PAD entails measurements of the ankle-brachial index (ABI), coupled with subsequent MR or CT angiography aimed at detecting vascular occlusions [8].

The ABI is computed as the ratio of maximal bilateral systolic blood pressure values in the lower and upper extremities [9]. Interpretation of ABI values, however, presents challenges, as age and metabolic conditions can elevate ABI above 1.3, yielding an uncertain diagnosis [10].

1.1.3 Problem Identification and Research Objectives

The feasibility of measuring microvasculature flow in the lower extremities lies in applying molecular imaging probes. This involves integrating contrast agents with optical [11][12], nuclear [13], MR [14], or US [15][16] imaging modalities to enhance the sensitivity and specificity of detecting blood cells within vascular spaces. While each technique effectively caters to distinct clinical demands, concerns regarding risk and cost have hindered their widespread utilization. The inclination leans towards achieving perfusion imaging without the need for contrast agents, provided it fulfills criteria encompassing reliability, affordability, minimal risk, and broad accessibility.

In this framework, Laser Doppler techniques emerge as secure and cost-effective alternatives for real-time surface perfusion imaging. Nonetheless, their potential is limited due to their capacity to measure depth, which typically extends to depths of only 1 to 2 mm [17]. On the other hand, conventional Power Doppler Ultrasound (PD-US) demonstrates sensitivity to red blood cell (RBC) movements in vascular beds. It offers superior depth penetration capabilities and real-time processing features. However, its applicability for clinical perfusion estimation is compromised due to the considerably weaker echoes produced by blood cells compared to tissue (Clutter) echoes, further compounded by their similar velocity ranges.

Tissue Motion Profiling

Tissue movement is primarily attributed to two sources: the motion of the sonographer's hand and physiological shifts in the patient, both of which currently limit the effectiveness of this technique in the absence of contrast enhancement [18]. When dealing with faster flows within noticeable blood vessels, the spectral components of the blood and clutter signals can be differentiated. Conversely, as blood flow velocities decrease, such as in capillary beds, or when there is significant tissue motion, the spectra of blood flow and clutter begin to overlap. This overlapping of spectra introduces complexity to separating blood and clutter based on temporal information. Several researchers have introduced an alternate proposition suggesting that the distinct spatial attributes of tissue and blood signals enable their separation. They posit that red blood cell scatterers exhibit significantly greater deformability than tissue, leading to noticeable spatial decorrelation in the echo signal. As a result, tissue signals display heightened spatial coherence compared to blood signals. This hypothesis has paved the way for a new category of singular value decomposition (SVD)-based clutter filtering methods [19][20][21][22][23].

Singular Value Decomposition (SVD)

PCA filters, derived from principal components analysis, are effective for separating clutter and blood echoes in peripheral perfusion imaging. Echo data is arranged in a matrix structure with spatial and temporal samples. Using SVD, these matrices generate singular values. Effective clutter filters are constructed by discarding initial singular values and calculating residual signal power. Assumptions include:

1. Stable tissue echoes
2. Weakly scattered blood echoes

3. Strong signal-to-noise ratios.

Despite these assumptions, practical clutter filtering is often incomplete. Therefore, a shift in focus occurred toward evaluating the clinical scanning environment. The primary goal of this research project is to develop novel PD- US without contrast enhancement acquisition and clutter filtering methods that provide consistent maps of blood-cell perfusion in peripheral muscle. Our proposed solution is centered around developing a three-dimensional blood perfusion model, serving as the foundational framework for a comprehensive assessment of the contributions made by individual measurement components and their corresponding assumptions to the PD-US signal [24]. This endeavor has yielded two notable accomplishments:

- **Firstly,** the introduction of a streamlined and precise rigid spatial registration technique, strategically employed to optimize echo conditioning;
- **Secondly,** the derivation of an echo correlation coefficient estimate, which assumes the role of a benchmark for assessing the efficacy of clutter filtering.

1.2 Main Results

We illustrated our consistent ability to accurately isolate slow-moving blood from tissue echoes and noise through a three-step process:

1. **Method Validation:** Initially, we establish the effectiveness of our methodology. This endeavor begins by subjecting PD-US techniques to a thorough evaluation involving tests that explore their boundaries via simulations and experiments utilizing phantom configurations. Simulations confirmed that spatial registration narrows the bandwidth of the clutter subspace, resulting in a more distinct threshold for effectively segregating the blood and clutter subspaces. Following this, we further substantiated the reliability of our techniques through In vivo evaluations. This entails the utilization of Laser Spackle Contrast Imaging (LSCI, the current validated modality for perfusion imaging) and a well-established animal model for in vivo assessments. Additionally, our validation process incorporates a comparative analysis of our outcomes against established findings in the existing literature. Through a comparative evaluation of PD-US outcomes alongside those from LSCI and pre-existing literature, we substantiated the capability of our proposed approach to accurately track the progression of perfusion patterns across time.

2. **Diagnostic Evaluation:** Moreover, we delved into the potential of PD-US to detect shifts in perfusion, considering influential biological factors. In pursuit of this objective, we employed a unilateral ischemic hindlimb model developed by the Dobrucki lab. This model serves as a platform for investigating perfusion dynamics in healthy and diabetic mice. To explore our method's diagnostic capacity, we meticulously tracked alterations in perfusion within the ischemic muscle in relation to the non-ischemic contralateral control hindlimb. This comprehensive study spanned four weeks and contained eight distinct mouse groups. These groups were characterized by variations in gender, health status (healthy or diabetic), and activity level (sedentary or exercise-conditioned). The results showed that PD-US measurements exhibit the capability to accurately track localized alterations in skeletal muscle perfusion due to diabetes, addressing the requirement for methods that can consistently monitor the progression of atherosclerotic changes that culminate in ischemic cardiovascular conditions.

3. **Human–Scale Adaptation:** Finally, we extend our measurements to encompass human-scale proportions, as the larger scale introduces complexities related to penetration, attenuation, reduced signal-to-noise ratio (SNR), and notable clutter motion. This transition to dimensions resembling those encountered in clinical settings brings us closer to approximating the challenges faced during general clinical scanning. We employed a pig model through a collaborative effort involving the Dobrucki, Sutton, and Phillips labs to achieve this objective. In this context, we introduced an ameroid constrictor ring around the right femoral artery of a pig. This setup aimed to replicate the effects of gradual occlusion, aligning more closely with the gradual progression of PAD seen in diabetic patients. This adjustment to the pace of PAD progression in a pig model enhances the relevance of our measurements to clinical scenarios where such challenges are encountered.

1.3 Summary of Chapters

The dissertation's core contribution lies in improving the sensitivity and specificity of perfusion imaging using PD-US technology through offline clutter filtering. This research project is entirely devoted to the advancement of non-contrast-enhanced PD-US techniques for peripheral perfusion imaging. Our paramount goal is the development of acquisition methods followed by rigid registration and SVD clutter filter as a clutter filtering method, leading to the consistent mapping of blood-cell perfusion in peripheral muscle tissues. The following outlines the structure of the thesis:

Chapter 2: Development of a PD-US Echo Simulator

This chapter focuses on developing an echo simulator designed explicitly for blood perfusion imaging using PD-US. The chapter provides an in-depth look at the registration and filtering techniques used in PD-US imaging for blood perfusion. The validity of the simulation is supported by a comprehensive experimental phantom study.

Chapter 3: Pre-clinical Investigation on Muscle Perfusion

Chapter three presents a pre-clinical study aimed at demonstrating the capability of PD-US measurements in detecting temporal changes in peripheral muscle perfusion. Due to the unavailability of realistic phantoms for experimentation, the study utilizes rodent hindlimbs, employing invasive and non-invasive methods to temporarily modulate blood flow. The goal is to assess the effectiveness of PD-US in capturing dynamic changes in muscle perfusion and its potential application in monitoring such alterations.

Chapter 4: Diabetic-Related Changes in Perfusion

This chapter extensively explores alterations in perfusion related to biological factors, especially diabetes, in response to long and short-term ischemic conditions. It specifically investigates parameters such as the maximum perfusion loss following femoral ligation, the duration required for complete perfusion recovery, and the measurement of hyperemia response in both resistive and conduit vessels for identifying endothelial dysfunction. The study underscores the remarkable sensitivity of PD-US imaging to changes associated with diabetes in mice, offering promising prospects for monitoring peripheral perfusion in clinical settings.

Chapter 5: Advancing PAD Understanding with a Pig Model

Chapter five builds upon previous mice-model studies and introduces enhancements in understanding PAD. It employs a pig-model approach, incorporating a 5-MHz ultrasound pulse and a handheld probe for deeper muscle perfusion assessment. An ameroid ring constrictor (ARC) is surgically placed on the femoral artery, inducing gradual muscle ischemia, more closely resembling the development of atherosclerosis in PAD patients.

Chapter 6: Conclusion

The final chapter summarizes the key findings and insights from the preceding chapters, highlighting the potential of PD-US in blood perfusion imaging for both clinical and research applications. The research presented in this thesis contributes to the development of non-invasive, cost-effective methods for early detection and monitoring of PAD, intending to improve patient outcomes and the management of this prevalent vascular condition.

Chapter 2

Simulation and Validation of Blood Perfusion Imaging with PD-US

2.1 Study Overview

The clinical applicability of Perfusion PD-US imaging, devoid of contrast enhancement, heavily relies on the efficient removal of clutter, ensuring that the acquired images accurately represent the echoes produced by slow-moving blood cells within the microvasculature. Principal Component Analysis (PCA) has emerged as a standard technique for constructing clutter filters based on the observed ultrasonic Doppler acquisition signals [20] [25] [26] [27]. PCA filters are remarkably effective in eliminating the signal power originating from tissue echoes, particularly in situations where weak blood echoes are the primary source of decorrelated-echo signals. This effectiveness is most pronounced when blood cells perfuse tissues that remain stationary with respect to the US beam. In such cases, signals from static tissue echos, although strong, exhibit a high degree of correlation between echo frames in the ensemble. This correlation enables PCA filters to efficiently distinguish them from the weaker, decorrelated echoes resulting from the motion of blood cells within the PCA spectrum. As the subspaces for these two echo sources diverge, the PCA filter effectively removes clutter, leaving only the signal power originating from the movement of blood cells and background noise.

In this chapter, we delve into developing an echo simulator tailored to the context of blood perfusion imaging using Power-Doppler Ultrasound (PD-US). We present a comprehensive overview of the registration and filtering techniques employed in the context of PD-US imaging of blood perfusion. Furthermore, we substantiate the validity of our simulation through an extensive experimental phantom study. [28].

2.2 Method

2.2.1 Perfused Tissue Model

To faithfully replicate echo-signal frames acquired from perfused tissues scanned with a linear array transducer, we adopt a discrete scatterer model. This model, which has been described in literature [29], allows us to simulate the behavior of point reflectors within a clear gel representing the biological tissue. These point reflectors are strategically placed within the gel, and they move freely between frames. Each individual scatterer is characterized as a 3-D Dirac delta function $\delta(x - x_n)$ situated at the spatial coordinates $x_n = (x, y, z)_n$. It

is worth noting that the position of each scatterer is not static but varies with time, $x_n = x_n(t)$. This dynamic aspect is essential, as it mirrors the movement of scatterers in response to the incident sound beam. The scattering field arising from these scatterers is mathematically represented by the object function, denoted as f, which varies with both spatial coordinates x and time t. This function is defined as:

$$f(x,t) = \sum_{n\in\Omega} a_n \delta(x - x_n(t)) \tag{2.1}$$

Here, a_n corresponds to the reflectivity of the nth scatterer, and $x_n(t)$ represents the dynamic spatial position of each scatterer within the image. This formulation allows us to model the behavior of point reflectors as they move in response to the US beam. Furthermore, our object function f can be further divided into two components, representing tissue and blood scatterers, respectively. This separation is defined as:

$$f(x,t) = f_\tau(x,t) + f_\beta(x,t) = \sum_{p\in\Omega} \tau\delta\left(\mathbf{x} - \mathbf{x}_p(t)\right) + \sum_{q\in\Omega} \beta\delta\left(\mathbf{x} - \mathbf{x}_q(t)\right) \tag{2.2}$$

Here, f_τ and f_β represent the scattering contributions from tissue and blood reflectors, respectively. The scattering amplitudes for tissue and blood reflectors are denoted as τ and β, respectively, and are considered constant within the imaging region Ω. The spatial positions of tissue and blood reflectors are denoted as $x_p(t)$ and $x_q(t)$, respectively, and n collectively represent the sets of tissue (p) and blood (q) reflectors. This framework provides a comprehensive representation of the scattering behavior within our US imaging system, enabling us to analyze and differentiate between tissue and blood components during image reconstruction.

2.2.2 Echo Signal Model

The signal model transforms the scatterer function described in Equation 2.1 into a time series of simulated 2-D radiofrequency (RF) echo frames. This transformation is achieved through the utilization of the spatial sensitivity function (SSF), denoted as $h_S(x)$, which characterizes the contributions of scatterers at different spatial positions to each sample of the RF signal. The SSF is fundamentally the pulse-echo impulse response function, denoted as $h(x,t)$, for a fixed measurement time, i.e., $h_S(\mathbf{x}) \triangleq h(\mathbf{x} \mid t)$ [29], [30]. This response function encompasses the three-dimensional spatial sensitivity of our imaging system, allowing for contributions to the echo signal from scatterers located at lateral (x), elevational (y), and axial (z) positions relative to the US beam axis. A critical assumption in our modeling framework is that tissue and blood-cell speeds are significantly slower than the acquisition frame rate. As such, we consider all scatterers to be effectively frozen in position while each echo frame is acquired. Additionally, we assume that the SSF remains spatially invariant within the imaging volume Ω, adhering to the principle of local shift-invariance. In our US imaging framework, let $g_{k\ell m}$ describe a sampled time series of 2-D RF echo frames, where k denotes the axial sample, l represents the lateral sample, and m signifies the frame index. The acquisition process can be expressed as:

$$g_{k\ell m} = \epsilon_{k\ell m} + \int_{\mathbf{x}\in\Omega} d\mathbf{x} h_S\left(x - x_\ell, y, z - ct_k/2\right) f\left(\mathbf{x}, t_m\right) \tag{2.3}$$

Here, $\epsilon_{k\ell m}$ represents the bandpass white Gaussian acquisition noise. Equation 2.3 encompasses a three-dimensional integral that effectively implements a two-dimensional convolution within the $x-z$ scan plane. The fast-time variable $t_k = (k-1)T_k$, with $1 \le k \le K$, identifies echo samples acquired along the beam axis at position $z_k = c\tau_k/2$ for a given sound speed c $[mm/\mu s]$. The fast-time sampling rate is defined as $1/T_k = 38.5MHz$. Lateral samples are characterized by $x_l = (l-1)X$, where $1 \le l \le L$, and $X = 0.1mm$

represents the lateral sampling interval determined by the pitch of the linear array transducer. The frame-time variable, denoted as $t_m = (m-1)T_m$ with $1 \leq m \leq M$, sampled at Doppler frame rate $1/T_m = 10Hz$. This Doppler frame rate is not fixed but rather adapts dynamically based on the velocity of blood cells, ensuring optimal data acquisition in varying flow conditions. By combining the mathematical expressions provided in Equations 2.1 and 2.3, we arrive at the formulation:

$$g_{k\ell m} = \epsilon_{k\ell m} + \sum_{n=1}^{N} a_n h_S\left(x_n\left(t_m\right) - x_\ell, y_n\left(t_m\right), z_n\left(t_m\right) - ct_k/2\right) \tag{2.4}$$

In Equation 2.4, a_n represents the reflectivity, and $a_n = \{\tau, \beta\}$ characterizes tissue and blood reflectors. This equation captures the echo signals recorded during the mth frame as the weighted coherent summation of shift-invariant SSF values, sampled at each scatterer's position within the imaging volume Ω By employing a functional representation for h_S, this equation allows us to simulate echo signals for scenarios involving continuously varying scatterer positions. To further refine our modeling, we apply a Gabor approximation to the SSF tailored for a linear array transducer. This approximation is represented as:

$$h_G\left(\mathbf{x}; u_0, \sigma_x, \sigma_z, \varphi\right) = \frac{1}{(2\pi)^{3/2}\left(2\sigma_x^2\right)\sigma_z} \exp\left[-\frac{1}{2}\left(\left(\frac{x}{\sigma_x}\right)^2 + \left(\frac{y}{2\sigma_x}\right)^2 + \left(\frac{z}{\sigma_z^2}\right)^2\right)\right] \times \sin\left(2\pi\left(2u_0/c\right)z + \varphi\right) \tag{2.5}$$

In this equation, u_0, σ_x, σ_z, and φ are free parameters chosen to simulate specific experimental conditions. u_0 denotes the carrier frequency of the US pulse, while σ_x and σ_z define the pulse width and length, respectively. The parameter φ characterizes phase, offering control over the behavior of the SSF. Importantly, we maintain a fixed ratio between the elevational beam width along the y-axis to be twice the lateral beam width along the x-axis. These refinements and approximations enhance the fidelity of our US imaging model, enabling accurate simulations and practical applications in various scenarios.

2.2.3 Blood and Tissue Scatterer Motion Model

The model inherently considers the dynamic motion of scatterers in space during the time intervals between echo frames, with each frame assumed to be instantaneously recorded. The continuous variation in the positions of scatterers between frames is dictated by the velocities of individual tissue and blood scatterers, as described by the following equations:

$$\begin{aligned} \mathbf{x}_p\left(t_m\right) &= (m-1)T_m\mathbf{v}_p\left(t_m\right) + \mathbf{x}_{p0} \\ \mathbf{x}_q\left(t_m\right) &= (m-1)T_m\left(\mathbf{v}_p\left(t_m\right) + \mathbf{v}_q\left(t_m\right)\right) + \mathbf{x}_{q0} \end{aligned} \tag{2.6}$$

Here, $\mathbf{v}_p = \left(v_x, v_y, v_z\right)_p^\top$ and $\mathbf{v}_q = \left(v_x, v_y, v_z\right)_q^\top$ represent the velocities of individual tissue and blood cells, respectively, measured in units of [mm/s]. The initial positions of scatterers are given by x_{p0} and x_{q0}. It's crucial to note that the collective motion of blood cells is determined by the summation of their individual velocities. All scatterer velocities are relative to the axis of the US sound beam. Our simulation encompasses various types of tissue motion. In one scenario, we rigidly translated the tissue between frames, denoted as $\mathbf{v}_p\left(t_m\right) = \mathbf{v}_{p'}\left(t_m\right)$ for all p, p' in Ω. This rigid movement remained constant for each frame, emulating the consistent velocity of the transducer during scanning. Additionally, we introduced oscillations in scatterer positions to replicate physiological phenomena such as breathing and cardiac pulsations. Nonrigid, scaled-coordinate deformations were also explored, where $\mathbf{v}_p\left(t_m\right) = \mathbf{v}\left(x_p/\alpha, \sqrt{\alpha}y_p, \sqrt{\alpha}z_p, t_m\right)$ introduced a

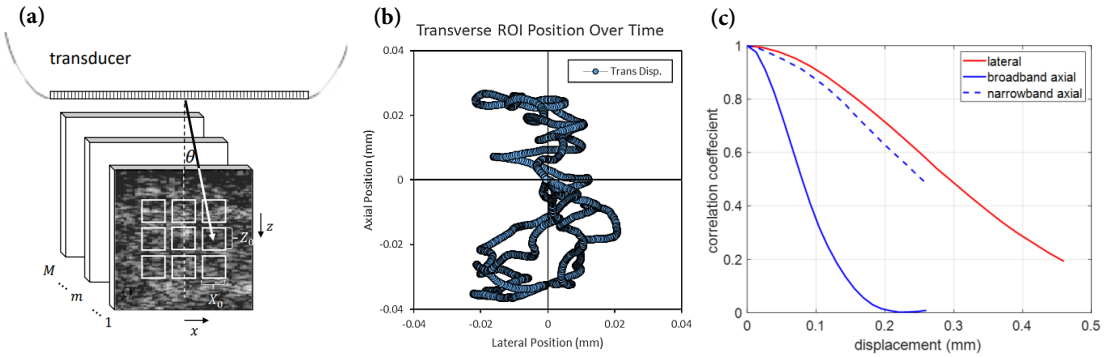

Figure 2.1: (a) Schematic representation of echo data acquisition in the (x, z) scanning plane involving an ensemble of M echo frames. Displacements are computed relative to the initial frame within nine distinct regions. (b) Assessment of clutter motion within a cross-sectional scan plane of the calf muscle. (c) Graphs illustrating correlation coefficient variations concerning the transducer's axial and lateral translation distances.

constant-volume scaling factor α to mimic muscle contractions.

For blood-cell motion, three distinct scenarios were considered. Firstly, we assumed a constant velocity that was uniform for all blood cells. Secondly, we simulated blood cells moving with a defined mean velocity and angular variability. Lastly, we introduced spatially diffuse motion, where individual blood cells moved with constant speed but randomly changed direction uniformly between 0 and 4π. Consequently, the spatially averaged blood velocity was$\overline{\mathbf{v}}_q\left(t_m\right) = 0$. The results from the latter two blood-cell motion scenarios are reported in this thesis. Each motion state exhibits predictable but not necessarily unique effects on the Doppler spectrum. To maintain consistency with empirical data, the ratio of tissue to blood cell reflectivity was set to $\tau/\beta = 10$. This amplitude ratio is derived from extensive literature sampling [31], [32] containing backscatter coefficient measurements from whole blood and skeletal muscle in the frequency range of 5-10 MHz. The higher tissue reflectivity within this ratio implies that the spatial registration of the echo frames is primarily influenced by the coherent motion of clutter.

2.2.4 Displacement Estimation and Spatial Registration

This section looks closely at the techniques employed for displacement estimation and spatial registration in US imaging, which are essential components in separating blood from the clutter domain.

Region Selection and Motion Analysis

The process begins with the selection of regions within each Radio-Frequency (RF) echo frame, denoted as $X_0 \times Z_0$ regions, typically representing 1 mm squares. These regions are chosen based on their homogeneous echogenicity, as visually illustrated in Figure 2.1(a). In scenarios where the transducer remains rigidly fixed in space, the range of motion observed in healthy subjects is typically less than 0.04 mm, as depicted in Figure 2.1(b). Accurate spatial registration and displacement estimation are paramount in such cases, as even slight motion can introduce distortions in the acquired data.

Coarse estimation

To estimate echo translation for each selected region, a two-stage process is employed, initially involving the computation of the discrete two-dimensional spatial cross-correlation function for a set of M echo frames

within the recorded ensemble. Here, spatial coordinates are represented as k' and ℓ', and the displacement in the horizontal and vertical dimensions is denoted as Δk and $\Delta \ell$, respectively. For a stationary random process g within an analysis region of dimensions $X_0 \times Z_0$, the cross-correlation function is expressed as:

$$\phi_{\Delta k \Delta \ell m m'} = \mathcal{F}^{-1}\left\{\mathcal{F}\left\{g_{k,\ell,m}\right\}\left(\mathcal{F}\left\{g_{k',\ell',m'}\right\}\right)^*\right\} \tag{2.7}$$

Where $\mathcal{F}\{\cdot\}$ denotes the discrete forward Fourier transform, $\mathcal{F}^{-1}\{\cdot\}$ is the inverse transform, and the asterisk represents complex conjugation. The displacement of echoes between frames m and m' is estimated as an integer number of samples, obtained by identifying the peak of the cross-correlation function:

$$[\Delta\hat{k}, \Delta\hat{\ell}]_{mm'} = \arg\max_{\Delta k, \Delta \ell} \phi_{\Delta k \Delta \ell m m'} \tag{2.8}$$

In the absence of motion (e.g., $v_p = 0$ or $m = m'$), the expectation is that $\Delta\hat{k} = \Delta\hat{\ell} = 0$. It's important to note that, due to the echo samples being $X = 0.1$ mm laterally and the $cT_k/2 = 0.02$ mm axially, this initial step provides coarse estimates, with the resolution limited by the size of the echo-signal sample size.

Sub-sample Translation Estimation

The second stage of the process involves sub-sample translation estimation. Here, a combination of cubic spline interpolation and a 2D unconstrained nonlinear optimization search procedure is implemented, utilizing the Matlab function `fminsearch`. In each iteration of the search process, the M-th echo frame is interpolated using Matlab's `interp2` function. Subsequently, a derivative-free simplex search technique [33] is employed, involving a cross-correlation analysis between the interpolated M-th frame and -1 times the M'-th echo frame. The choice to manipulate the sign of one of the two frames is made to facilitate the identification of the correlation minimum. The fine-scale search begins with the preliminary coarse-scale estimates and concludes upon reaching a convergence threshold of 10^{-4}. This results in a sub-sample displacement vector estimate represented as $d' = (\Delta x', \Delta z')$.

Net Displacement Estimate

The overall displacement estimate characterizing the translation of frame M' relative to frame M in millimeters is expressed as:

$$\mathbf{d}_{mm'} = \begin{pmatrix} \Delta x \\ \Delta z \end{pmatrix}_{mm'} = \begin{pmatrix} \Delta\hat{\ell} X + \Delta x' \\ \Delta\hat{k}\frac{cT_k}{2} + \Delta z' \end{pmatrix}_{mm'} \tag{2.9}$$

This two-step approach has been demonstrated to yield unbiased sub-sample displacement estimates and is effective at mitigating the risk of becoming trapped in local minima, a common occurrence when dealing with multi-cycle (narrowband) Doppler pulses. Simulated echo signals are subject to rigid frame translations during the registration process, allowing for the averaging of estimates obtained from multiple subregions within a frame, as depicted in Figure 2.1. These estimates are conducive to minimizing the impact of random errors stemming from noise, with the SNR for simulations set at 30 dB. In the context of measuring displacements relative to the first frame, the frames within the ensemble are spatially aligned with the initial frame through spline interpolation, with a grid shift parameterized by $d_{1m'}$. If tissue motion exhibits nonrigidity across the entirety of the echo frame, adjustments to the window size and position can be made to detect deformation and spatially register each subregion individually.

This comprehensive approach to displacement estimation and spatial registration is pivotal in enhancing the quality and reliability of echo data in US imaging. It ensures that even in the presence of motion and noise, accurate and coherent images can be acquired and analyzed.

2.2.5 Phantom Experiments Validation

The simulation presented in the previous sections underwent experimental verification, performed using a gelatin phantom with uniformly distributed scatterers. To emulate real-world scenarios, a simple phantom was crafted following established methodologies [34]. While this phantom did not incorporate perfusing scatterers due to the complexities associated with introducing a realistic flow pattern, it was instrumental in focusing on the critical task of spatially registering echo frames in the presence of moving clutter and noise sources. The experimental setup involved scanning a stationary and congealed gelatin block using a linear array transducer. The key aspect of this setup was the controlled motion of the gelatin block in three dimensions, allowing for the assessment of registration errors under known conditions. These errors were quantified as a function of the inter-frame correlation because correlation lengths characterize beam properties [35]. Correlation lengths provide a robust measure of performance and accuracy, as they are independent of the beam shape.

2.2.6 PCA Filtering

In this section, we discuss the application of PCA as a filtering technique for processing RF echo data in the context of PD-US imaging.

Data Preparation

To begin the PCA filtering process, we start with the RF echo data collected from a specific 2-D subregion, as illustrated in Figure 1. The RF echo data in the first frame of an ensemble is organized into a 1 $\times$ N row array. This process is then repeated for the same subregion across all M frames, resulting in an M $\times$ N echo matrix, denoted as X. Here, M represents the temporal samples, and N represents the spatial samples.

Temporal Covariance Approximation

The temporal covariance matrix of the zero-mean echo signals denoted as K_X, is approximated as:

$$K_X = \frac{1}{M-1} X X^T, \tag{2.10}$$

where the approximation assumes that the echo signals are derived from an ergodic random process. This approximation allows us to perform spatial averaging as a substitute for ensemble averaging.

Eigen-decomposition

Next, we apply an eigen-decomposition to the temporal covariance matrix K_X [36]:

$$K_X = V \Lambda V^T, \tag{2.11}$$

In this equation, the columns of the M $\times$ M unitary matrix V represent the eigenvectors of the temporal covariance matrix, while the nonzero elements of the M $\times$ M diagonal matrix Λ represent the corresponding

eigenvalues. These eigenvalues are real and sorted in descending order, with $\lambda_1 > \lambda_2 > \ldots > \lambda_M$.

The principal components of K_X are extracted through the product:

$$Y = V^T X. \tag{2.12}$$

PCA filtering is employed to eliminate all principal components that are not associated with the blood subspace, resulting in the filtered echo signal matrix Y'. Subsequently, the filtered echo data matrix X' is reconstructed as:

$$X' = VY'. \tag{2.13}$$

Each column of X' is then reassembled into a 2-D echo subregion. This step is crucial in isolating the signal components attributed to the motion of blood cells. If the source subspaces are indeed separable and the filter thresholds are judiciously selected, the remaining signal power in X' predominantly comprises the echo signals originating from moving blood cells. The utilization of PCA filtering in US imaging is a powerful technique for enhancing the visualization of dynamic structures within the body, particularly in scenarios involving the observation of blood flow and tissue motion.

2.3 Results

2.3.1 Estimation of Clutter Motion

This subsection presents the results of displacement estimation based on Equation 2.9 and discusses the associated errors, represented as the difference between estimated displacement and true displacement, for both radio-frequency (RF) and envelope (ENV) signals. The signals discussed here primarily consist of noisy clutter echoes, without blood perfusion, aimed at emulating the phantom measurements presented later in this section.

The in-plane motion results, depicted in Figure 2.2, simulate the estimates of clutter movement as the transducer is moved within the x-z scan plane while scanning a fixed random scattering medium, as illustrated in Figure 2.1 a. On the other hand, the out-of-plane motion results in Figure 2.3 are obtained by moving the transducer in elevation along the y-axis. All the results are generated using a 5 MHz pulse frequency and are categorized into two scenarios: 75% fractional pulse bandwidth (broadband, BB) and 25% fractional pulse bandwidth (narrowband, NB). The pulse is calculated at a focal length of f/2 in-plane aperture and an f/4 elevational aperture, remaining shift invariant across the simulated echo field. Comparisons between RF and ENV results are made to examine the effects of pulse modulation on estimation errors, with the echo SNR held constant at 30 dB.

A crucial factor in minimizing displacement errors when registering echo frames is to maintain a high correlation between the pairs of echo frames under comparison. The impact of pulse SSF size and shape on echo correlation is assessed through axial and lateral correlation coefficients, as depicted in Figure 2.1 c for in-plane motion and Figure 2.3 f for out-of-plane motion. Each correlation coefficient curve is derived from a series of echo frames acquired as the transducer is moved along the axial, lateral, or elevational axes. In-plane motion exhibits minimal echo decorrelation, while significant decorrelation is observed for out-of-plane motion exceeding the elevational beam width. These correlation curves are derived from the ENV of the RF echo signals.

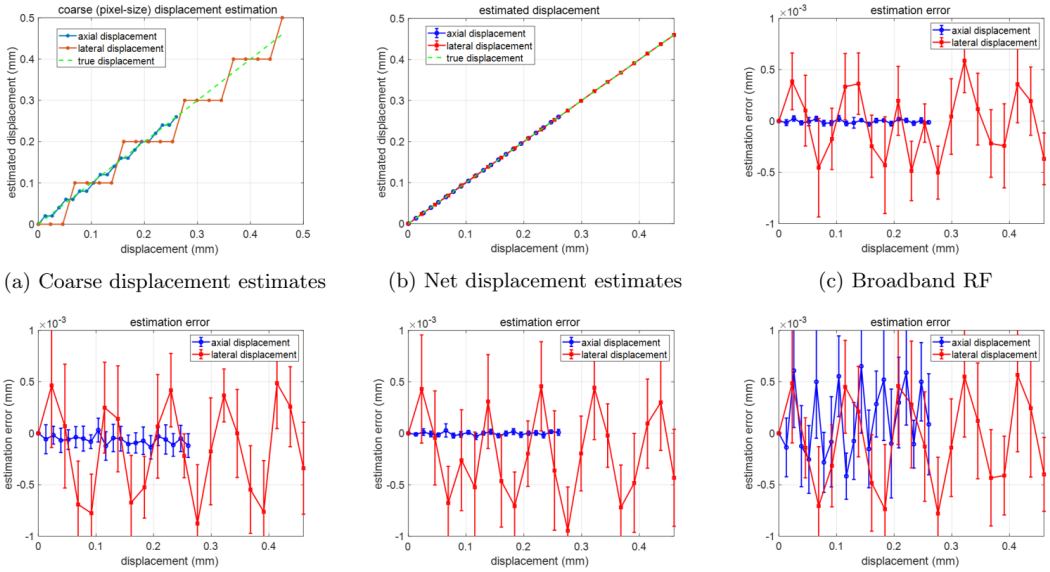

(a) Coarse displacement estimates (b) Net displacement estimates (c) Broadband RF

(d) Broadband ENV (e) Narrowband RF (f) Narrowband ENV

Figure 2.2: In-plane displacement estimates and errors for 5 MHz echo signal simulations.

These results offer valuable insights into the impact of different motion scenarios and pulse characteristics on the quality of displacement estimation in US imaging.

2.3.2 In-Plane Measurements of In-Plane Motion from Simulated Echo Data

Here we presents the results of in-plane motion estimation based on simulated echo data, with a focus on the evaluation of displacement estimates. The results of Figure 2.2 a, b are derived from the broadband ENV signals as the transducer undergoes diagonal motion within the scan plane. The total displacement encompasses 0.46 mm along the x-axis and 0.26 mm along the z-axis. Dashed lines in the provided figures represent the true values. Notably, these displacement ranges are notably larger, approximately 5-10 times greater, than the range of clutter translation typically observed in clinical scenarios, as exemplified in Figure 2.1 b. The error plots illustrated in Figures 2.2 c-f display the mean errors along with the range of standard deviation (± 1 SD) computed from 9 non-overlapping subregions within an echo frame. A comprehensive analysis of these results reveals several significant findings. For axial measurements, the smallest displacement errors are observed, particularly when using narrowband radio-frequency (RF) signals. However, it is worth noting that the errors associated with broadband RF signals are also within a similar range. Importantly, pulse modulation techniques play a pivotal role in substantially reducing displacement errors in this range of motion. Conversely, the largest displacement errors are encountered when making lateral estimates, with error magnitudes roughly equivalent across various situations, even when employing a constant cross-range beam width. To further comprehend the impact of pulse length and modulation, a direct comparison can be made by examining the axial measurements represented by the blue curves in Figure 2.2 c-f.

2.3.3 In-Plane Measurements of Out-of-Plane Motion from Simulated Echo Data

Now we explore the results of in-plane displacement estimates obtained from simulated echo data, focusing on the impact of out-of-plane motion. The transducer's motion perpendicular to the scan plane, along the y-axis, is the primary focus. In these scenarios, the true displacements are consistently zero in each plot, as the motion is solely out-of-plane. The following observations are derived from the analysis:

Figure 2.3 a-e visually represents in-plane displacement estimates as the transducer is translated along the y-axis. These translations induce out-of-plane motion, making it essential to monitor the corresponding errors. Particularly, the 5 MHz broadband radio-frequency (RF) signals in Figure 2.3 a demonstrate that the transducer can be translated in an elevational direction by up to 1.2 mm before encountering a notable increase in estimation errors. The first 1.2 mm of data in Figure 2.3 a is presented more comprehensively in Figure 2.3 b, where a progressive rise in measurement errors is evident. These errors are primarily attributed to a reduction in elevational correlation coefficients, which fall to approximately 0.1 (as illustrated in Figure 2.3 f). Moreover, the results indicate that there is no significant distinction between lateral and axial displacement errors in the presence of elevational decorrelation.

In summary, the analysis reveals that both measurement bias and variance for in-plane displacement estimates exhibit a gradual increase as elevational correlation diminishes. For radio-frequency (RF) echo signals, the tolerable range of elevational decorrelation extends up to 0.2, while for ENV signals, this range reaches up to 0.4. Beyond these thresholds, displacement estimates become unreliable and, subsequently, fail to provide accurate results. These findings establish critical limits that help define the permissible ranges of out-of-plane clutter motion for robust perfusion imaging applications.

These findings shed light on the nuances of in and out of plane motion estimation and the factors influencing displacement errors. It is evident that the choice of signal type, such as narrowband RF or broadband ENV, and the implementation of pulse modulation techniques significantly impact the accuracy of displacement estimates in response to various motion scenarios.

2.3.4 Experimental Verification of Simulation Results via Phantom Measurements

This section presents an experimental verification of a subset of results obtained from Figures 2.2 and 2.3 by conducting real-world measurements on a random-scattering gelatin phantom. The experiments involved using an Ultrasonix SonixRP system operating at 5 MHz, mirroring the system parameters employed in the simulated echo data. The SNR for the experimental setup was measured at 32 dB, aligning it closely with the simulated conditions.

Figure 2.4 displays the experimental results for broadband ENV data, where the transducer was systematically moved along one of three axes in each experiment, with efforts made to minimize motion along the other two axes. The following observations were made:

The experimental results closely resemble the simulations for both the ENV signal and the radio-frequency (RF) signals (not shown). While the agreement is substantial, it's worth noting that there may have been minimal unintended movement along the axes that should ideally remain stationary, as evidenced by the small axial displacement in Figure 2.4 a and lateral displacement in Figure 2.4 b. Furthermore, the comparison of the correlation functions between Figure 2.4 d and Figure 2.4 f suggests that the actual beam width in elevation may be broader than what is indicated by the nominal probe specifications. However, this broader

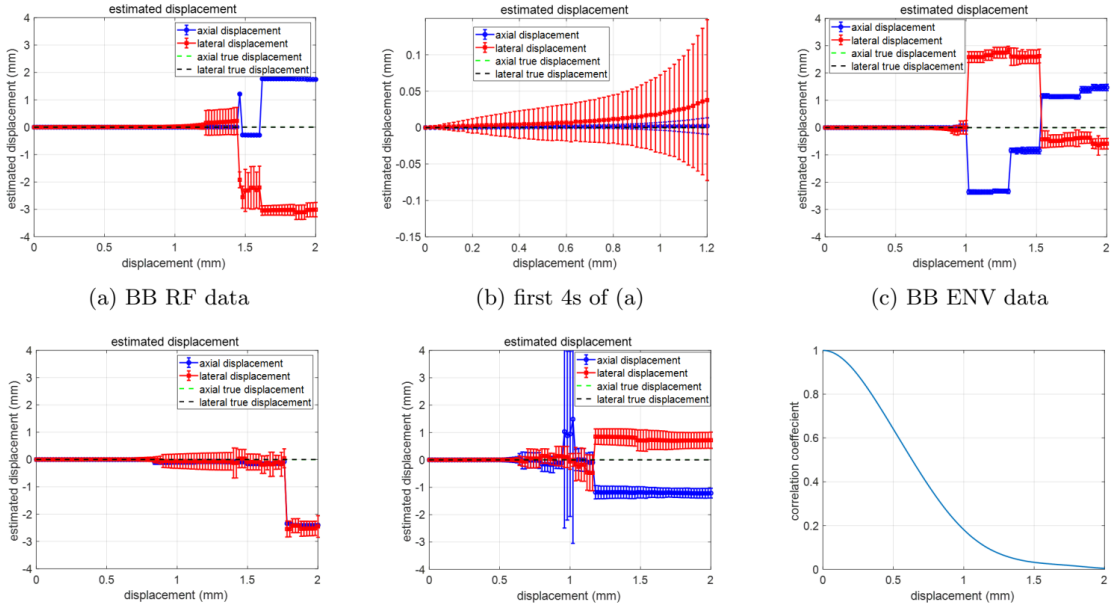

(a) BB RF data (b) first 4s of (a) (c) BB ENV data

Figure 2.3: Estimation of in-plane motion when the probe is moved in elevation for 5 MHz simulated broadband (BB) and narrowband (NB) RF and ENV echo data.

sound beam's impact on displacement estimates was found to be insignificant when assessing the experimental results against simulations.

The results in this section, both from simulation and experiment, focus on registration errors for clutter signals within a noisy environment, without the presence of blood perfusion. It is evident that by processing 5 MHz broadband RF echo signals, reliable measurements of in-plane-only translations greater than 0.005 mm can be achieved, with negligible bias and SDs less than 0.02 mm, achieved through spatial averaging over 1 mm^2 regions. The in-plane errors arising from out-of-plane motion are largely determined by the beam width in elevation and are predictable from the elevational correlation coefficient. The following section expands upon these findings, introducing a blood echo signal to the simulations of clutter and noise components to draw conclusions about the effectiveness of clutter filtering in perfusion imaging.

This experimental verification bridges the gap between simulation and real-world scenarios, providing valuable insights into the potential of clutter filtering in US perfusion imaging.

2.3.5 Separation of Clutter and Blood Components

Two distinct spatial distributions of blood cell movements were examined in these simulations. In both scenarios, blood is confined to a central perfusion region, as observed in the colored area in the PD-US images shown in Figure 2.6. Within the perfusion region, the echo signals include contributions from blood, clutter, and noise components, whereas outside this region, the volume contains clutter and noise only. Notably, all blood cells move at a speed of $|v_q| = 0.2$ mm/s.

In the first distribution, the average direction of blood cell motion aligns with the +z axis, while individual blood cells' directions are randomly varied over a 30° opening angle, creating a cone-like distribution centered about the z-axis. In the second distribution, each blood cell moves in a random direction over a full $4pi$ spherical area, simulating the random diffusion-like motion of the blood cells. The clutter motion, with

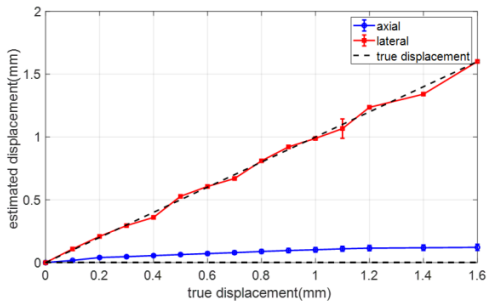

(a) BB ENV data with lateral motion

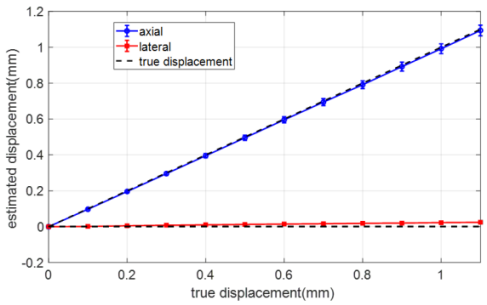

(b) BB ENV data with axial motion

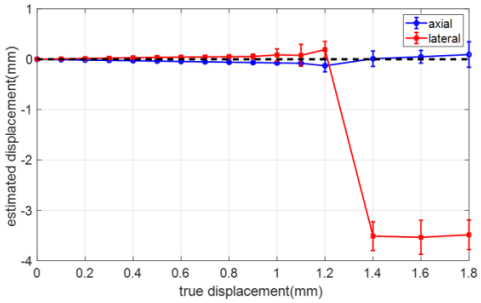

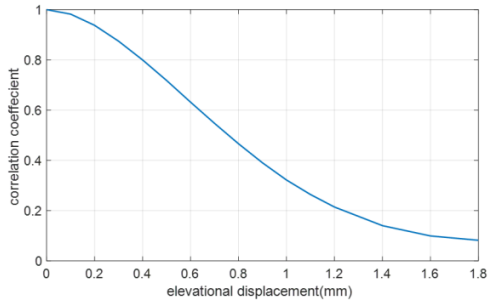

Figure 2.4: Displacement estimations for 5 MHz phantom experiments.

velocity in [mm/s], remains constant at $\mathbf{v}_p = 0.17\hat{x} + 0.23\hat{z}$, indicating movement down and to the right, as illustrated in Figure 2.6 c and 2.6 f. The ratio of tissue to blood amplitude reflectivity, $\tau/\beta = 10$, maintains consistency with empirical data. To spatially register the echo frames, a two-step process is employed. Initially, displacements are measured in each of the subregions within a 3x3 array, and the results are averaged. It's important to note that the central three subregions include contributions from blood, clutter, and noise sources, while the remaining six subregions contain only clutter and noise. The average displacement obtained is then applied to register the entire frame. Given the inherent variability of perfusion within tissues, mixing subregions with and without perfusion to estimate clutter movement is a practical necessity in this context.

2.3.6 Doppler Spectrum Analysis

Following the clutter filtering process, the evaluation of remaining signal power is accomplished through the computation of the Doppler power spectral density. Power spectra are computed at each sample within a 2×2 mm^2 region and subsequently averaged. In the ensemble consisting of M = 21 frames, 21 spectral points are obtained, allowing for the examination of the Doppler spectrum. As these data are simulated, it becomes feasible to separately compute the clutter and blood spectra and also explore their combined effects. It's essential to note that the integral of the Doppler spectrum, although not quantitatively linked to blood perfusion, exhibits a monotonic relationship with changes in perfusion when measured in [ml/min per gram of tissue], given that the clutter and noise components are effectively minimized.

In the case of spatial registration without PCA clutter filtering, the impact on the Doppler spectrum is evident, as demonstrated in Figure 2.5. The top row of figures displays the registration errors and Doppler spectra for axially directed perfusion, while the second row pertains to diffusive perfusion scenarios. Similar to the findings in the noisy clutter simulations presented in Figure 2.2, the displacement estimates maintain

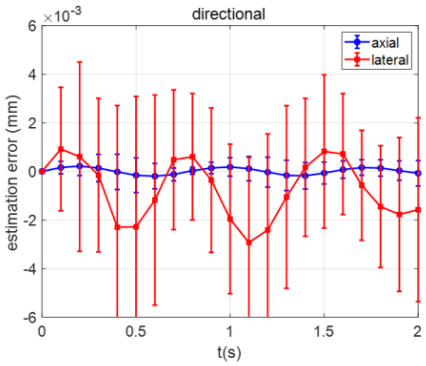

(a) Registration errors for directional perfusion

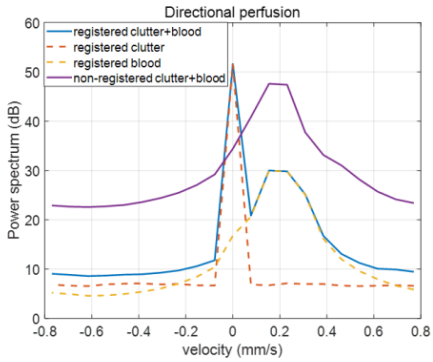

(b) Power spectra for directional perfusion

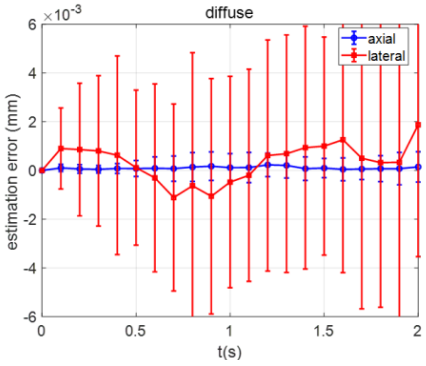

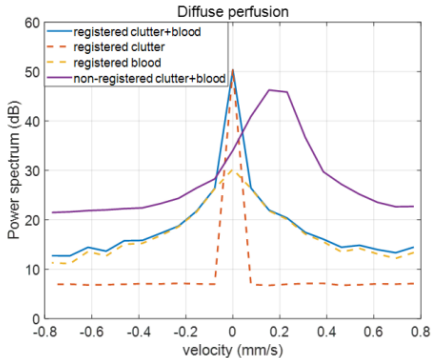

Figure 2.5: Registration errors and power spectra with and without spatial registration

their unbiased nature. However, the introduction of blood scatterers results in an increase in the SD of displacement estimates by approximately a factor of six. The most noteworthy observations stem from the analysis of the Doppler spectra. With simulated blood perfusion in the presence of in-plane clutter motion, as depicted in Figures 2.5 b, d, the Doppler spectra exhibit similarity before the registration process. Each spectrum reveals a peak close to the axial component of clutter velocity. These spectral peaks undergo broadening due to the lateral component of clutter motion and the variable movement direction of blood cells.

After the spatial registration process, the Doppler spectrum in Figure 2.5 b, associated with axially directed perfusion, exhibits several distinct features. Firstly, a robust peak at zero velocity signifies the signal power originating from spatially registered clutter echoes. Concurrently, there exists a weaker yet broader peak, located near the mean velocity of the perfusing blood, specifically at 0.2 mm/s. By separately processing the noisy clutter and noisy blood signal components, it becomes evident how these individual components (depicted as dotted-line spectra) combine to create a spatially registered net spectrum, illustrated in blue.

In the case of diffusive perfusion, as shown in Figure 2.5 d, the Doppler spectrum transforms into a symmetric peak centered at the origin post-registration. The analysis of component spectra highlights that the stationary clutter power is predominantly concentrated at zero velocity. On the other hand, the blood power exhibits a more extensive distribution about zero velocity, which aligns with the expectation for directionally variable blood cell movements featuring zero mean axial velocity. This transformation raises the question of how to accurately compute the blood power while minimizing the influence of clutter within the Doppler spectrum.

2.3.7 DC-Blocker Clutter Filter

One of the simplest approaches to clutter filtering is the use of a DC-blocker filter. It assumes that spatial registration is highly effective in concentrating all the clutter power at the origin of the Doppler spectrum. Consequently, the filter estimates the blood power by integrating the Doppler spectrum while excluding the value at the origin. Alternatively, in the temporal domain, the DC-blocker filter can be implemented by subtracting the temporal average signal at each spatial position, squaring the results, and averaging over both time and space. The efficacy of this filter in isolating the blood power is contingent on the perfusion model. When the DC-blocker filter is applied to the results in Figure 2.5 b, associated with axially directed perfusion, the measured power is 316.94 units. In comparison, the power within the blood-only component is 315.03. For this particular perfusion model, the DC-blocker filter works fairly well. However, in the case of the results shown in Figure 2.5 d, corresponding to diffusive perfusion, the filtered power measures 173.08, while the power in the blood-only component is 309.87. In this scenario, the DC-blocker filter eliminates a significant portion of the blood power because a substantial fraction of the diffusive blood signal energy is concentrated at the origin.

It's essential to acknowledge that some loss of blood-signal power is expected when employing any clutter filter. The quality of a clutter filter is often assessed by its ability to maximize the blood-to-clutter power ratio. In the subsequent section, we investigate the performance of PCA clutter filters, both with and without spatial registration.

2.3.8 PCA Clutter Filter: Axially Directed Perfusion

The PCA clutter filter, as described in Section 2.2.6, operates by expanding the echo signal into spatial and temporal eigenbases. Unlike a Fourier basis, these eigenbases allow for the separation of signal components based on the spatial coherence of motion and velocity differences. In this section, we evaluate the effectiveness of combinations of registration and PCA filtering for clutter-blood separation, specifically for directed and diffusive perfusion cases. We compare these results with those obtained using the DC-blocker filter. To apply the PCA filter, it is necessary to define two thresholds: one to separate the clutter and blood subspaces in the eigenspectrum, and another to distinguish the blood and noise subspaces (see Figure 2.6 b for reference). The criteria for selecting these thresholds are to maximize both the blood power and the ratio of blood-to-clutter power. The PCA clutter filter's performance is assessed based on these criteria, and the results are presented for the case of axially directed perfusion.

Perfusion with Nonzero Axial Velocity (Axial Directed Perfusion):

In this section, we explore the scenario of perfusion with a nonzero axial velocity, specifically axial-directed perfusion. We investigate the effectiveness of PCA filtering without spatial registration for this case, utilizing certain criteria to identify the blood subspace within the eigen spectrum. Table 2.1 presents power measurements corresponding to various threshold values, with the bolded column indicating values that meet the established criteria. The PCA-filtered Doppler spectra for unregistered echoes are illustrated in Figure 2.6 a.

Additionally, for the case of directed perfusion, we extend our analysis by employing PCA filtering with spatial registration. This approach yields a different set of criteria for the blood subspace, spanning thresholds in the range of 2-5 (Figure 2.6 e). The corresponding PCA-filtered Doppler spectra for the registered echoes are displayed in Figure 2.6 d, while Table 2.2 provides power estimates for various threshold values.

Eigenvalues	5-6	**5-7**	5-8	5-9	5-10	6-8	4-8
Blood power	177.98	**213.06**	220.96	226.43	228.58	117.63	307.32
Clutter power	4.86	**8.55**	10.13	11.10	11.73	8.25	81.87
Blood clutter power ratio	36.62	**24.92**	21.81	20.4	19.49	14.26	3.75

Table 2.1: PCA filtered blood and clutter power estimates (without registration) at various filter thresholds for directed perfusion. The true signal power from simulated blood perfusion is 215.19. Bolded values were thresholds selected for spectra shown in Figure 2.6 a.

Eigenvalues	2-3	2-4	**2-5**	2-6	2-7	2-8	3-5
Blood Power	198.63	224.17	**232.18**	232.63	234.23	236.01	91.31
Clutter Power	1.52	2.15	**2.74**	3.36	3.93	4.67	1.77
Blood-Clutter Power Ratio	130.67	104.26	**84.74**	69.23	59.60	50.54	51.58

Table 2.2: PCA filtered blood and clutter power estimates (with registration) at various filter thresholds for directed perfusion. The true signal power from simulated blood perfusion is 237.69. Bolded values were thresholds selected for spectra shown in Figure 2.6 d.

The PCA-filtered Doppler spectra for registered echoes are presented in Figure 6d, and the corresponding power estimates for various threshold values are detailed in Table 2.

A comparative analysis of Figures 2.6 a and 2.6 d reveals several key observations. Firstly, the application of spatial registration prior to PCA filtering (Figure 2.6 a) leads to several improvements: (a) a narrowing of the clutter contribution to the Doppler spectrum, with values concentrated near zero velocity, (b) enhanced clarity of the blood perfusion peak at 0.2 mm/s, and (c) an increase in clutter rejection across the spectrum.

Furthermore, for scenarios involving directed perfusion, the estimated blood power values closely approximate the true blood-signal power values, as listed in Tables 2.1 and 2.2. Notably, there is little qualitative difference between the PD-US images displayed in Figures 2.6 c and 2.6 f. Spatial registration provides the advantage of superior clutter suppression, as evidenced by the larger Blood-To-Clutter Ratio (BTCR).

2.3.9 PCA Clutter Filter in Diffusive Perfusion Case

The same analysis is applied when the spatially averaged perfusion velocity is zero, representing diffusive perfusion. However, the effects on blood-power estimation differ significantly from the directed flow results in Figure 2.6.

For diffusive perfusion using PCA filtering without spatial registration, the blood subspace corresponds to the eigen-index range 6-9. Table 2.3 presents power measurements for various threshold values. The corresponding PCA-filtered Doppler spectra for unregistered echoes are displayed in Figure 2.7 a. Applying PCA filtering with spatial registration for diffusive perfusion results in the criteria defining the blood subspace as 2-10 (Figure 2.7 e), with power estimates for different threshold values provided in Table **??**.

Eigenvalues	6-14	6-13	6-12	6-11	6-10	**6-9**	6-8	5-8	4-8	7-8
Blood Power	45.01	42.6	39.3	35.96	31.95	**28.97**	24.21	46.62	135.86	14.84
Clutter Power	6.84	6.21	5.47	4.77	4.09	**3.33**	2.73	10.51	75.25	1.87
Blood-Clutter Power Ratio	6.58	6.86	7.18	7.54	7.81	**8.7**	8.86	4.43	1.81	7.93

Table 2.3: PCA filtered blood and clutter power estimates (without registration) at various filter thresholds for diffusive perfusion. The true signal power from simulated blood perfusion is 274.57. Bolded values are the thresholds selected for spectra shown in Figure 2.7 a

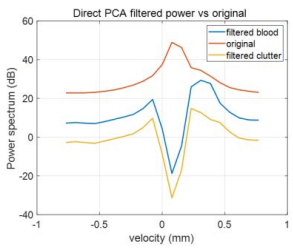

(a) Direct PCA filtered

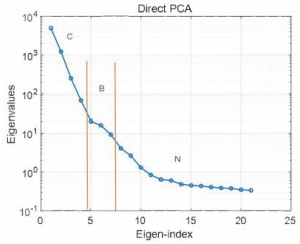

(b) Eigen-spectrum without echo-signal registration

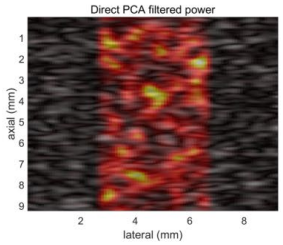

(c) PCA-filtered PD-US image without spatial registration

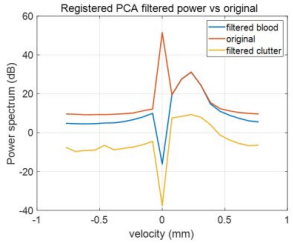

(d) Registered PCA filtered

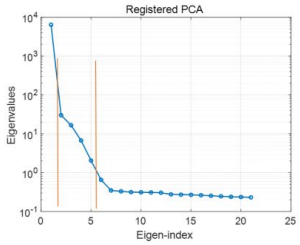

(e) Eigen-spectrum with echo-signal registration

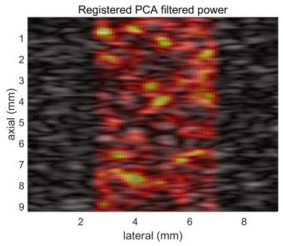

(f) PCA-filtered PD-US image with spatial registration

Figure 2.6: In Figures (a-c) and (d-f), we present the results of PCA clutter filtering for scenarios with axial directed perfusion in the presence of a moving clutter field, while maintaining an echo SNR of 30 dB. The spectra labeled 'original' and 'filtered blood' are derived from data within a central 2×2 mm^2 region where both clutter and blood components are present. These spectra represent the average Doppler spectra within this region. In contrast, the spectra labeled 'filtered clutter' originate from a region of the same size near the margins of the image where there is no blood perfusion. These spectra serve to measure the clutter power that leaks through the PCA clutter filter. Notably, without the application of spatial registration, the spectral extrema in Figure (a) are not located at zero velocity.

Comparing Figures 2.7 a and 2.7 d, it is evident that spatial registration narrows the clutter component in the Doppler spectrum. The eigen-spectra no longer exhibit prominent blood velocity peaks on either side of zero velocity, and diffusive blood velocities manifest broadly and symmetrically at both positive and negative velocities in the Doppler spectrum. Significantly, the PCA filter now removes a substantial portion of the measured blood power, primarily due to its suppression of stationary echoes.

Eigenvalues	2-5	2-6	2-7	2-8	2-9	**2-10**	2-11	2-12	3-10
Blood Power	103.34	110.42	116.18	122.78	127.46	**131.01**	135.08	136.39	92.91
Clutter Power	2.6	3.08	3.79	4.31	4.95	**5.6**	6.15	6.73	5.48
Blood-Clutter Power Ratio	39.75	35.85	30.65	28.49	25.75	**23.40**	21.96	20.27	16.95

Table 2.4: PCA filtered blood and clutter power estimates (with registration) at various filter thresholds for diffusive perfusion. The true signal power from simulated blood perfusion is 274.57. Bolded values are the thresholds selected for spectra are shown in Figure 2.7 d.

However, spatially registering the echoes before PCA filtering yields two key benefits: (a) recovery of 4.5 times more of the true blood-signal power and (b) a threefold increase in the BTCR when compared to measurements made without spatial registration prior to PCA filtering. The increase in perfusion is visually indicated in Figure 2.7 f when compared to Figure 2.7 c.

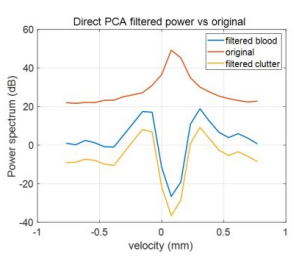

(a) Direct PCA filtered

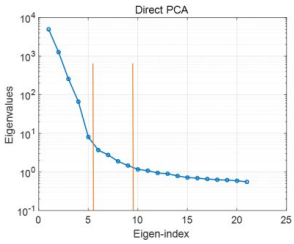

(b) Eigen-spectrum without echo signal registration

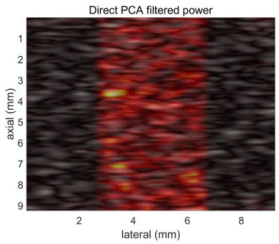

(c) PCA-filtered PD-US image without spatial registration

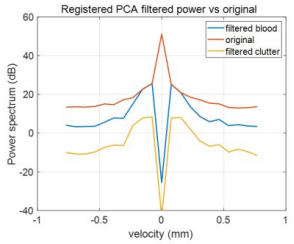

(d) Registered PCA filtered

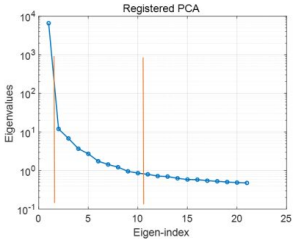

(e) Eigen-spectrum with echo signal registration

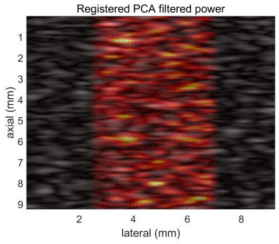

(f) PCA-filtered PD-US image with spatial registration

Figure 2.7: PCA clutter filtered results without (a-c) and with (d-f) spatial registration applied to the echo ensemble before filtering are shown. These data have diffusive perfusion in a moving clutter field, and the echo SNR is 30 dB. The spectra labeled 'original' and 'filtered blood' are an average from data in a central 2 × 2 mm2 region where there are both clutter and blood components. The spectra labeled 'filtered clutter' are from the same-size region near the margins where there is no blood perfusion. The latter spectra measure the clutter power leaking through the PCA clutter filter. Notice that without registration, the spectral extrema in (a) are not located at zero velocity.

PD-US Images: Spatial Registration Followed by PCA Clutter Filtering.

Figure 2.8 illustrates examples of PD-US images for directed and diffusive perfusion. The key advantage of power-Doppler (PD) methods is their ability to retain sensitivity to blood-cell movements regardless of direction, distinguishing them from color-flow methods. In each of the six images, the speed of each blood cell is 0.2 mm/s. In Figure 2.8 a, the mean velocity is directed downward along the beam axis. In Figure 2.8 b, the mean velocity is directed laterally, to the right, and in Figure 2.8 c, the mean velocity is directed elevationally, into the scan plane. The figure captions indicate that the true blood-signal velocity is detected primarily when perfusion is directed along the beam axis, while measured values decrease to approximately 10% for directed perfusion oriented perpendicular to the beam.

Examples of diffusive perfusion (also with blood cells moving at 0.2 mm/s but with zero mean velocity) are presented in Figures 2.8d-f. As expected, the measured blood power remains roughly the same in each flow channel, with values ranging from 30% to 50% of the true blood-signal power. Furthermore, when echo frames are spatially registered before PCA filtering, the BTCRs are notably larger compared to PCA clutter filtering alone.

2.4 Discussion

Here, we explore the advantages of Power-Doppler (PD) imaging in assessing peripheral perfusion. PD imaging offers unique benefits over Color-Flow imaging, primarily due to its ability to detect blood cell

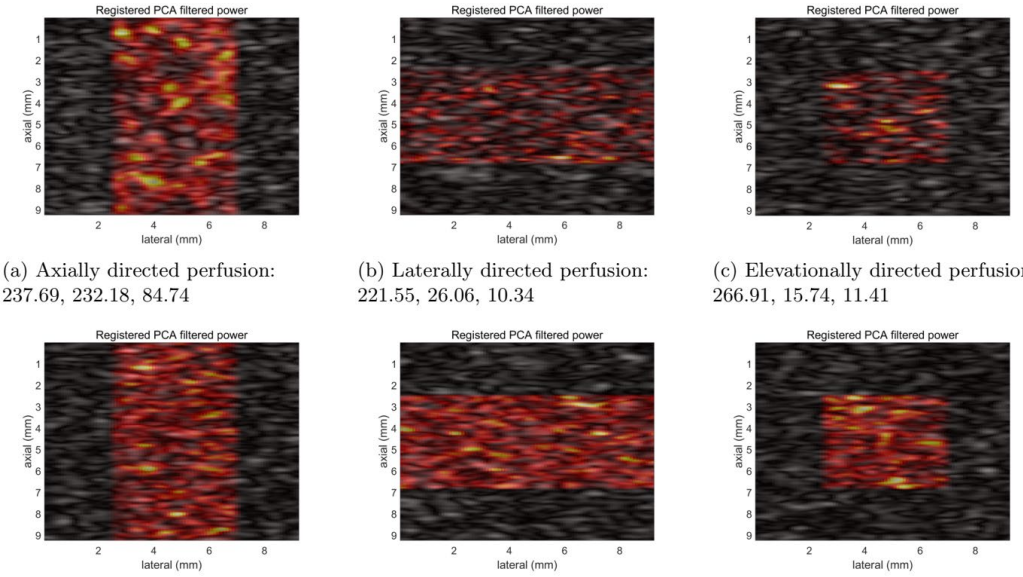

(a) Axially directed perfusion: 237.69, 232.18, 84.74

(b) Laterally directed perfusion: 221.55, 26.06, 10.34

(c) Elevationally directed perfusion: 266.91, 15.74, 11.41

(d) Diffuse perfusion: 274.57, 131.01, 23.4

(e) Diffuse perfusion: 287.72, 98.46, 22.0

(f) Diffuse perfusion: 280.9, 100.69, 21.4

Figure 2.8: PD-US images of directed perfusion where the mean velocity is along the beam axis (a), lateral to the beam axis (b), and into the scan plane (c). In (d)-(f), the perfusion is diffuse. After modeling each situation, the simulated echo signals are first spatially registered and then PCA-filtered before computing blood power as a function of position. The three numbers are, respectively, the true blood power, the measured blood power, and the BTCR after filtering.

movement without directional limitations or aliasing issues. This is achieved by using low Doppler sampling rates (typically around 10 Hz), enhancing sensitivity to slower reflector speeds (below 1 mm/s). However, this increased sensitivity introduces challenges in distinguishing tissue and blood-signal components, resulting in spectral overlap.

Our approach to clutter filtering in peripheral perfusion PD-US involves spatially registering echo frames. We assume that tissue reflectors are the dominant signal contributor and that tissue motion exhibits greater spatial coherence than blood perfusion. By minimizing clutter power and optimizing echo SNR, we reliably infer relative perfusion and regional ischemia. Simulated echo-signal frames represent slow continuous scatterer movements of tissue clutter and blood cells. Through these simulations, we successfully estimate spatially coherent clutter movements as small as 0.005 mm, with minimal bias and low SDs achieved through spatial averaging. Accurate and precise registration methods are crucial for evaluating the benefits of spatial registration in clutter filtering. Nevertheless, the key focus in perfusion imaging is obtaining a consistent measure of blood power. PD-US imaging, while not providing quantitative perfusion measurements, serves as a reliable and consistent indicator with predictable variations.

In our simulations, spatially registering echo frames before applying PCA clutter filtering significantly improved the specificity of PD-US imaging for detecting true blood perfusion, leading to an increased blood-to-clutter signal-power ratio. Simulations considered scenarios where individual blood cell speeds were fixed at 0.2 mm/s, and the average speed was directed with known variability or diffusive with zero average velocity (as depicted in Figure 2.8). The true blood-signal power was determined from simulated echo power, excluding clutter but including noise components. In cases of directed perfusion, all true blood-signal power was recovered when perfusion aligned with the sound beam, while only about 10% was detected

when perfusion was normal to the beam axis. For diffusive perfusion, only one-third to one-half of the true blood-signal power was recoverable, with lost power directing a significant portion of the blood energy to the zero-frequency value in the Doppler spectrum, eliminated by the PCA clutter filter. Spatial registration before PCA filtering consistently improved the BTCR, with sensitivity depending on the perfusion pattern. In contexts with diffusive perfusion patterns, spatially registered and PCA-filtered PD-US images provide a reliable representation of blood perfusion, enabling the interpretation of low echo power regions as potentially ischemic.

2.5 Summary

PD-US imaging, without the need for contrast enhancement, is emerging as a valuable tool for monitoring changes in blood perfusion. Although PD-US methods do not provide quantitative perfusion measurements, they can effectively capture spatiotemporal variations in muscle perfusion when clutter and noise power are adequately minimized. This chapter has explored a spatial registration technique applied to echo signals before employing principal components analysis (PCA)-based clutter and noise filtering. The primary objective was to obtain PD-US images that reliably map relative perfusion. Through simulations of echo-signal frames, the study demonstrated the sub-sample spatial registration of echo frames before clutter filtering, even in the presence of clinical tissue motion. This spatial registration approach narrowed the eigen-spectrum of tissue clutter and enabled efficient PCA filtering, leading to minimized clutter power and enhanced echo SNR. It was observed that PD-US images could consistently represent relative perfusion and regional ischemia. In particular, spatially registered, PCA-filtered PD-US images were found to improve the specificity of the signal for true blood perfusion. The reliability of PD-US as an indicator of blood perfusion was further confirmed through simulation cases with both directed and diffusive perfusion patterns.

These findings suggest that spatial registration methods significantly enhance the dependability of PD-US imaging in representing tissue perfusion. In addition, PD-US images show potential for monitoring dynamic tissue changes, making them a promising tool for assessing PAD progression and evaluating responses to therapeutic interventions. In the subsequent phase of our study, we sought to investigate the feasibility of employing PD-US images for monitoring dynamic tissue changes. To achieve this goal, we conducted an in vivo experiment aimed at tracking muscle perfusion during brief episodes of ischemia in rodent models. This inquiry was undertaken to determine whether PD-US has the potential to enhance the assessment of PAD progression and evaluate responses to therapeutic interventions.

Chapter 3

Monitoring Muscle Perfusion in Rodents During Short-Term Ischemia Using PD-US

3.1 Study Overview

The present study [37] constitutes a pre-clinical investigation with the primary objective of demonstrating the capacity of Perfusion PD-US measurements to detect temporal changes in peripheral muscle perfusion. Given the unavailability of realistic phantoms that offer known perfusion states for experimentation, this study focuses on the examination of measurements taken from rodent hindlimbs, employing both invasive and non-invasive experimental methodologies. Both experimental approaches involve the utilization of anesthetized animals, in which the blood flow to the muscles in the right hindlimb is intentionally and temporarily modulated. The study seeks to elucidate the effectiveness of PD-US in capturing these dynamic changes in muscle perfusion and its potential application in monitoring such alterations. This research aims to contribute valuable insights into the applicability and reliability of PD-US as a tool for assessing perfusion dynamics in peripheral muscles, thus offering a foundation for potential future clinical investigations.

3.1.1 Invasive Perfusion Measurements

In the context of our study, the invasive perfusion measurements are specifically designed to investigate changes in deep-muscle perfusion. This examination is conducted by clamping the right iliac artery for a period of 30 seconds. The primary objective of this procedure is to establish a temporal correlation between perfusion changes occurring at the limb's surface and those deeper within the muscle tissue. This approach enables us to make direct comparisons between PD-US and Laser Speckle Contrast Imaging (LSCI) estimates of perfusion.

LSCI is a well-established technique frequently utilized to infer changes in hindlimb perfusion over time. It achieves this by analyzing temporal alterations in surface blood flow patterns [38] [39] [40] [41]. During the temporary occlusion of the iliac artery, blood flow to the limb is interrupted. Upon release of the vessel clamp, downstream muscle perfusion typically experiences a brief surge, exceeding baseline levels for a duration of less than 30 seconds. This phenomenon is referred to as reactive hyperemia (RH) and is induced as

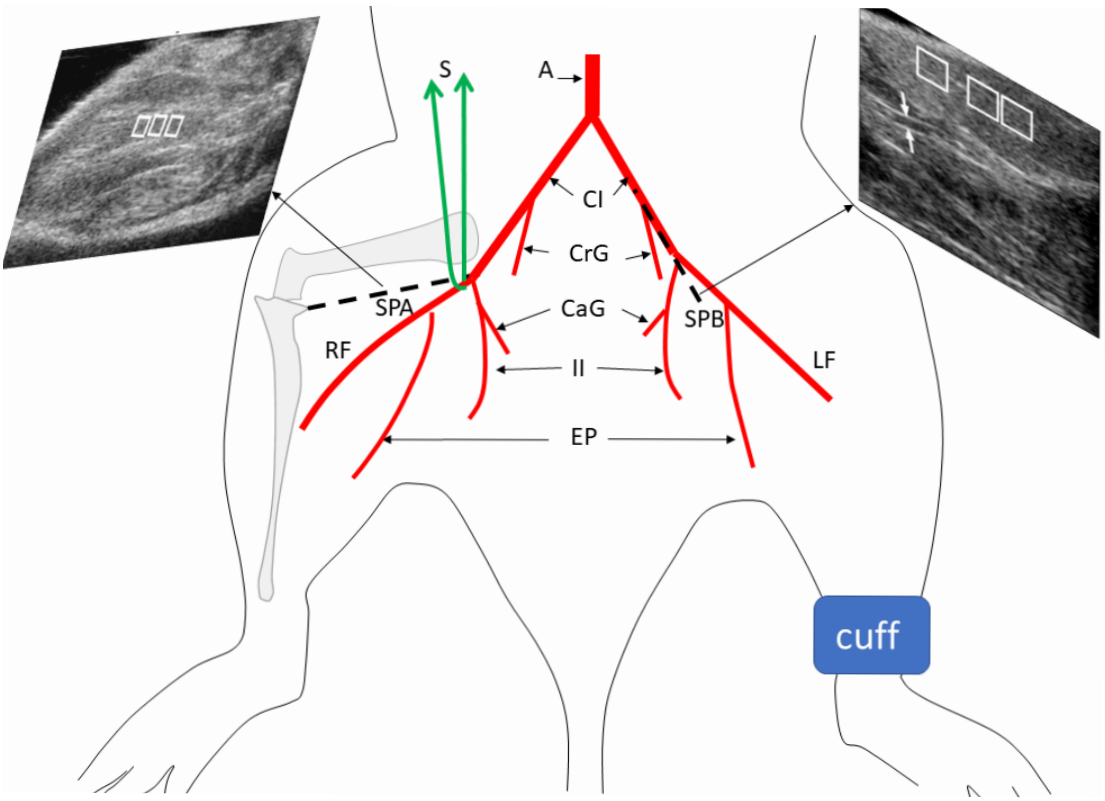

Figure 3.1: Key arteries in mouse hindlimbs include the aorta (A), common iliac arteries (CI), cranial gluteal arteries (CrG), caudal gluteal arteries (CaG), internal iliac arteries (II), external pudendal arteries (EP) and right femoral (RF) and left femoral (LF) arteries. The vessel geometry was drawn from dissection photos from Kochi et al. [43]. Green lines indicate suture (S) positioned at the site where an artery (and vein not shown) is clamped and released. The vessels are occluded by pressing down on the cylinder surrounding the suture, as indicated by the arrow. At ultrasonic scan plane A (SPA, dashed line), the B-mode image displays the three subregions (white boxes) selected for the invasive study. At scan plane B (SPB), the color flow (CF) image displays the three subregions selected for perfusion estimation in the non-invasive study. White arrows in that image indicate the vessel segment where arterial diameters are estimated. The distal positioning of the blood pressure cuff is also shown.

the ischemic stimulus triggers the production of shear-induced nitric oxide (NO), leading to the dilation of resistive vessels [42].

It is important to note that neither PD-US nor LSCI provides quantitative estimates of perfusion on an absolute scale. However, through our study, we aim to demonstrate the equivalence between the relative changes detected by these two modalities. These modalities are subject to highly correlated variations in tissue perfusion, allowing us to validate both methods. This validation process mirrors the way measurements from a realistic perfusion phantom are used to establish the accuracy and reliability of these techniques in quantifying perfusion changes.

3.1.2 Non-Invasive Perfusion Measurements

The non-invasive perfusion measurements within this study focus on the examination of variations in both arterial lumen diameter and muscle perfusion, observed simultaneously before and after inducing a more

extended ischemic period of 5 minutes in the hindlimb. This ischemic period is initiated by the application of external pressure via a pressure cuff. As the pressure in the cuff is rapidly reduced, a series of perfusion-related events unfold. Initially, there is a surge in blood flow, followed by a period of responsive hyperemia, during which perfusion remains elevated for several minutes. Responsive hyperemia is mediated and sustained by factors released during the initial surge of blood [42]. To monitor these changes in perfusion, we employ PD-US estimates. Additionally, we measure flow-mediated dilation (FMD) of the left femoral artery [44]. The primary objective of the non-invasive study is to observe alterations in the tone of resistive vessels, as indicated by the temporal variations in muscle perfusion, while simultaneously monitoring changes in the tone of conduit vessels.

The significance of this study lies in its ability to investigate the involvement of the endothelium in modifying vascular responses to muscle ischemia, both in diabetic animals and humans [45]. Blunted hyperemic responses in mammals serve as an indicator of endothelial dysfunction, which, in turn, predicts an increased risk of atherosclerosis and a higher incidence of cardiovascular events from various causes [42] [46] [47] [48]. Changes in the endothelial function of conduit arteries are associated with age and hypertension, while changes in the endothelial function of resistive vessels are indicative of risks associated with metabolic imbalances often associated with high body mass index and diabetes [46] [47] [48] [49].

3.2 Method

3.2.1 Mice Study

The procedures outlined in this section were conducted in accordance with the ethical guidelines and approved by the Institutional Animal Care and Use Committee (IACUC) of the University of Illinois at Urbana-Champaign.

For the mouse studies, we employed both invasive and non-invasive approaches to investigate perfusion dynamics.

Invasive Experiment

The invasive experiment involved two healthy male C57BL/6 mice, each 16 months old and weighing 45 grams (Charles River Laboratories, Thousand Oaks, CA, USA). After being anesthetized with 1% to 3% isoflurane, each mouse was gently restrained in a supine position on a rigid heating pad to minimize movements and maintain a constant body temperature of 37°C. To ensure clear access to the hindlimb vasculature, body hair from the inner thighs was removed using a depilatory cream.

The vasculature was exposed through a small skin incision, performed using micro-scissors and blunt dissection. A 6-O silk suture was placed around the artery and vein near the iliac-femoral artery junction, passing through a small plastic cylinder, as indicated in Figure 3.1. At the predetermined time, both vessels were temporarily clamped for 30 seconds by gently pushing down on the cylinder while pulling up on the suture. Due to the presence of numerous collateral vessels, the degree of ischemia varied within the hindlimb. The clamp was released, visibly restoring conduit vessel flow. During this procedure, LSCI or PD-US images of the hindlimb muscles were recorded.

Non-Invasive Experiment

The non-invasive study involved five male and five female C57BL/6 mice. Two of the male mice were also part of the invasive study. The anesthetization and scanning preparation were identical to the procedures previously described. Instead of surgery, a 5-minute period of partial ischemia was induced using an inflatable cuff placed on the lower limb (refer to Figure 3.1).

Hemodynamic responses were measured both before and during cuff inflation and for 5 minutes after rapid cuff deflation.

Flow Mediated Dilation (FMD)

FMD values were determined from 24 MHz US B-mode images by measuring the fractional change in the femoral artery cross-sectional diameter. The diameter measured during a pre-occlusion baseline period (D_b) and during peak hyperemic dilation after cuff release (D_a) were combined to estimate FMD as follows:

$$FMD = \frac{D_a - D_b}{D_b} \tag{3.1}$$

Reactive Hyperemia (RH)

The post-occlusion RH, measured in decibels (dB), was estimated in muscle by calculating the ratio of the peak PD-US value after cuff pressure was released to the baseline PD-US value before occlusion:

$$RH = 10 \log \left(\frac{\text{peak}}{\text{baseline}} \right) \tag{3.2}$$

In equation 3.2, RH = 0 dB indicates no change in perfusion, while RH = $\pm$3 dB indicates approximately a doubling or halving of perfusion relative to the baseline value.

Exercise Regimen

In this subsection, we detail the exercise regimen employed in our study, which involved three out of the five healthy male and female mice included in the noninvasive investigation. The goal was to assess the impact of exercise conditioning on vascular function, specifically endothelial-dependent vasodilation, as measured by FMD and RH responses.

The "exercised mice" group underwent a comprehensive cardiovascular conditioning program over the course of two weeks. The conditioning regimen consisted of forced swimming, a well-established exercise model known for its cardiovascular benefits [50]. The exercise protocol was progressively intensified, with the mice initially swimming for only a few minutes each day and gradually increasing to a total of 60 minutes per day over the course of one week. In the final two weeks leading up to the experiment phase, each mouse consistently swam for 60 minutes per day.

FMD and RH measurements were acquired from both the "exercised" and "non-exercised" groups of male and female mice. It's important to note that our study considered the potential impact of biological variables such as sex and exercise fitness level. Previous research has suggested that perfusion levels may exhibit variations in response to the sex of the animal and the level of exercise conditioning [51]. Therefore, these variables were scrutinized in our non-invasive investigations to provide a comprehensive evaluation of the effects of exercise on vascular function.

3.2.2 Rat Study

Next, we'll explore the findings from our rat studies, which aimed to replicate the invasive vessel-clamping experiments conducted in mice, and additionally, we incorporated measurements of FMD. The rat study involved two male Sprague-Dawley rats, both 9 months of age, with an average body weight of 980 grams. This animal model was selected to provide insights into perfusion dynamics that could be translated to clinical relevance. In the rat study, we investigated muscle perfusion using PD-US measurements, both before and after the application of lidocaine. The purpose of applying lidocaine was to reduce the tone of resistive vessels in the muscles fed by the clamped vessel, thus modifying the vascular response [52].

The surgical preparation for the rat study closely paralleled that of the mice; however, one notable difference was the removal of the skin from the right leg before clamping. This modification allowed us to apply a 1% lidocaine hydrochloride (HCl) solution (10 mg/mL vial without epinephrine, Hospira, Inc., Lake Forest, IL, USA) topically to the exposed area. Subsequently, we proceeded to measure the femoral artery diameter and muscle perfusion at various time points, including before, during, and after clamping the right iliac artery. This measurement series was performed twice: once before the application of lidocaine and again 10 minutes after lidocaine was administered. It's worth noting that the application of lidocaine as a vasodilator was based on its molecular weight of 234.3 g/mol and concentration of 0.0437 M. At this concentration range, lidocaine has vasodilatory properties, as documented in the literature [53].

The findings from these rat studies contribute to our understanding of vascular responses and their modulation by the application of lidocaine.

3.2.3 Laser Speckle-Contrast Imaging

Laser speckle-contrast imaging is a valuable technique used to assess blood flow and perfusion in tissues. In our study, laser speckle-contrast images were acquired using a moorFLPI-2 laser perfusion imager, manufactured by Moor Instruments in Devon, UK. The system was operated through a Windows-based PC using the moorFLPI software (moorFLPI Measurement, version 1.1, Moor Instruments).

The fundamental principle behind laser speckle-contrast imaging involves the assessment of blood flow to a tissue's superficial layers, typically to a depth of approximately 1 millimeter. This is achieved by illuminating the skin surface with near-infrared (NIR) laser light at a wavelength of 785 nanometers. When the laser light interacts with the tissue, coherent backscattered photons create an interference pattern known as a speckle pattern. This speckle pattern undergoes changes based on the motion of blood cells within the tissue.

One key parameter of interest is speckle contrast, which is defined as the ratio of the SD to the mean photon intensity. Speckle contrast values are inversely related to blood cell motion within the tissue: higher speckle contrast corresponds to less motion, whereas decreasing speckle contrast indicates increased blood cell movement. This relationship is integral to the assessment of perfusion and blood flow dynamics within the imaged tissue [39] [54]. Speckle contrast is at its highest when the medium being imaged is relatively static and composed of random scatterers that do not move significantly. As motion within the tissue increases, the coherence of the detected photons decreases, resulting in reduced speckle contrast. In the final output, the laser speckle-contrast image is displayed as a color representation of regional speckle contrast, providing visual insights into the perfusion characteristics of the imaged area.

For the experiments conducted in our study, the moorFLPI-2 system was prepared and configured in accordance with the manufacturer's guidelines to ensure reliable and accurate results. A high-resolution 576 $\times$ 768 pixel CCD camera was employed, capturing the near-infrared photon flux from the tissues at a rapid

frame rate of 25 frames per second (fps). To mitigate noise and improve data quality, a sequence of frames was recorded over a period of 94 seconds in mice. Subsequently, these frames were processed by averaging them in 2-second or 4-second intervals.

Laser speckle-contrast imaging serves as a valuable tool in our study, offering insights into tissue perfusion dynamics and contributing to our assessment of vascular responses and endothelial function.

3.2.4 Ultrasonic Acquisition

The acquisition of ultrasonic data is a fundamental aspect of our study, allowing us to gain insights into perfusion dynamics and vascular responses. To perform these measurements, we utilized a Vevo 2100 US imaging system (FUJIFILM VisualSonics Inc., Toronto, ON, Canada) in conjunction with an MS400 linear-array probe that transmits 24-MHz pulses. This high-frequency probe is particularly suitable for capturing detailed information from the hindlimb muscles and vessels, providing us with the necessary data for our research.

The US system records echo signals from the hindlimb muscles and vessels, and the raw data collected, known as in-phase and quadrature (IQ) pulse-echo data, are subjected to offline processing using our custom software. This software plays a crucial role in estimating PD-US signals [24] and generating perfusion images [26]. By leveraging this approach, we can accurately assess blood flow and perfusion in the targeted regions of interest.One important technical aspect of our data acquisition is the need for stability and precision. To eliminate any hand-induced motion or jitter during scanning, we rigidly mounted the US probe above the limb. This approach is particularly critical in ensuring the accuracy of our measurements. The reduction of motion artifacts is essential for reliable and reproducible results, as discussed by Tierney et al. in their work on jitter reduction processing for freehand scanning applications [25].

For the vascular clamping experiments, we selected a specific scan plane that is both anatomically relevant and well-suited to our research objectives. This scan plane is parallel and medial to the femur and is located within the gracilis anterior muscle, aligned along the muscle fibers (as illustrated in SPA in Figure 3.1). To ensure the successful reproduction of the scan plane and the precise acquisition of images of muscle tissue, a systematic protocol was employed. This protocol aimed to maintain consistency and accuracy in our US imaging.

The following steps were followed to achieve the desired scan plane for muscle tissue imaging:

1. **Femur-Centric Scan Plane:** The initial step involved acquiring a scan plane that offered a comprehensive view of the femur, a prominent anatomical reference point.

2. **Position Adjustment:** Subsequently, the US transducer was carefully adjusted by moving it toward the tail of the mouse. This adjustment continued until the entire femur bone was no longer visible within the scan plane. The disappearance of the femur in the US image indicated that the transducer was positioned beyond the bone.

3. **Desired Muscle Tissue Location:** The new location of the transducer, where the femur bone had completely disappeared from view, was the scan plane specifically chosen for imaging the target muscle tissue. This location allowed us to focus on the desired region with accuracy and precision.

By implementing this standardized protocol, we ensured that the scan plane was consistently positioned for imaging the muscle tissue of interest. This approach minimized variability and contributed to the reliability of our US data acquisition, ultimately enhancing the quality of our research findings. This positioning allows

us to focus on the regions of interest in a consistent and standardized manner. To maintain consistency in our analysis, we selected three specific 1 mm^2 regions within the chosen scan plane for perfusion estimation. These regions are located at a depth of approximately 3 mm within the muscle tissue. The ultrasonic attenuation in this scenario was measured at 3.6 dB. It's important to note that the attenuation losses remained constant across all measurements, eliminating the need for additional corrections.

During cuff inflation, a different scan plane (SPB in Figure 3.1) was selected, which included a long-axis segment of the internal femoral artery along with the adjacent muscle. This approach ensures that we capture the relevant anatomical structures during the experiments, facilitating our assessment of vascular responses and perfusion dynamics. The robust and precise ultrasonic acquisition method employed in our study is foundational to our research, enabling us to obtain high-quality and reproducible data for our investigations into vascular function and perfusion in the hindlimb muscles. This meticulous approach provides a solid foundation for our subsequent analysis and interpretation of results.

3.2.5 Data Structures

The data collected for perfusion estimation in our study are organized as follows:

Doppler-Frame Ensembles

Each data set gathered for perfusion estimation consists of 96 Doppler-frame ensembles, as illustrated in Figure 3.2. These ensembles are recorded in color mode over a 12-second duration, capturing eight ensembles per second. Each ensemble is comprised of 17 individual color-mode frames, recorded at an effective frame rate of 10^3 fps. However, for our PD-US measurements, we use only the first color-mode frame in each Doppler ensemble. This results in an effective frame rate of 8 fps for our PD-US measurements.

IQ Echo Frame Details

Each IQ echo frame has a total area of 6.71 $\times$ 15.1 mm, with a depth-sampling interval of 0.031 mm and a lateral-sampling interval of 0.060 mm. Converting IQ data to RF echo data results in upsampling of the RF signal by a factor of 16 along the beam axis (fast time). Consequently, the axial (depth) and lateral sampling intervals for each RF data frame are 0.0019 $\times$ 0.060 mm, and each RF color-mode frame consists of 3531 $\times$ 252 pixels. In our procedures, three subregions are selected in one muscle from these data. The B-mode spatial resolution at 24 MHz is 0.085 mm axially and 0.15 mm laterally.

Invasive Procedure Data Collection

In the invasive procedure, once the vessels are surgically exposed and the suture is properly positioned, a baseline data set is recorded from the muscle tissue, lasting 12 seconds (equivalent to 96 frames). As the vessel is clamped, an occlusion-period data set, also lasting 12 seconds, is recorded. After 30 seconds of clamping, the clamp is released, and the first 12-second recovery data set is recorded from the same tissues. Additional recovery data sets are recorded every 30 seconds until perfusion achieves a steady-state condition. Steady-state perfusion is assumed to occur 10 seconds after changes in the artery diameter cease. It's important to note that 18 seconds are required to upload each 12-second echo-data set before another can be recorded in research mode.

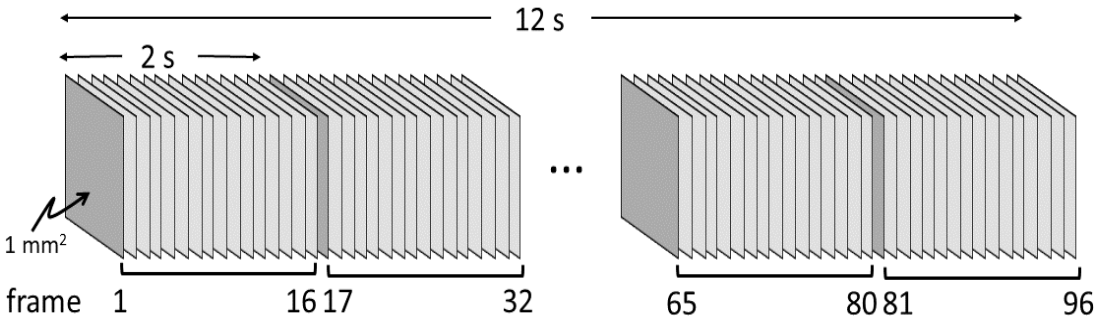

Figure 3.2: Temporal partitioning of an echo data set for one spatial subregion. The 96 frames (12 s) are parsed into six groups of 16 (2 s each). Each group of 16 frames is spatially registered to the first frame in that group and clutter filtered, and the residual signal power is computed. The mean over three subregions with a total area 3 mm2 is converted to decibels and displayed as data points in Figure 3.4.

Non-Invasive Procedure Data Collection

In the non-invasive procedure, a pressure cuff is positioned on a hindlimb immediately above the foot, as illustrated in Figure 3.1. Prior to cuff inflation, a 12-second baseline data set is recorded on the cuffed hindlimb, which includes a long-axis view of the femoral artery and muscle tissue (as seen in SPB in Figure 3.1). Each acquisition during this phase includes color-mode data for PD-US measurements and B-mode data for vessel diameter estimation. The cuff is quickly inflated and held at a pressure higher than the level at which the systolic pulse sounds are silenced for 5 minutes. During the occlusion phase, a 12-second data set is acquired every minute. After 5 minutes, the cuff is rapidly deflated to restore limb circulation, and 12-second data sets are acquired every minute for 5 minutes.

These specific data structures and acquisition procedures are integral to our research, enabling us to assess perfusion and vascular responses in a controlled and systematic manner.

3.2.6 Power Doppler (PD) Estimation

In our research, all ultrasonic signal processing and image formation computations were carried out using MATLAB R2021b (The MathWorks, Inc., Natick, MA, USA) applied offline to the recorded echo data. The following section provides a detailed account of the methods and techniques employed in PD estimation.

Subregion Selection

To ensure the accuracy of our PD estimation, subregions were carefully chosen within the B-mode image. These subregions were selected to have visibly uniform speckle, with special attention to avoiding vessels and muscle fascia. Each subregion was parsed in time, as illustrated in Figure 3.2.

Conversion to RF Echo Data

The initial step involved converting IQ echo data to RF echo data using the method and parameter values recommended by the manufacturer. This transformation allowed us to prepare the data for subsequent analysis.

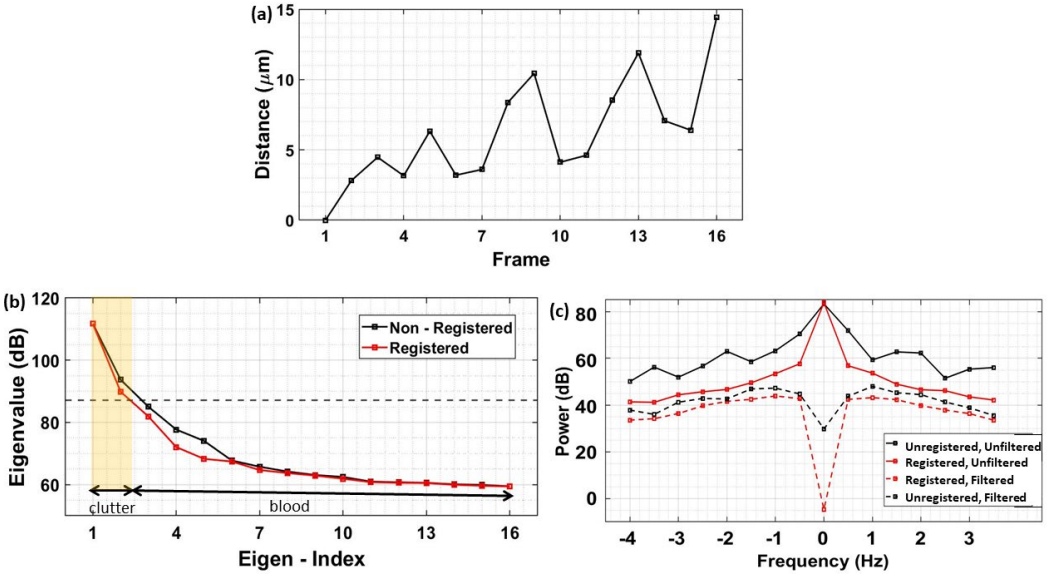

Figure 3.3: (a) Example of in-plane displacements measured in hindlimb mouse muscle for each of 16 frames relative to the first, as detected during spatial registration. Distance is determined from axial and lateral displacements found during registration. (b) The corresponding PCA singular spectra obtained before (black) and after (red) spatial registration. After registration, a clutter filter threshold (dashed line) is applied to distinguish the clutter subspace (shaded region) from the blood subspace; singular values greater than the threshold are considered clutter. (c) Doppler spectra are plotted before (black) and after (red) spatial registration and before (solid) and after (dashed) PCA clutter filtering. PD-US signals are areas under the filtered Doppler spectrum on a linear scale.

3.2.7 Spatial Registration

Spatial registration of the RF echo frames within each subregion was performed to ensure the alignment of data frames. The 96 RF frames were partitioned into six groups, each consisting of 16 frames. The choice of 16 frames per group, corresponding to 2 seconds of echo data, struck a balance between the requirement for high temporal resolution and the need for noise suppression through frame averaging. The displacement needed to realign each RF frame with the first frame in its group was computed. A continuous rigid-body spatial registration method was then employed to eliminate the in-plane translation estimated for each subregion. This method was based on techniques described in the previous chapter [24].

Typical in vivo motion primarily stems from diaphragmatic breathing, where hindlimb muscles exhibit cyclic motion at respiration rates, covering a distance of less than 0.025 mm and mostly along muscle fibers oriented approximately parallel to the lateral axis of the transducer. Given the speed of capillary flow in muscle (typically less than 2 mm/s) and a SNR of 15 dB under typical scanning conditions [24], averaging perfusion over 2 seconds and 3 mm^2 of tissue resulted in acceptable PD-US estimation precision. If needed, the precision of power estimates could be further enhanced by averaging more echo frames from each Doppler frame.

In-Plane Displacements

The net in-plane displacements for a typical group of 16 frames were analyzed. In a representative case (see Figure 3.3 a, the measured displacement exhibited oscillation in the scan plane at a rate of 2 breaths per second, corresponding to a 4-frame period at 8 fps. In this scenario, the linear trend in displacement indicated that the tissue also translated along a line within the scan plane. It's important to note that hindlimb motion resulting from vessel clamping and release was substantially greater than the respiratory motion (see Figure 3.3 a) observed. Spatial registration was employed instead of respiratory gating because respiration was just one of several sources of tissue motion.

Residual Signal Power

Once the 16 frames were spatially aligned and subjected to PCA filtering, the residual signal power was computed. Rigid registration ensured that the clutter signals were aligned without distorting the blood signals. This was feasible because coherent tissue clutter dominated each recording, with tissue backscatter being approximately 14 dB greater than blood backscatter at 20 MHz [32] [55]. Only spatially coherent tissue movements were registered by these means. In this comprehensive process of PD estimation, careful considerations were made to preserve data quality and accuracy, ensuring the reliability of our findings in the assessment of perfusion and vascular responses.

3.2.8 Quality of PD-US Estimates

In our study, the quality of PD-US estimates plays a critical role in the accuracy of perfusion assessment. Herein, we will address the factors that influence the quality of PD-US estimates and how we ensure reliable perfusion descriptors.

Challenges with Tissue Echo Decorrelation

One of the key challenges in PD-US estimation is the presence of large out-of-plane tissue movements and substantial in-plane tissue deformation. These dynamic tissue behaviors lead to the decorrelation of tissue echoes between consecutive frames. Unlike in-plane translations, this type of tissue-echo decorrelation cannot be effectively recovered through rigid registration methods. Consequently, a portion of the tissue-echo signal power remains coupled to the blood echoes in the PCA singular spectrum, resulting in incomplete clutter filtering.

Inter-Frame Correlation Coefficient

The inter-frame correlation coefficient, denoted as ρ and taking values between 1 (perfect correlation) and -1 (perfect anti-correlation), serves as a crucial indicator of the separability of clutter and blood signal power. This coefficient, introduced in previous chapter [24], provides valuable insights into the effectiveness of PCA clutter filtering. A higher ρ indicates a better separation between clutter and blood signal power, which is essential for accurate perfusion assessment.

Mitigating Spatial Registration Errors

To reduce spatial registration errors stemming from tissue-echo decorrelation, we employ a practical strategy. By averaging displacements over 3 mm^2 regions, we can mitigate the impact of tissue-echo decorrelation on

the quality of PD-US estimates without significantly compromising the stationarity of tissue echoes. This approach helps to enhance the reliability of perfusion descriptors.

Criteria for Valid PD-US Estimates

For a PD-US estimate to be considered a valid perfusion descriptor, specific criteria must be met. These criteria are designed to ensure that the PD-US estimates faithfully represent perfusing-blood signal power:

1. The recorded signals in each frame before clutter filtering must be dominated by tissue echoes recorded at high echo SNR.

2. Any tissue motion between frames must be describable as a rigid translation within the scan plane.

When these assumptions are met, and in-plane deformation or significant out-of-plane tissue motion is minimized, the inter-frame correlation (ρ) will be sufficiently high. The criterion for considering a PD-US estimate as a valid perfusion descriptor is that the correlation coefficient (ρ) between the first frame and other frames in each post-registration group must exceed 0.9. This threshold ensures that the PD-US estimates accurately reflect the perfusion dynamics under investigation.

In summary, the quality of PD-US estimates is a crucial aspect of our perfusion assessment methodology. By addressing issues related to tissue-echo decorrelation, employing the inter-frame correlation coefficient, and adhering to specific criteria, we maintain the reliability and validity of our PD-US-derived perfusion descriptors.

3.2.9 Determining the Blood-Echo Subspace in the PCA Singular Spectrum

Proceeding to the process of determining the blood-echo subspace within the PCA singular spectrum a crucial step in our perfusion assessment methodology.

Clutter Echo Elimination

Clutter echoes, which primarily stem from tissue movements and other sources of interference, are effectively eliminated by selectively setting to zero all singular values outside the blood-echo subspace. This crucial step is visually illustrated in Figure 3.3 b. After applying this filtering operation, the remaining signal power within the filtered 16-frame group is attributed to the echo signals resulting from spatially diffuse blood cell motion and any associated acquisition noise (as seen in Figure 3.3 c).

Identifying the Clutter-Blood Subspace Boundary

The process of determining the boundary that separates the clutter and blood subspaces within the singular spectrum is carried out in a relatively straightforward manner. Prior to the application of rigid registration, the intense signal generated by moving clutter is dispersed across the first 5 of 16 singular values, as exemplified in Figure 3.3 b (indicated by the black spectral line). This broad tissue clutter component substantially overlaps with the blood perfusion component in the singular spectrum. Upon successful spatial registration (determined when ρ 0.9), the clutter and blood subspaces become more separable, and the energy of the clutter signal becomes more concentrated within the initial singular values (as indicated by the red spectral line in Figure 3.3 b). Singular values within the clutter subspace are subsequently set to zero, effectively filtering out the clutter-signal power from the echo signal.

Empirical Setting of the Clutter-Blood Threshold

The lower singular-spectrum threshold between the clutter and blood subspaces is determined empirically for each 16-frame subregion after registration. This is achieved by identifying and discarding singular values that exceed 0.4% of the first singular value within that group on a linear scale (i.e., -24 dB), as represented by the dashed horizontal line in Figure 3.3 b. In contrast, an upper spectral threshold between the blood and noise subspaces is not explicitly set. Previous findings have indicated that these components do not reliably separate for diffuse perfusion patterns at typical echo SNR values [24]. Consequently, the upper end of the singular spectrum remains unfiltered. The influence of noise power on changes in perfusion measurements relative to baseline values is minimal, particularly for the data illustrated in Figures 3.4 and 3.6.

3.2.10 Doppler Spectrum Analysis after Spatial Registration and PCA Filtering

In this section, we discuss the analysis of the Doppler spectrum following spatial registration and PCA filtering. The Doppler spectrum, after processing, is presented in Figure 3.3 c as the dashed red curve. This figure serves to highlight the significant disparity in estimated power spectra when comparing measurements before and after spatial registration, even though the in-plane tissue translation in Figure 3.3 a is merely 0.015 mm. Notably, the application of PCA filtering demonstrates its effectiveness in mitigating stationary contributions within the Doppler spectrum, specifically at 0 Hz. These stationary components encompass the signal power arising from echoes of static blood cells. To estimate the static blood power, we perform interpolation on the zero-frequency term within the registered and filtered Doppler spectrum shown in Figure 3.3 c. It is important to note that while interpolation consistently increases the PD-US estimates in Figures 3.4 – 3.6, this adjustment does not introduce any alterations to the relative perfusion changes that are under observation. As such, interpolation was not employed in the reported results.

Frame Rate Considerations

Turning our focus to discuss considerations related to frame rates in Doppler US data acquisition. Specifically, the analysis pertains to the processing of 2 seconds of echo data sampled at 8 fps, which enables the capture of 16 Doppler frequencies within a range of ± 4 Hz and a frequency resolution of 0.5 Hz, as depicted in Figure 3.3 c. The conversion between Doppler frequency and blood velocity denoted as v in millimeters per second (mm/s), is achieved by applying the pulsed Doppler equation in relation to the speed of sound, c:

$$v[\text{ mm/s}] = (c/2[\text{ mm}/\mu\text{s}]) \times (\text{ Dopplerfrequency [Hz]/ pulsefrequency [MHz]}) \tag{3.3}$$

Equation 3.3 highlights that a frequency resolution of 0.5 Hz yields a blood cell velocity resolution of 0.016 mm/s for a 24 MHz US pulse. This resolution is deemed acceptable for capturing capillary perfusion in muscle, particularly for velocities within the range $|v| < 2$ mm/s. It is important to note that this frame rate, although sufficient for various applications, is not high enough to prevent aliasing of the fastest blood velocity components. Nonetheless, it should be emphasized that aliased signal power can still be accurately estimated, as indicated by previous studies [56]. However, the 8 fps frame rate proves to be adequate for capturing mouse respiratory motion without the occurrence of aliasing, ensuring an accurate representation of this vital physiological parameter.

3.2.11 PD-US Imaging

Up to this point, we have discussed the characterization of time-varying perfusion in 2-second intervals based on spatially averaged PD-US estimates derived from a uniform region of ultrasonic speckle. Additionally, PD-US perfusion images can be generated using similar processing methods. To create a PD-US perfusion image, a subregion (20×20 samples, measuring 0.6 mm axially by 1.2 mm laterally, with a 1/3 spatial overlap) is systematically scrolled over the entire frame, following the procedure described by Kim et al. [57]. The signal processing techniques remain consistent with those previously described. These PD-US values are then superimposed as a color overlay on black-and-white B-mode images, as exemplified in Figure 3.5b.

3.2.12 Statistical Analyses

The values presented in Figures 3.4 - 3.7 represent sample means. The error bars accompanying these values indicate either ± 1 sample SD (SD) or ± 1 standard error (SE), as specified in the respective text and figure captions. When comparing paired groups, two-sided Student t-tests are utilized, with differences considered statistically significant at a significance level of $p < 0.05$. It is important to note that sample statistics and hypothesis testing results may vary depending on the sample size (N) reported for each measurement.

3.3 Results

This section presents the results obtained from invasive and non-invasive perfusion measurements conducted in mice.

3.3.1 Invasive Measurements in Mice

Figure 3.4 illustrates the results of invasive perfusion measurements for one of the mice under examination. Each PD-US data point in Figure 3.4 b is derived from a group of 16 echo frames averaged over a muscle subregion, resulting in a spatiotemporal mean value over 2 seconds within the 3 mm^2 muscle area, as depicted in Figure 3.5 b. The clusters of PD-US estimates displayed in Figure 3.4 a and 3.4 b represent a cumulative 12 seconds of perfusion data. The intervals between these point clusters correspond to the periods during which echo data is uploaded.

The LSCI estimates presented in Figure 3.4 c denote values averaged over 2 or 4-second intervals within four distinct surface regions, as indicated in Figure 3.5 c. Regions 3 and 4 in LSCI are designed to avoid the influence of large surface vessels found in regions 1 and 2. Region 1 encompasses the entire upper hindlimb, including regions 3 and 4, while region 2 pertains to the lower hindlimb (foot) region. These results provide valuable insights into the perfusion dynamics within the examined mouse model, as well as the comparative analysis between PD-US and LSCI measurements.

Correlation Coefficients

Figure 3.4 a illustrates the minimum correlation coefficient (ρ) between the first frame and each of the other 15 frames in the group, both before (black) and after (red) the spatial registration of the echo frames. When $\rho \geq 0.9$ at specific measurement times, it indicates that tissue clutter within the 16 frames is essentially motionless. The slight decorrelation that is observed is attributed to diffuse blood motion and acquisition

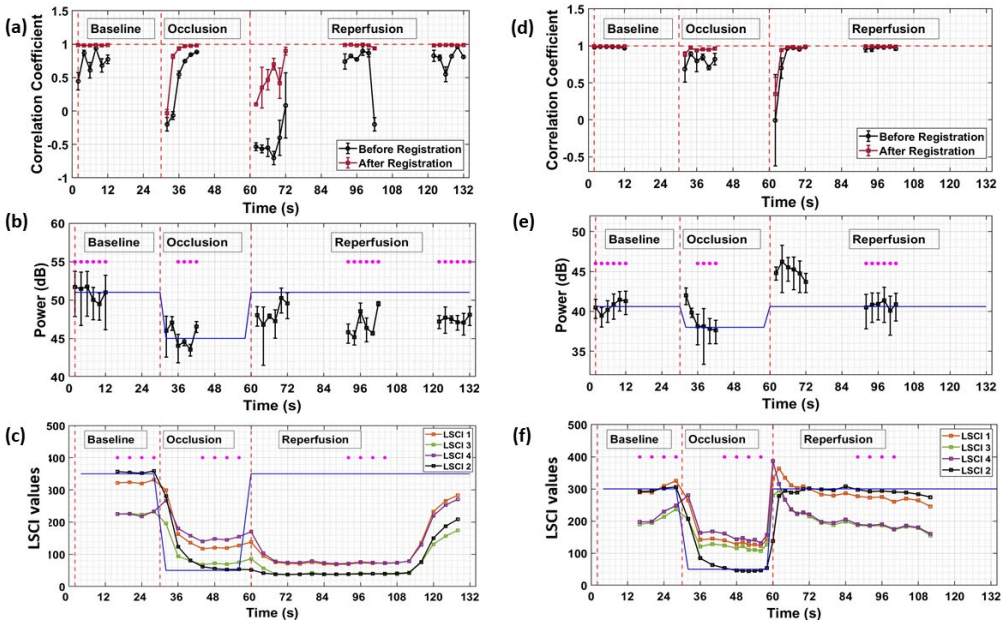

Figure 3.4: Measurements for one female mouse (a-c) and one male mouse (d-f). The minimum correlation coefficient ρ between frame pairs in the 16-frame group before filtering are shown before and after spatial registration in (a) and (d). PD-US measurements are shown in (b) and (e); the mean signal power over 2 s from three subregions ± 1 SD are plotted. LSCI results in (c) and (f) are measurements from hindlimb regions 1-4 as marked in Figure 5d. The LSCI are averaged over 4 s intervals (100 frames) to give each point, except between measurement times 48-72 s in the male mouse, where the averaging interval was reduced to 2 s to capture the hyperemic response. Magenta points indicate valid PD-US measurements ($\rho > 0.9$) during steady-state perfusion. These values formed the mean bar-plot measurements in Figures 5a and b. The blue curves in (b,c,e,f) are descriptive only to indicate the vessel clamping period.

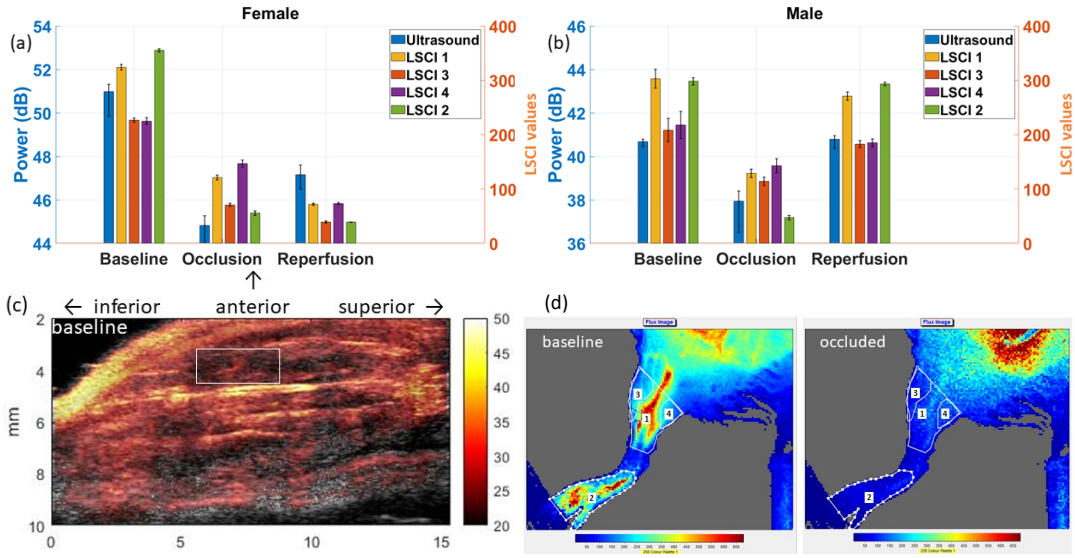

Figure 3.5: Plots (a) and (b) show the spatiotemporally averaged PD-US signal power (blue bars) from the muscle region of a PD-US image indicated in (c), and LSCI values from the four hindlimb subregions indicated in the LSCI of (d). Data shown are the mean ± 1 SE for two female (a) and two male (b) mice, including the data of Figure 4. Notice the similarity of the baseline and reperfusion measurements for the male mice, which is a pattern not seen for the female mice.

noise. When $\rho \geq 0.9$, it is expected that PCA filtering will effectively reduce clutter power, thereby allowing the PD-US measurements to reliably track the average perfusion within that muscle region.

Measurements taken at times when there are substantial differences between ρ values measured before (black) and after (red) spatial registration indicate the presence of significant in-plane tissue motion, which has been accurately aligned by the registration software. At the few instances where $\rho < 0.9$ after registration, PD-US values are considered questionable estimates of perfusion since they contain significant levels of residual clutter power. These points typically coincide with clamping transition times and are excluded from the average values presented in Figure 3.5 a. It is worth noting that as mentioned in the previous chapter [24], registration errors caused by reduced inter-frame correlation can be partially mitigated by employing spatial averaging over larger areas, provided that the tissue echoes remain wide-sense stationary.

PD-US and LSCI Perfusion Measurements

Next, we'll present the results of perfusion measurements obtained through PD-US and LSCI techniques.

PD-US and LSCI estimates, as depicted in Figure 3.4 b and 3.4 c, respectively, provide insights into temporal changes in both deep muscle and surface perfusions. Magenta points in Figure 3.4 b highlight valid PD-US estimates at steady-state values, whereas the initial 30 seconds post-occlusion period reflects the transient hyperemic response. LSCI measurements characterize temporal changes in superficial tissue perfusion, where the top half of the approximately 1mm depth of light penetration comprises skin tissue, possibly including large vessels [58], and the bottom half represents muscle tissue.

Figure 3.5 a presents estimates of changes in perfusion relative to baseline, derived from Figure 3.4 b and 3.4 c, using a linear scale. Three distinct time periods are identified: steady-state perfusion values during

pre-occlusion baseline, clamped-vessel occlusion, and post-hyperemic reperfusion recovery. The bars in Figure 3.5 a indicate means ±1 SE. Figure 3.4 b demonstrates that 6 seconds after vascular clamping, the PD-US signal power reduced to 53% of the baseline value (2.8 dB). Similarly, Figure 3.4 c shows that 6 seconds after vascular clamping, the LSCI values in regions 3 and 4 of Figure 3.5 d decreased to 63% of baseline. LSCI regions 1 and 2 exhibited greater reductions, reaching 42% and 16%, respectively, owing to the inclusion of large surface vessels. The LSCI values from regions 3 and 4, which exclude large surface vessels, are most comparable with the PD-US estimates, and further discussion will focus on this aspect.

Upon the release of the clamped artery at $t = 60$ seconds, the PD-US signal increased to 3.1 times the baseline (5 dB). The high correlation coefficient ($\rho > 0.9$) suggests successful clutter filtering, instilling confidence in the post-ischemic hyperemic response for PD-US estimates. LSCI data in regions 3 and 4 of Figure 3.4 c follow a similar pattern, with a peak hyperemic response of twice the baseline. To emphasize the surface hyperemic response, LSCI data were averaged over 2-second intervals (rather than 4 seconds) for recording times within the range $48 \leq t \leq 72$ seconds. Both PD-US and LSCI perfusion data returned to values within 5% of their respective baselines before 30 seconds.

3.3.2 Non-Invasive Measurements in Mice

The results of non-invasive experiments are presented in Figure 3.6. The left column of plots (Figure 3.6 a – 3.6 d) provides a summary of measurements of the femoral artery diameter taken before, during, and after 5 minutes of partial hindlimb ischemia, which was induced by inflating the pressure cuff. All measurements are expressed relative to the mean baseline arterial lumen values listed in Table 3.1. The right column of plots (Figure 3.6 e – 3.6 h) presents the PD-US time series describing muscle perfusion. These PD-US values, in decibels (dB), have been normalized by baseline measurements. It's worth noting that this data was recorded simultaneously with the artery diameter measurements. The results for non-exercised mouse groups (with $N = 2$ individuals each for males and females) can be observed in Figure 3.6 a, 3.6 b, 3.6 e and 3.6 f. Meanwhile, results for the exercised mouse groups (with $N = 3$ individuals each for males and females) are presented in Figure 3.6 c, 3.6 d, 3.6 g, and 3.6 h. These non-invasive measurements provide valuable insights into the response to partial hindlimb ischemia in both non-exercised and exercised mouse groups, allowing for a comparative analysis of arterial diameter changes and muscle perfusion responses.

	Exercised (N = 3)	**Non-exercised (N = 2)**	**Without lidocaine (N = 2)**	**With lidocaine (N = 2)**
Female mice	0.310 ± 0.005	0.308 ± 0.004	–	–
Male mice	0.324 ± 0.002	0.310 ± 0.004	–	–
Male rats	–	–	0.510 ± 0.019	0.518 ± 0.015

Table 3.1: Measurement of baseline femoral artery diameters. N, number of animals studied in each group.

FMD Estimates

Here, we present a detailed analysis of FMD estimates, a key parameter in assessing vascular function. FMD measurements were obtained from the mean femoral artery lumen diameter using a long-axis view in a 24 MHz B-mode image. The results are presented in Figure 3.6 a–d.

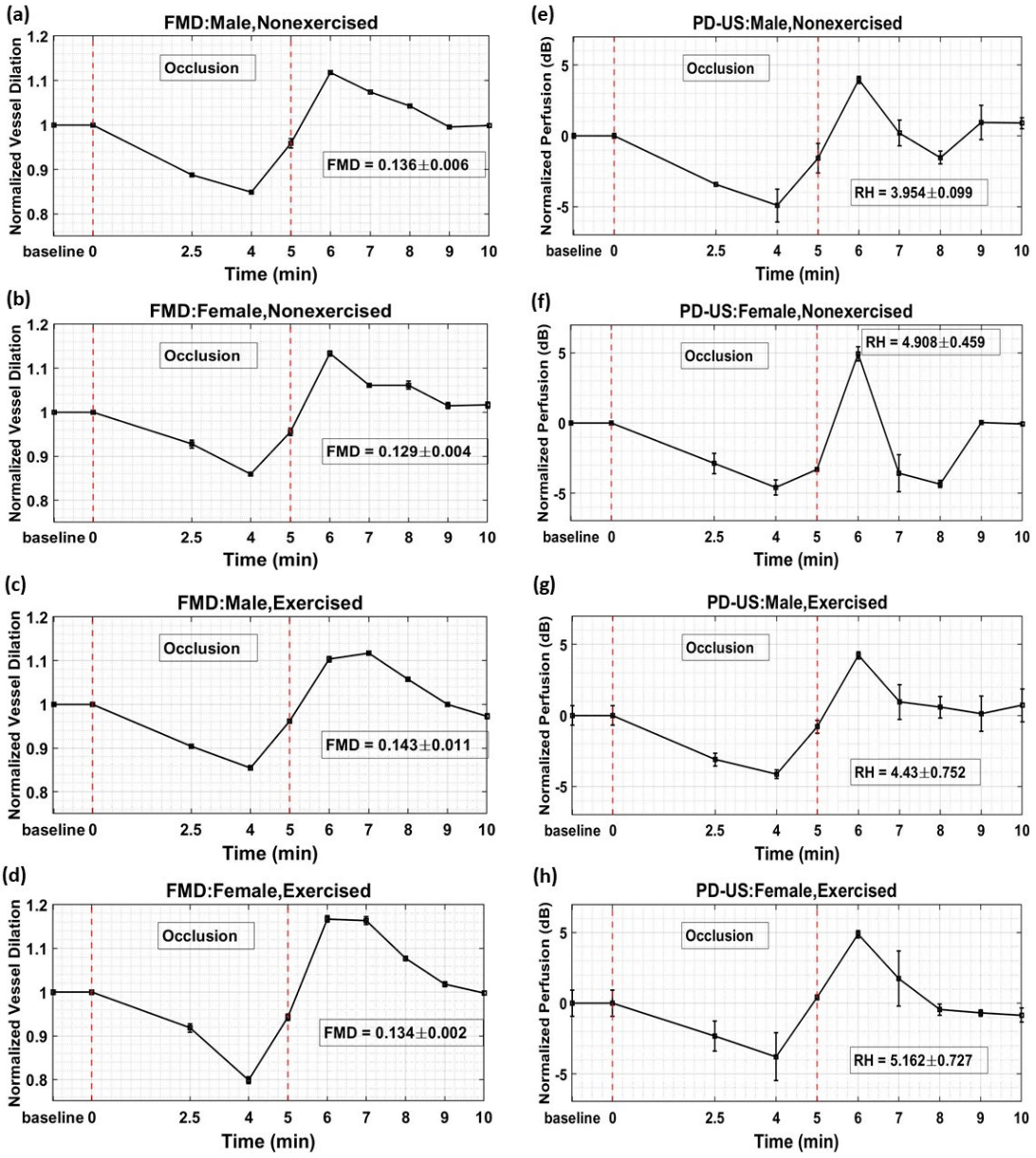

Figure 3.6: Ultrasonic measurements (mean ± 1 SE) of the right internal femoral artery diameter (left column) and muscle perfusion via PD-US measurements (right column) made before, during, and after 5 min of hindlimb ischemia-induced using a pressure cuff. From these data, FMD is estimated via Equation 3.1 for male and female mice with exercise training (N=3) and without exercise training (N=2). Simultaneously, the RH estimates from adjacent muscle regions are computed via Equation 3.2. For all PD-US perfusion estimates, $\rho > 0.9$.

Measurement Method

To assess FMD, we employed scan plane B (SPB in Figure 3.1), which provided a longitudinal view of the femoral artery. The measurements were derived using Equation 3.1, and the values are listed in Figure 3.6 for each mouse group. Due to the elevated heart rates of the mice, exceeding 600 beats per minute, precise synchronization of B-mode frame acquisition proved challenging. However, we mitigated the associated small diameter estimation uncertainty by averaging multiple measurements.

Temporal Variations

Temporal variations in vessel lumen diameter were consistently observed across all groups. During the ischemic phase, the diameters decreased by 14% – 20% below baseline values as hindlimb blood flow slowed. Subsequently, within 2 minutes after releasing the cuff pressure, the artery dilated to peak values that were 12% – 17% greater than the baseline. The overall average FMD value, as indicated in Figure 3.6 a–d, was measured to be 0.136 ± 0.013. Importantly, our analysis revealed no statistically significant differences based on sex or fitness level within the studied mouse groups. Our FMD values are consistent with previous measurements conducted on the same type of mouse but with younger all-male groups. Song et al. [59] reported FMD values of 0.1196 ± 0.0098 for 2-month-old mice, Schuler et al. [60] reported 0.176 ± 0.022 for 3-month-old mice, and Leo et al. [61] reported 0.20 ± 0.038 for mice aged 2 to 24 months. Notably, the authors of the latter study found a SD of 0.12 with a sample size of $N = 10$, which we converted to SE for meaningful comparison. It's essential to note that our study measured vessel lumen in the proximal hindlimb with the cuff positioned distally, near the foot. In contrast, Leo et al. [61] placed the cuff proximally and measured vessels in the distal hindlimb. The influence of different cuff positions on FMD is a topic of discussion in subsequent sections. This comprehensive analysis of FMD estimates provides valuable insights into vascular function and the influence of various factors on FMD values in the context of our mouse model. It contributes to our understanding of vascular health and its assessment in experimental settings. sections.

Perfusion Estimates

In this subsection, we delve into the perfusion estimates obtained through PD-US for muscle perfusion in mice, exploring temporal variations, response to ischemia, and differences between exercise and non-exercise groups.

RH estimates

The PD-US estimates of muscle perfusion are obtained by averaging data over time, space, and the number of animals within each group, as shown in Figure 3.6 e –3.6 h. In each graph, estimates of post-occlusion RH are included, and calculated using Equation 3.2. Specifically, the means ± 1 SE are derived from measurements at six 2-second frame groups of echo data, focusing on a 3 mm^2 muscle region. The sample size (N) varies between 2 or 3 animals depending on the group. Importantly, a comparison of RH estimates between males and females within exercise and non-exercise groups reveals no statistically significant differences at the 5% significance level.

Temporal Variations in Perfusion

The temporal variations in perfusion, as represented by the PD-US curves, closely mirror the changes observed in arterial diameter. During the ischemic period, PD-US estimates indicate that perfusion decreases to

approximately 0.32 to 0.40 of the baseline (equivalent to 4–5 dB) in all groups. Post-ischemic PD-US values indicate hyperemic peaks at 2.5 to 3.2 times the baseline (4–5 dB), occurring approximately one minute after the rapid release of cuff pressure. Notably, Leo et al. [40], utilizing laser Doppler methods, reported a similar peak in perfusion at 2.7 ± 0.75 (SD) times baseline values 65 seconds after cuff pressure release.

Reperfusion and Resistance Tone

During the reperfusion phase and after the hyperemic peak, perfusion steadily declines to baseline levels within three minutes following cuff deflation in the exercised male and female groups. However, for the non-exercise groups, the peak post-ischemic power falls below baseline levels for 2–3 minutes before eventually returning to baseline. This observed perfusion dip suggests a difference in deep-muscle perfusion levels between exercised and non-exercised mice following the hyperemic peak. Notably, in the non-exercise groups, perfusion dips below baseline even as the femoral artery remains dilated during these periods, implying a change in resistive vessel tone. The investigation of these perfusion estimates provides valuable insights into the dynamics of perfusion, the response to ischemia, and potential variations based on exercise levels, offering a comprehensive understanding of vascular function in the study of mice.

3.3.3 Invasive Measurements in Rats

Proceeding, We extend our investigations to healthy male rats, replicating the invasive PD-US measurements reported in Figure 3.4 b and the non-invasive FMD measurements reported in Figure 3.4 a from healthy male mice. The objective of the rat study is to measure simultaneous changes in femoral lumen diameter and downstream muscle perfusion. These measurements were conducted before and after the application of lidocaine to hindlimb muscles. Lidocaine, a known vasodilator with minimal influence on conduit vessel tone, was expected to provide insights into vascular responses in this larger animal model. Rats were chosen for this study due to their larger size, which facilitates the application of lidocaine topically to select tissues. Additionally, the slower heart rate of rats compared to mice allows for cardiac synchronization of data acquisition during vessel-lumen measurements.

Experimental Procedure

Measurements were initially taken without the application of lidocaine, and these baseline measurements are represented by the red-line curves in Figure 3.7. Subsequently, a lidocaine solution (10 mg/mL) was topically applied to the exposed hindlimb muscles, and a waiting period of 10 minutes was observed. During this wait time, muscle perfusion was measured every minute, with no significant changes exceeding ±11% (data not shown). Following the wait period, the entire vessel clamping experiment was repeated, and the resulting PD-US data is displayed as black-line curves in Figure 3.7. To facilitate comparisons of perfusion before and after lidocaine application, each curve was normalized by its average baseline measurement.

Expectations and Results

It was anticipated that there would be minimal changes in the artery diameter measured before and immediately after a short 30-second vessel occlusion, based on the findings of Leo et al. [61]. Leo and colleagues measured the extent of vascular dilation as a function of the ischemic period duration, predicting negligible dilation following a 30-second occlusion. Additionally, it was expected that lidocaine would primarily dilate downstream resistive vessels in muscles during times well beyond any reactive hyperemic period.

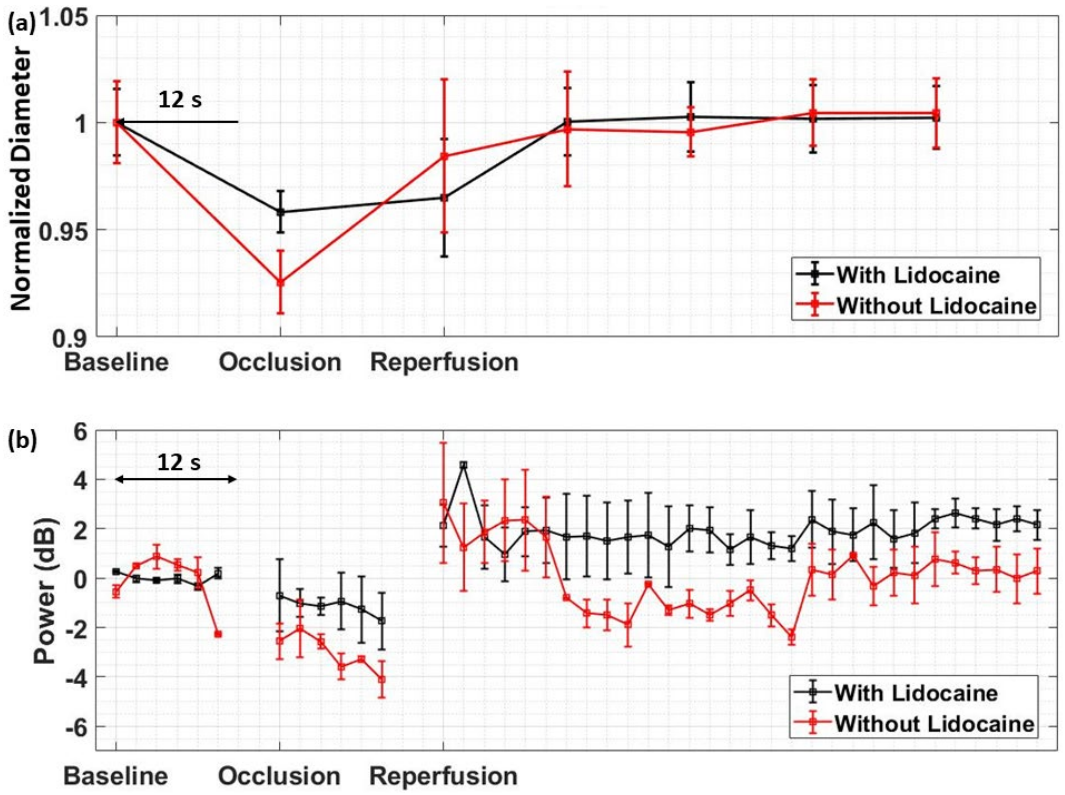

Figure 3.7: An iliac artery clamping experiment is summarized for one male rat with (black) and without (red) lidocaine administered topically to muscles fed by the external femoral artery. (a) Measurements of the fractional change in the femoral artery diameter (mean ± 1 SD). Each point is formed by normalizing the averaging lumen measurements acquired over 12 seconds with the mean baseline measurement. The average baseline and occlusion period values are given along with reperfusion measurements made every 30 seconds after the vessel is released. (b) Simultaneous PD-US measurements (mean ± 1 SD) indicate blood perfusion in downstream muscle. Perfusion is estimated every 2 seconds over 12 seconds intervals before the vessel is clamped (baseline) and during the 30 seconds clamping period. Perfusion is also estimated over 12 seconds intervals every 30 seconds after the vessel is released. The 18 seconds gap following each 12 seconds recording is compressed in time. Heart rate = 450 - 650 bpm, respiratory rate = 87 bpm and body temperature = 37°C.

The changes in the diameter of the right external femoral artery lumen relative to baseline are plotted in Figure 3.7 a, with baseline diameters provided in Table 3.1. Each data point represents an average of measurements collected over 12 seconds of B-mode data. The results of PD-US muscle perfusion are presented in Figure 3.7 b, where each point indicates signal power relative to the average baseline measurement during the 12-second recording. As expected, the topical application of lidocaine directly to hindlimb muscles had limited influence on the tone of the femoral artery supplying the muscle. However, it was evident that lidocaine enhanced muscle perfusion post-occlusion, extending beyond the duration of the hyperemic peak. These findings provide compelling evidence that PD-US measurements are sensitive to changes in muscle perfusion following the dilation of resistive vessels.

3.4 Discussion

3.4.1 Invasive Studies

The comprehensive examination of invasive studies, as depicted in Figures 3.4 and 3.5, provides insights into the congruence and distinctions between PD-US and LSCI in measuring tissue perfusion. These studies allow us to explore the extent to which these two imaging modalities can yield comparable data and under what conditions such comparability can be achieved.

PD-US measurements of muscle perfusion are inherently distinct from LSCI measurements of superficial tissue perfusion in several aspects. PD-US acquires data in a tomographic plane, delving into the depth of the tissue, while LSCI, in contrast, captures data from the proximal tissue surface. This inherent difference in data acquisition modalities introduces challenges in directly comparing the results. One critical finding that emerges from these studies is the remarkable agreement between measurements of relative perfusion obtained using PD-US and LSCI, provided that surface vessels are excluded from spatially averaged LSCI values. Figure 3.5 a beautifully illustrates this convergence when surface vessels are carefully omitted from the analysis. This agreement suggests that both modalities, when used selectively, can reliably reflect regional changes in tissue perfusion. Consequently, when substantial differences between the responses of these two modalities are observed, as documented in previous ischemic hindlimb experiments [40], it bolsters our confidence that such discrepancies genuinely represent distinct regional perfusion patterns.

In the field, it is not uncommon for researchers to apply LSCI specifically to the foot region, denoted as "region 2" in our study 3.5. This is particularly relevant when monitoring changes in surface perfusion, and Figure 3.4 c accentuates this practice by demonstrating that the foot region exhibits the most pronounced deviation from the baseline during ischemic periods. In summary, the invasive studies presented in this section highlight the compatibility and divergence between PD-US and LSCI measurements of tissue perfusion. The agreement found in the measurements, particularly when surface vessels are excluded, underscores the utility of these modalities in revealing regional perfusion changes. This understanding can be instrumental in future research and clinical applications where precise perfusion assessment is critical.

3.4.2 Non-Invasive Studies

In Figure 3.6, we present the outcomes of non-invasive experiments, focusing on vascular responses to a 5-minute ischemic period in both male and female mice. The observations within this section provide insights into the interaction between different biological variables and the overall health status of the subjects.

Vascular Responses

Figure 3.6 illustrates that there were no statistically significant differences in the vascular responses between male and female mice during the 5-minute ischemic period. This finding suggests that the vascular responses were consistent across genders. Temporal variations in femoral artery diameter (Figure 3.6 a - 3.6 d) were similar for all four mouse groups. Furthermore, the changes in the muscle-perfusion time series (Figure 3.6 e - 3.6 h) mirrored the observed variations in artery diameter. These results are indicative of healthy vascular endothelial function and response in these adult mice, with no notable distinctions based on sex.

Comparison of FMD and RH Estimates

Detailed analysis of the data revealed minimal discrepancies among FMD and RH estimates among the four groups, none of which reached statistical significance. The absence of significant differences in these measures is in alignment with previously reported findings, suggesting normal vascular endothelial function in these healthy adult animals. While the majority of our findings pointed to highly consistent vascular responses, there was an exception noted when comparing non-exercised animals with their exercised counterparts. After an initial reperfusion burst, non-exercised animals experienced a period of reduced post-ischemic reperfusion. This phenomenon was not observed in the exercised groups. This observation hints at a potential difference in the hyperemic responses of conduit and resistive vessels between the two sets of animals. Such variations are worthy of further investigation, as they might be influenced by the impact of regular physical activity.

Comparative FMD Measurements

An interesting point of consideration is the comparison of our FMD measurements with those reported by Leo et al. [61]. Our measurements in the proximal hindlimb were found to be only 68% of those reported by Leo and colleagues in the distal hindlimb. This discrepancy can be attributed to the differences in the positioning of the occlusion cuff during experiments. While we placed the cuff near the foot and measured proximally, Leo et al. employed proximal occlusion with distal measurements. A parallel can be drawn to a study involving FMD techniques in humans [62], where it was demonstrated that the choice of occlusion site can significantly influence FMD values. Distal occlusion at the wrist resulted in FMD values only 62% of those obtained with upper bicep occlusion. These findings emphasize that the choice of occlusion site plays a pivotal role in the interpretation of FMD measurements.

Unique Experimental Limitations

It is important to acknowledge that some of the limitations encountered during these experiments are unique to non-invasive approaches. For instance, the duration of tissue sampling through US was limited to 12 seconds, and each recording needed to be offloaded for 18 seconds before the next 12-second time series could be recorded. This temporal constraint resulted in the gaps observed in the time plots of Figures 4b and 7b. Additionally, vessel clamping, while effective for experimental purposes, presented challenges related to tissue deformations and out-of-plane tissue movements during clamping transitions. This led to incomplete clutter filtering for PD-US estimates, a concern that does not apply to clinical assessments where real-time onboard processing is more readily available. The incorporation of fast rigid spatial registration methods in system software is proposed as a valuable addition to addressing this challenge.

In conclusion, the non-invasive studies provide valuable insights into the vascular responses of healthy mice during ischemic challenges, and the findings are pivotal for the next experiment in the context of diabetic animal models. These experiments, along with the invasive studies conducted, contribute to a more comprehensive understanding of perfusion dynamics in different settings.

3.5 Summary

The primary objective of this chapter was to assess the reliability of PD-US measurements without the use of contrast enhancement for monitoring temporal changes in peripheral blood perfusion. Through pre-clinical rodent studies, we developed and validated a combination of spatial registration and clutter filtering techniques

applied to PD-US signals, allowing the consistent tracking of blood perfusion in skeletal muscle. In invasive studies, we compared PD-US measurements in deep muscle with LSCI of superficial tissues before, during, and after short-term arterial clamping. Additionally, non-invasive studies involved the use of a pressure cuff to induce prolonged hindlimb ischemia. These studies included B-mode imaging to measure FMD of the femoral artery and simultaneous PD-US monitoring of downstream muscle perfusion to quantify RH. Biological variables, such as the sex and fitness levels of adult male and female mice and rats, were explored.

Our PD-US methods were validated through comparisons with LSCI measurements. As expected, we observed no significant differences between sexes or fitness levels in FMD or RH estimates. However, exercise conditioning did enhance post-ischemic perfusion, suggesting differences in the hyperemic responses of conduit and resistive vessels. Furthermore, our ability to assess endothelial function and vascular responses across a spectrum of biological variables positions us well for the next phase of our study. Specifically, we aim to apply the insights gained from these experiments to estimate hindlimb perfusion in both healthy and diabetic mice. The literature has highlighted several factors influencing endothelial function in diabetic animal models, and our non-invasive approach using PD-US provides a sensitive tool for monitoring deep-muscle vascular responses in both healthy and diabetic individuals.

Chapter 4

Power-Doppler ultrasonic imaging of peripheral perfusion in diabetic mice

4.1 Study Overview

Our primary objective in this study [63] is to showcase the potential of PD-US imaging in detecting perfusion changes associated with diabetes, particularly in assessing endothelial function. The independence of endothelial responses in conduit and resistance vessels introduces scale-dependent information regarding the risk of atherogenesis advancing towards coronary artery disease [46] [64]. Changes in the function of conduit vessel endothelium provide insights into the risks associated with advancing age and hypertension. On the other hand, changes in the endothelial function of resistive vessels, a feature uniquely described by PD-US [37], indicate risks associated with metabolic imbalances linked to a high body-mass index and diabetes, which are known precursors of PAD [49].

In the course of this research, we delve into diabetic-related changes, specifically focusing on the maximum loss of perfusion following femoral ligation, the time required for full perfusion recovery, and the resistance to blood flow (RH) in resistive vessels. Our study demonstrates that PD-US imaging exhibits high sensitivity to disease-specific changes in diabetic mice, suggesting its potential to revolutionize the monitoring of peripheral perfusion in clinical practice. The findings and insights presented in this thesis contribute significantly to the development of non-invasive, accessible, and cost-effective methods for the early detection and monitoring of PAD, offering the potential to improve patient outcomes and the overall management of this prevalent vascular condition.

4.2 Method

4.2.1 Animal Preparation

In this study, a total of 30 male and 30 female C57BL/6 mice, sourced from Charles River Laboratories in the United States, were carefully selected for our experimental cohort. To ensure rigorous control over variables, these mice were categorized into eight subgroups based on key factors such as health, sex, and fitness levels, as outlined in Figure 4.1. Prior to conducting any experimental procedures, ethical considerations were paramount. All animal research protocols and procedures were conducted in strict adherence to the guidelines

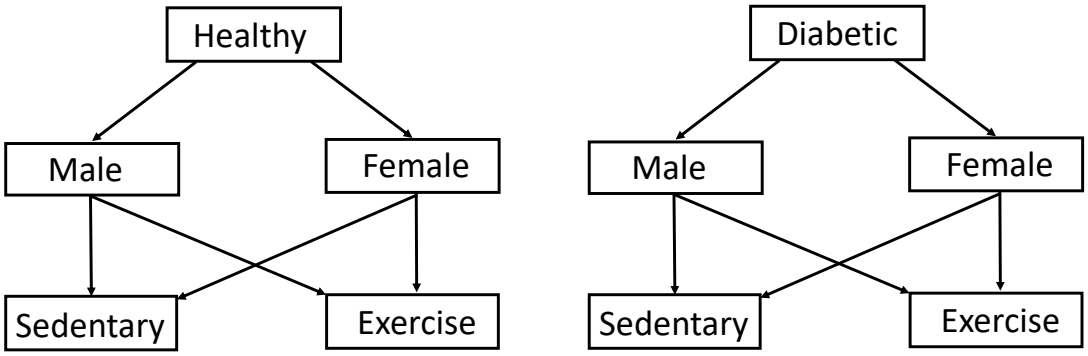

Figure 4.1: Breakdown of the mouse cohorts examined. From Elsevier with permission.

established by the Institutional Animal Care and Use Committee (IACUC) at the University of Illinois at Urbana-Champaign. The IACUC approval ensures the ethical treatment of animals and compliance with relevant regulatory and welfare standards.

Anesthesia and Positioning

Each mouse underwent anesthesia, with isoflurane administered at a concentration of 2-3%. Following successful anesthesia, the mice were placed in the supine position on a heated pad to maintain their body temperature during the entire experimental process. The use of a heating pad is crucial in preventing any temperature-related stress or complications during the procedures. To minimize unintended body movements that could interfere with measurements, each limb was securely fastened using Velcro straps. This restraint ensured the stable positioning of the mice during data acquisition.

Fur Removal and Vessel Exposure

In preparation for the experimental procedures, the fur on the inner surface of both hindlimbs was carefully removed using a depilatory cream. This step was taken to facilitate clear access to the targeted anatomical areas. Following fur removal, a small incision in the skin was made using micro scissors, and gentle dissection was carried out to expose the right femoral artery and vein. The exposed vessels were ligated together using 6-0 silk suture. The choice of ligation site was made judiciously to reduce perfusion by 30-50% while preserving sufficient blood flow patterns in adjacent vessels to circumvent the ligation site. This careful approach aimed to prevent muscle necrosis, ensuring the viability of the limb for further experimentation.

Recovery and Restoration

It is noteworthy that natural recovery processes were leveraged to restore blood flow to the ligated limb. Over the course of two weeks, the limb underwent normal arteriogenic and angiogenic compensatory processes, leading to the natural restoration of perfusion[65] [66] [67].

4.2.2 Data Acquisition Schedule

In addition to acquiring baseline measurements before femoral ligation, Power-Doppler Ultrasonic (PD-US) data were obtained from muscles in the ligated right hindlimb and the control left hindlimb at various time

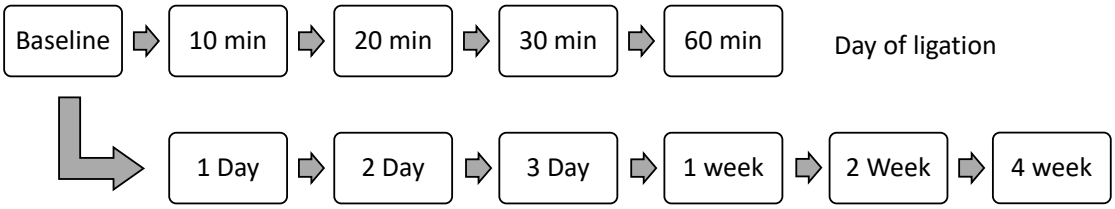

Figure 4.2: PD-US data are acquired from muscles in both mouse hindlimbs according to this measurement schedule. Baseline measurements are recorded before right femoral ligation at t = 0. From Elsevier with permission.

points spanning from 10 minutes to 4 weeks post-ligation, as indicated in the measurement schedule outlined in Figure 2. The meticulous preparation and standardized procedures applied to the animal subjects are crucial for ensuring the accuracy and reliability of our study's results, contributing to a comprehensive understanding of the vascular dynamics in response to our experimental interventions.

4.2.3 Diabetic Mouse Model

In this investigation, we employed an obesity-induced type-2 diabetes mellitus mouse model to investigate the impact of diabetes on peripheral perfusion in the C57BL/6 mouse strain, a widely used model for biomedical research. The diabetic mouse model was implemented following a well-established protocol, which aimed to replicate features of type-2 diabetes that are commonly observed in humans [68] [69].

Model Induction

To induce diabetes, a single low dose of streptozotocin (STZ) was administered intraperitoneally (i.p.) at 20 mg/kg. STZ is a compound known for its ability to damage pancreatic β cells, resulting in a state of reduced insulin production, a hallmark of type-2 diabetes. Subsequently, the mice were transitioned to a high-fat, carbohydrate-free diet (HFD) provided by Research Diets (Catalog #D12492). This diet, with an energy content consisting of 72% lard, 28% protein, and less than 1% carbohydrate, was maintained for a duration of three months. One of the key features of this model is the heterogeneity of the metabolic response among the mice. It was anticipated that only approximately 50% of the mice subjected to this protocol would develop the obese diabetic phenotype [69]. This inherent variation mirrors the clinical heterogeneity seen in human patients with type-2 diabetes.

Diabetic Confirmation

Diabetic induction was validated through an intraperitoneal glucose tolerance assay. In this assay, glucose (1 g/kg) was injected i.p. after a 6-hour fasting period. Blood glucose levels were monitored at specific time points (-30, 0, 30, 60, and 90 minutes after glucose administration) by collecting a 3.5 μL blood sample from a tail vein and measuring it using a glucose meter. A mouse was classified as diabetic when the fasting glucose baseline level (at T-30) exceeded 200 mg/dL, and both the area under the curve (AUC) for the intervals T0-T30 and T30-T90 exhibited statistically significant differences compared to non-diabetic animals [70].

This model is particularly relevant to the study of human diabetic physiology. It mimics key aspects of type-2 diabetes, including obesity-induced insulin resistance and the absence of β cell compensation, ultimately

resulting in impaired glucose tolerance. Furthermore, the model is characterized by being environmentally induced, as opposed to genetic or chemical factors [71]. It is noteworthy that hyperglycemia induced by low-dose STZ is unlikely to induce diabetes in animals fed a standard diet [72]. The adoption of this diabetic mouse model provides a robust platform for investigating the impact of diabetes on peripheral perfusion, given its ability to replicate important features of the disease observed in humans. The heterogeneous response observed in this model adds a layer of complexity and clinical relevance, making it a valuable tool in our pursuit of understanding vascular dynamics in diabetic subjects.

4.2.4 Exercise Regimen

During this exploration, a carefully designed exercise regimen was implemented to assess the impact of physical activity on vascular health in both healthy and diabetic male and female mice, as depicted in Figure 4.1. Physical activity is recognized as a pivotal factor in shaping vascular health, especially in the context of metabolic disorders [73].

Group Stratification

To systematically evaluate the effects of exercise, the mice were categorized into two main groups: sedentary and exercised subgroups. This stratification allowed us to make precise comparisons and analyze the distinct vascular responses resulting from the exercise regimen. Each of these subgroups included both healthy and diabetic mice, providing a comprehensive view of how exercise influences vascular dynamics across different health conditions and sexes. the exercise protocol for the pre-ligation phase was described in detail in the previous chapter 3.2.1.

Post-Ligation phase

Following the pre-ligation phase, the mice continued the 60-minute daily exercise routine throughout the four weeks of post-ligation testing. This allowed us to examine how exercise influenced vascular health during the critical recovery period after femoral ligation. The exercise regimen was meticulously tailored to provide valuable insights into the role of physical activity in vascular health under various health conditions and across different sexes. By systematically analyzing the vascular responses of these subgroups, we aimed to gain a comprehensive understanding of the interplay between exercise, diabetes, and vascular dynamics.

4.2.5 FMD and RH Estimates

In this study, we evaluated endothelial function in the mouse groups by assessing two critical parameters: FMD of the left femoral artery and the RH Index, while simultaneously obtaining PD-US perfusion estimates in the muscles of the left hindlimb. The methodology for these assessments has been detailed in the previous chapter 3.3.2.

FMD is a pivotal indicator of endothelial function, specifically in conduit vessels. To measure FMD, we employed a well-established approach. Following a 5-minute pressure-cuff occlusion, we monitored changes in the diameter of the femoral artery using 24 MHz B-mode US imaging. These measurements were recorded every minute for a total of 5 minutes. Normal FMD values for mice typically fall within the range of 0.13 to 0.14, as established in the prior chapter [37]. Values below this range are indicative of reduced endothelial function in conduit vessels. Simultaneously with FMD measurements, we assessed the RH Index. RH serves as an important indicator of endothelial function in resistance vessels. This assessment was carried out using

the same data acquisition setup. Based on the previous chapter [37], the normal range for the RH Index typically falls between 3.9 and 5.2 dB. Smaller RH values are suggestive of reduced endothelial function in resistance vessels.

These assessments allowed us to gain valuable insights into endothelial function in both conduit and resistance vessels within the mouse groups, providing a comprehensive view of the vascular dynamics and their response to the experimental interventions.

4.2.6 NO Inhibition

In the context of our study, we made an intriguing observation as perfusion in the hindlimb declined following right femoral ligation. Approximately 20 minutes after ligation, we noted the emergence of a sudden, short-lived perfusion peak. This unexpected event prompted us to develop a hypothesis, which centered around the role of endothelium-dependent, flow-mediated NO release in inducing this transient vasodilation. We posited that the surge in NO production was responsible for this vasodilatory response, as the blood flow in the hindlimb adapted to the sudden onset of ischemia. To test this hypothesis and explore the involvement of NO in the observed phenomenon, we conducted a separate experimental study. In this study, we used an additional group of 10 C57BL/6 mice, all 9-month-old sedentary males.

Experimental Design

The 10 mice were divided into two groups, each consisting of five individuals. The first group received an intraperitoneal (i.p.) injection of a non-specific nitric oxide synthase (NOS) inhibitor known as L-NAME (Cayman Chemicals #80210, Ann Arbor, MI). Each mouse in this group received a dose of 3 mg of L-NAME, administered one hour before the right femoral ligation procedure. This group was designated as the "L-NAME group." The second group, serving as a control, consisted of an additional five mice that underwent the right femoral ligation procedure without receiving the L-NAME inhibitor. These mice were also healthy, 9-month-old, sedentary males.

The administration of L-NAME, a NOS inhibitor, allowed us to specifically target the production of NO in these mice. By comparing the response of the L-NAME group to the control group, we sought to gain insights into the role of NO in the sudden perfusion peak observed after femoral ligation. This investigation not only adds depth to our understanding of the underlying mechanisms behind the observed vasodilatory response but also sheds light on the involvement of NO in adjusting blood flow in the hindlimb in response to ischemia. The results from this study will contribute to our broader understanding of the vascular dynamics and regulatory processes in our experimental model.

4.2.7 Data Acquisition and Processing

To assess perfusion in the hindlimb muscles, we employed meticulous data acquisition techniques using a Visualsonics system. A specialized MS 400 probe was used to record pulse-echo signals. While the surgical procedures to prepare the mice were similar to previous descriptions, anesthesia was adjusted to 1.3% isoflurane, ensuring the well-being of the subjects. The processes detailed in the preceding chapter 3.2.4 have been thoroughly elucidated. In the subsequent section, we provide a concise overview of these processes

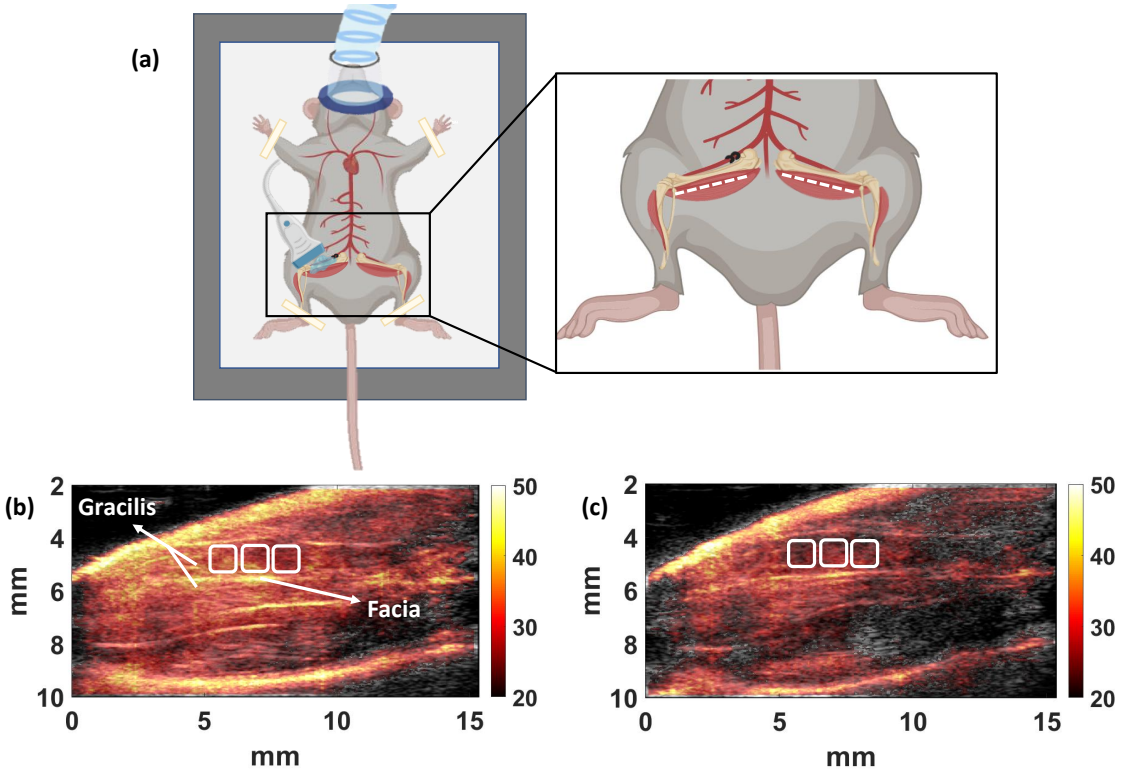

Figure 4.3: (a) Positioning of the 24 MHz linear array (not to scale) on a mouse wearing a nose cone to maintain anesthesia. Inset: the dashed white lines indicate the PD-US scan plane locations on muscles in both legs. (b) PD-US images of pre-ligation and 60-min post-ligation hindlimbs. Three 1 mm2 analysis regions in the gracilis muscle are selected to estimate the spatially averaged perfusion. Illustration in (a) was created with BioRender.com. From Elsevier with permission.

US Imaging

The US imaging was conducted using the Vevo 2100 system, with the scan planes directed at the right (ischemic) and left (control) hindlimb muscles. The precise positioning of the scan planes can be observed in the inset of Figure 4.3 a, indicated by dashed lines. Perfusion images were generated offline from the IQ data.

Probe Alignment

To ensure that the same image plane was consistently located for each measurement, the US probe was initially aligned to capture the long axis of the femur. Following this alignment, the probe was translated medially and perpendicularly to a scan plane until the femur was no longer visible. The probe was then mechanically fixed in this position, eliminating any hand jitter during the measurements.

Region of Interest (ROI)

Within the gracilis muscle, three distinct 1 mm^2 regions were selected for analysis, as illustrated in Figure 4.3 b. The regions of interest for PD-US estimates were centered approximately 4 mm from the probe, at a tissue depth of 2 mm. This positioning ensured that the ultrasonic attenuation losses remained approximately 5 dB for all acquisitions. We opted not to compensate for attenuation, as the signal loss was uniform for all scans.

This approach resulted in an echo SNR of approximately 15 dB, which in turn produced acceptable PD-US estimation uncertainties [24].

Stability of Muscle Region

It's important to note that femoral ligation induces alterations in perfusion distribution within the hindlimb as the body adapts to compensate for the lost blood flow. To minimize estimation variability caused by changing spatial perfusion patterns, we consistently selected the same muscle region at each time point. This approach ensured that the hindlimb vasculature remodeling did not introduce additional variability among mice in our study.

Data Averaging

The PD-US values reported in our analysis were obtained through the aggregation of echo data across space, time, and the number of animals in each cohort. To ensure robust and reliable results, we recorded ninety-six Doppler frames of echo data over a period of 12 seconds at a frame rate of 8 fps. A transmit pulse frequency of 24 MHz was employed. Following the acquisition of each dataset, a minimum of 18 seconds was allocated for downloading the echo data from the scanner to facilitate offline processing. This step was crucial to ensure that additional data could be recorded without interruptions. The process was carefully executed to guarantee the integrity and accuracy of the data collected.

4.2.8 Doppler Frame Partition and Processing

In our study, we thoroughly processed Doppler frames to extract valuable information about muscle perfusion. Each Doppler frame, comprising 17 echo frames, was acquired in CF mode at a frame rate of 1000 fps. We adopted a structured approach to ensure data accuracy and quality.

Frame Selection and Grouping

To begin, we selected the first echo frame from each of the 96 Doppler frames, forming the foundation for our subsequent analysis. These echo frames were then partitioned into six distinct groups, each consisting of 16 echo frames. Each of these groups spanned a 2-second interval of muscle perfusion data, allowing us to meticulously assess the dynamics within this timeframe. This approach provided us with a high Doppler-frequency resolution of 0.5 Hz and a remarkable velocity resolution of 0.016 mm/s [37]. Our bandwidth extended to ± 4 Hz, enabling us to capture a wide range of perfusion dynamics.

Data Processing Steps

The initial stage of PD-US estimation involved converting the IQ signals recorded into RF echo data, following the manufacturer's instructions.

The subsequent step involved spatially registering the 16 echo frames in each 2-second interval to the first echo frame. This registration was performed with precision to minimize the decorrelation of tissue echoes caused by tissue motion occurring between Doppler frames. To achieve this, a rigid spatial registration method was employed, which offered sub-sample RF echo-signal registration accuracy with micron-scale precision as described in the previous chapter 2.2.4. An example of axial and lateral displacements before and after spatial registration for a mouse experiment is illustrated in Figure 4.4 b. It's worth noting that the

tissue movement in this example was in sync with respiration, where the scan plane periodically translated 0.010 mm in a direction lateral to the beam axis and along the muscle fibers while simultaneously trending downward along the beam axis and to the left toward the foot.

The final data processing step involved passing the spatially registered data through PCA clutter filter. Our findings revealed that when the tissue remained motionless over the 2-second interval, removing the first singular value in the PCA filter output effectively minimized tissue clutter power [24] [37]. Consequently, blood cell motion emerged as the primary source of decorrelation for echo signals that had undergone PCA filtering. The post-filtered echo-signal power was computed for each hindlimb and normalized by its pre-ligation baseline value. Mean values and SEs were computed for the sample size, and the results were converted to decibels (dB). The resulting data was presented in Figure 4.6, offering a comprehensive visualization of the perfusion dynamics in the hindlimb muscles. Our systematic data partition and processing strategy enabled us to obtain accurate and meaningful insights into muscle perfusion dynamics, ensuring the integrity and quality of our results.

4.2.9 Spatial Registration and Clutter Filtering

Our analysis encompassed data processed both with and without spatial registration applied before PCA clutter filtering. The effectiveness of these steps depended on specific conditions, especially regarding tissue motion within the scan plane. In situations where tissues exhibited translations exceeding 10-20 µm in the scan plane, we observed that spatial registration significantly improved the separation of signal subspaces. This separation was particularly vital for distinguishing between strong, slow-moving tissue echoes and weak, slow-moving blood-cell echoes. By enhancing the efficacy of clutter filtering, spatial registration played a crucial role in ensuring that PD-US estimates accurately represented blood perfusion dynamics without the need for contrast enhancement.

Significance of PD-US Estimates

It's important to note that while PD-US estimates do not provide quantitative measurements in units of flow per mass of tissue, they offer valuable signal-power estimates. These signal-power estimates were found to consistently reflect perfusion changes occurring over the course of our four-week study period [37]. The ability to reproducibly capture perfusion changes in this manner proved to be essential in our research, allowing us to monitor and analyze the vascular dynamics and their response to experimental interventions with a high degree of accuracy and reliability. The inclusion of spatial registration and PCA clutter filtering contributed to the precision and consistency of our PD-US estimates, offering an indispensable tool for the comprehensive evaluation of blood perfusion in the hindlimb muscles and their response to various physiological and pathological conditions.

4.2.10 Parameters Characterizing the Ischemic Response

The results section in this chapter of the thesis displays a comprehensive time series of hindlimb muscle perfusion changes observed over the 28-day post-ligation measurement schedule depicted in Figure 4.2. Within this section, we delve into the description of three critical parameters derived from these results. These parameters have been thoughtfully selected to characterize the average response of the hindlimb vasculature following right femoral ligation in both healthy and diabetic animal models.

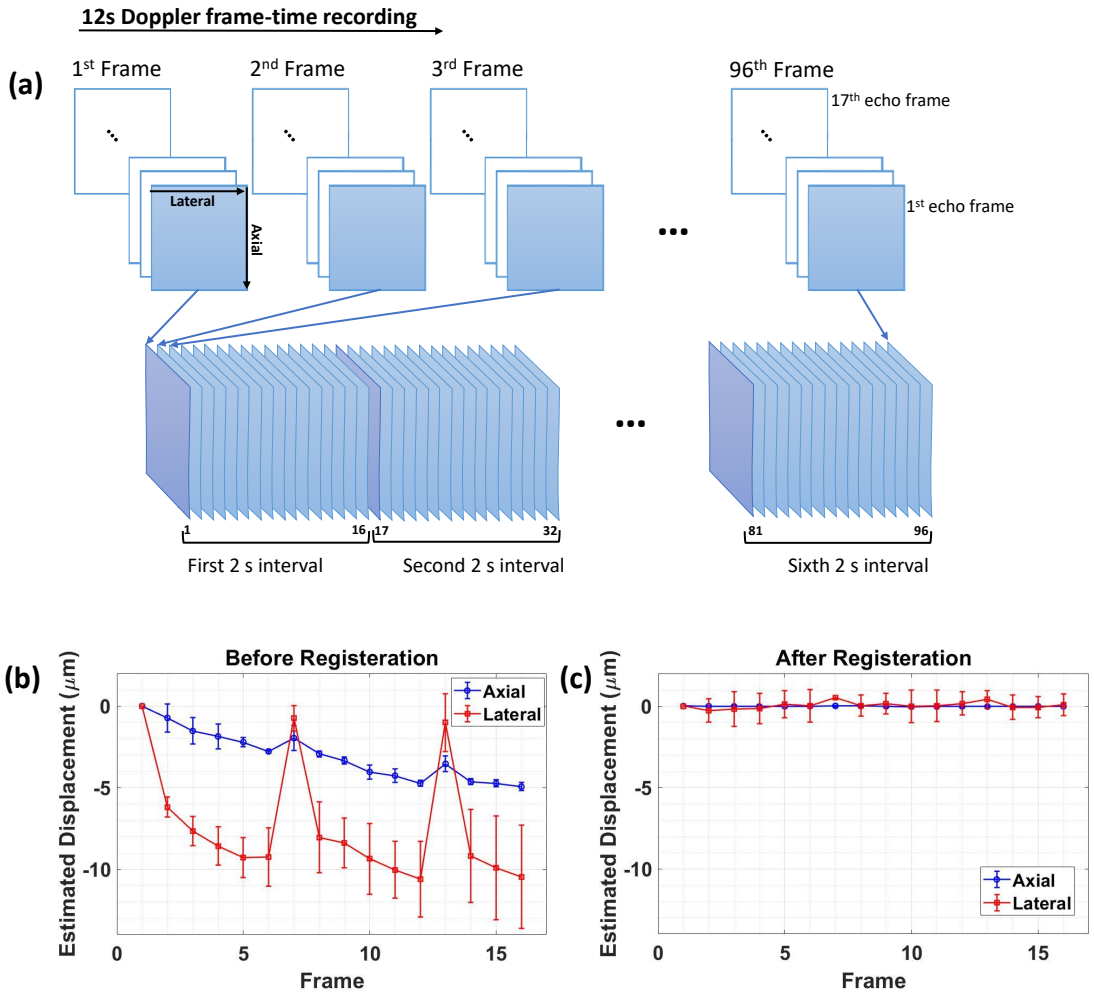

Figure 4.4: (a) Twelve seconds of echo data are recorded in 96 Doppler frames, each consisting of 17 color-mode echo frames. We select the first echo frame in each Doppler frame to assemble 2-s time intervals composed of 16 echo frames at 8 fps for each PD-US estimate. A 12-s recording yields PD-US estimates at six-time points for one mouse; averaging values over N mice yields points plotted in Figure 4.6. An example of relatively large echo displacements measured before (b) and after (c) applying rigid registration to the 16 frames in one 2 s interval is shown. Axial (blue) and lateral (red) movements are plotted as a function of time, where there are 0.125 s between frames.From Elsevier with permission.

Group	Date of Experiment	Age (months)	Ligation type	Sex	Avg. Weight (g)	N'	N
Healthy, Sedentary (HS)	8.25.2020	10	FA	F	NA	5	F = 5
				M	NA	4	M = 8
	6.21.2023	9	FA&V	M	34.1	9	
Diabetic, Sedentary (DS)	10.5.2020	12	FA&V	F	56.82	4	F = 9
				M	63.26	2	
	11.5.2021	25	FA&V	F	54.6	5	M = 6
				M	55.86	4	
Diabetic, Exercise (DE)	7.2.2021	7	FA&V	F	44.08	4	F = 9
				M	46.64	5	
	11.19.2021	11	FA&V	F	48.68	5	M = 7
				M	53.52	2	
Healthy, Exercise (HE)	2.18.2022	14	FA&V	F	32.76	5	F = 5
				M	45.78	5	M = 5

Table 4.1: Summary of mouse-group information. The sources of variability in this study are represented as columns. Values in columns listed as Date of Experiment, Age, Avg. Weight are baseline values at $t = 0$. N' is the number of mice that survived the 4-week trial out of 5 (in one case 10). N indicates mouse numbers for Males and Females after combining data from different experiments within one Group. FA = femoral artery, FA&V = femoral artery and vein. From Elsevier with permission.

Perfusion Spike at 20 Minutes ($P_{\max}$)

At the 20-minute mark following ligation, a notable and consistent perfusion spike is observed in all animals. This spike is denoted as $P_{\max}$, and it represents the maximum increase in perfusion relative to baseline values during the study. To estimate $P_{\max}$, we applied a second-order polynomial curve-fit to the PD-US measurements taken prior to ligation and at time points of 10, 30, and 60 minutes post-ligation. The value of $P_{\max}$ is determined by the difference (in decibels, dB) between the measured PD-US values and the corresponding curve-fit values, as exemplified in Figure 4.5 a. The error bar associated with $P_{\max}$ estimates is calculated based on the SD of PD-US measurements taken at the 20-minute time point.

Recovery Time (T)

An essential parameter in characterizing the ischemic response is the duration it takes for perfusion to recover and return to the baseline level. This parameter is denoted as T. Perfusion in the ischemic hindlimb experiences a progressive decline during the initial 24 to 48 hours post-ligation. However, at the 20-minute time point, there is a transient doubling of perfusion. To estimate the recovery time T, we applied a second-order polynomial curve-fit to the PD-US measurements collected at time points 1, 2, 3, 7, and 14 days post-ligation, as demonstrated in Figure 4.5 b. Since PD-US values are measured relative to the average baseline value, the recovery time T is determined as the point at which the curve-fit line crosses the 0-dB perfusion axis.

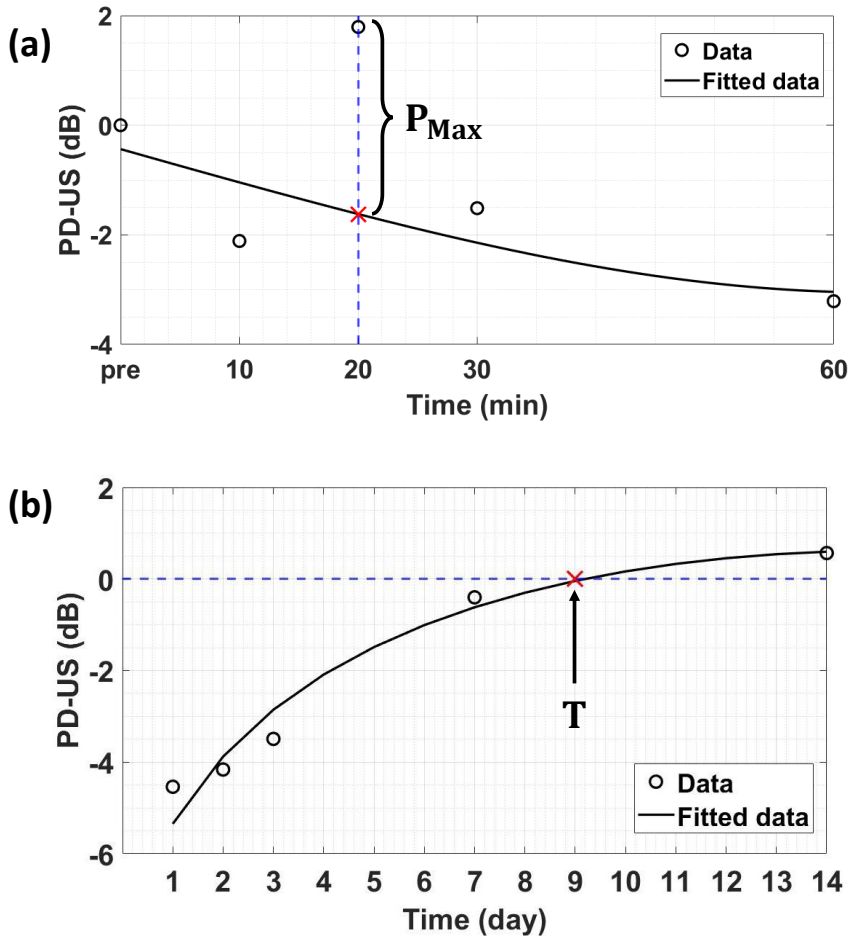

Figure 4.5: (a) Points are perfusion measurements made before (pre) and at four times after right femoral ligation. The solid line is a polynomial fit to these four points. $P_{\max}$ is the difference (in dB) between measured and fit values at 20 min. The 3.5 dB shift indicates a two-fold increase in perfusion-related signal power at 20 min relative to the trend between 10-60 min. (b) Example of a recovery time measurement T from the polynomial fit of perfusion data, where $1 \leq t \leq 14$ days. In this example T = 9 days. The points in both plots are from the data in Figure 4.6. From Elsevier with permission.

Minimum Perfusion Index ($P_{\min}$)

The third parameter, $P_{\min}$, characterizes the minimum recorded PD-US value during the 28-day experiment. It serves as an essential indicator of the lowest perfusion level reached in the hindlimb muscle.

These parameters collectively offer an in-depth understanding of the vascular response in the hindlimb following right femoral ligation, shedding light on the dynamic changes in perfusion and their relationship to health and diabetic conditions. The rigorous methodology and precise analysis applied to obtain these parameters ensure the reliability and robustness of the findings presented in this study.

4.2.11 Statistical Analyses

This section uncovers the statistical aspects of our study, where we explore the key variables influencing our measurements, outline our analytical approach, and address the challenges posed by changing sample sizes in

our data analysis.

Variables and Data Handling

First and foremost, it's vital to elucidate the key experimental variables that underpin our measurement results, as illustrated in Table 4.1. Notably, this table provides an essential reference for the various factors and conditions that could impact our observations. Furthermore, we must consider the temporal dynamics of our sample sizes (denoted as 'n') over the course of the study, a detail clearly depicted in Figure 4.6. Our data analysis was rigorously conducted using MATLAB, a powerful tool for statistical computation and visualization.

PD-US Measurements

Each measurement in our study was derived from PD-US data, which plays a pivotal role in characterizing perfusion within the hindlimb muscle. To ensure the reliability and consistency of our measurements, we employed a meticulous approach. Each PD-US measurement represents the mean echo-signal power observed during a 12-second data acquisition, which is an average of six sequential 2-second estimates. These measurements are critical in assessing perfusion changes over time. The time points plotted in Figure 4.6 represent the culmination of our efforts to provide a comprehensive overview of PD-US measurements. To ensure robust results, these time points are characterized by further averaging PD-US measurements, a process that hinges on 'sample size' (n). The 'sample size' denotes the number of mice in each group under study and is thoughtfully provided beneath the corresponding plots. To assess the reliability of our data, we have also presented representative error bars, providing a visualization of the variability in our measurements, typically denoted as ± 1 SE.

Addressing Sample Size Variability

A noteworthy challenge we encountered in our study pertains to sample size fluctuations, particularly within certain diabetic groups over the four-week experimental period. To address this, we executed a secondary study involving a subset of mice from the original cohort. These additional mice underwent the same experimental procedures but were studied several months later, as detailed in Table 4.1. This approach was necessary to mitigate the influence of falling sample sizes on the statistical power of our analysis. By incorporating data from the second study, we were able to restore sample sizes, enhancing the robustness of our statistical tests. Specifically, these additional data points were included in our analysis, ensuring that the sample sizes were sufficiently representative for subsequent statistical testing.

Non-parametric Analysis of Covariance (ANCOVA)

The analysis of covariance (ANCOVA) is a powerful statistical technique used to investigate the impact of one or more continuous covariates on the relationship between an independent variable (IDV) and a dependent variable (DV). ANCOVA is a valuable tool when the covariate(s) exhibit a significant association with the DV, and its inclusion as a control variable is necessary to elucidate the true effect of the IDV. However, the assumptions of ANCOVA, including normality and homogeneity of regression slopes, may not always be met in real-world data. Non-parametric methods offer a robust alternative when these assumptions are violated. Non-parametric ANCOVA, also known as Kruskal-Wallis ANCOVA, extends the traditional Kruskal-Wallis

test to accommodate covariates. In this section, we delve into the principles, procedures, and applications of non-parametric ANCOVA.

Principles of Non-parametric ANCOVA

Non-parametric ANCOVA is based on the following principles:

1. **Rank-Based Analysis**: Like other non-parametric tests, it relies on rank-based data rather than the actual values, making it distribution-free.
2. **Group Comparison**: It compares the ranks of the DV across different levels of the IDV while controlling for the covariate.
3. **Medians as Summary Statistics**: Instead of means, non-parametric ANCOVA utilizes medians to summarize data within groups.

Procedure

The procedure for non-parametric ANCOVA is as follows:

1. **Ranking Data**: Rank all data points within the DV while preserving the grouping structure of the IDV and the covariate.
2. **Calculate Group Medians**: Calculate the median for each group within the IDV for the ranked data.
3. **Test for Group Differences**: Use the Kruskal-Wallis test to assess if there are significant differences in the group medians.
4. **Covariate Adjustment**: After assessing group differences, use the covariate to control for its influence on the DV. This step is crucial for isolating the effects of the IDV.
5. **Report Results**: Report the results, including p-values, effect sizes, and confidence intervals.

To account for the potential influence of mouse weight and age on perfusion measurements [61], we implemented a non-parametric ANCOVA for our two datasets. This sophisticated statistical technique was employed to determine whether the mean PD-US estimates for the two groups were statistically equivalent. Importantly, ANCOVA allowed us to control for continuous covariates, namely, mouse age and weight.

After meticulous analysis, we found that we could accept the null hypothesis, indicating that the mean PD-US estimates for these two groups were statistically equivalent at the significance level of $p = 0.05$. Consequently, we made the decision to merge these two groups, thereby increasing the sample sizes available for our subsequent statistical analyses, as elucidated in the right-most column of Table 4.1. In the following sections, we will explore the impact of our data processing methodologies and the significance of various biological variables in our study. Our comprehensive statistical analysis aims to unravel the complex dynamics of perfusion in response to different conditions and treatments.

The Box-Cox Transformation

The Box-Cox transformation is a powerful statistical technique used to stabilize variance, normalize data, and make it more closely approximate a normal distribution. Named after statisticians George E. P. Box and Sir David R. Cox, this transformation is particularly valuable when dealing with data that violates the assumptions of normality and homoscedasticity in various statistical analyses. In this section, we explore the principles, procedures, and applications of the Box-Cox transformation [74].

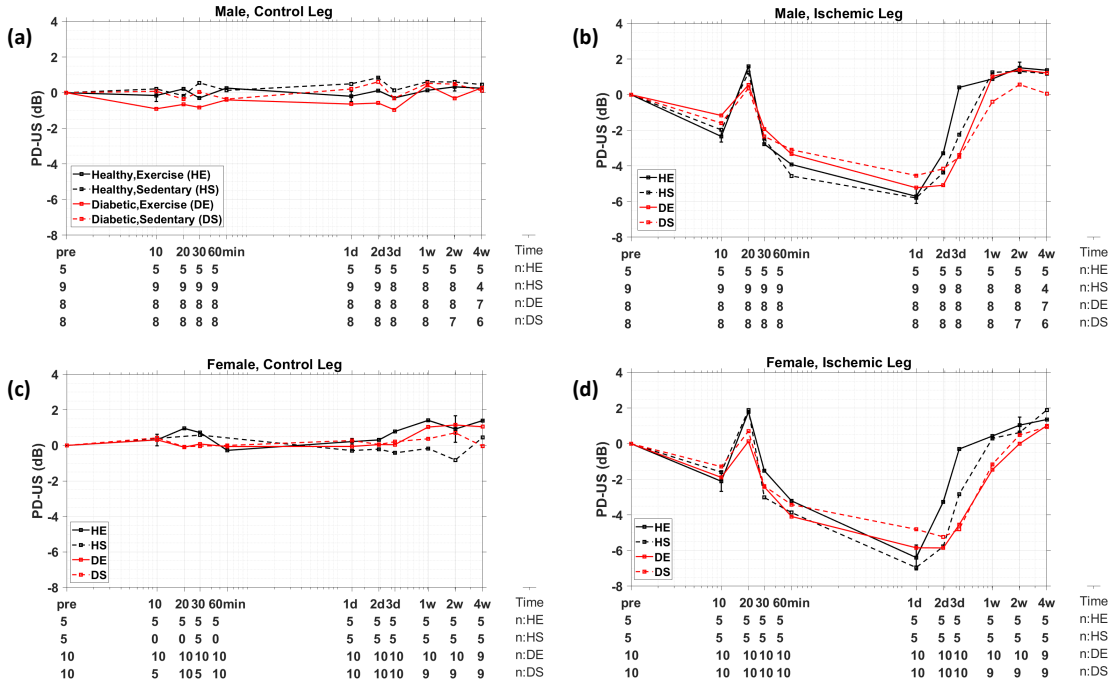

Figure 4.6: PD-US measurements for male (a,b) and female (c,d) mice as a function of time are plotted on log-log scales. Measurements are made on the non-ligated (control) left leg (a,c) and the ligated (ischemic) right leg (b,d). Black lines indicate perfusion changes relative to the pre-ligation baseline in healthy (non-diabetic) mice while red lines indicate that for diabetic mice. Solid lines indicate results for exercised mice and dashed lines for sedentary mice; e.g., DE labels the curve for the diabetic exercised group while HS labels the healthy sedentary group. The time axis extends from pre-ligation baseline measurements (pre) through four weeks post-ligation (4w) as indicated by the schedule in Figure 4.2. Below the time axis are sample sizes (n) over the 4-wk experiment for the four mouse groups. Animal numbers vary because of attrition and unavailable data. Error bars at 10 min, 1 d and 2 w for the HE mouse group indicate ±1 SE.

Principles of the Box-Cox Transformation

The Box-Cox transformation is based on the following principles:

1. **Normalization of Data**: It aims to make the data conform more closely to a normal distribution by applying a power transformation.

2. **Stabilization of Variance**: The transformation can stabilize the variance, making it approximately constant across different levels of the IDV.

3. **Parameter λ**: The transformation involves a parameter λ, which determines the type of transformation applied. The choice of λ depends on the characteristics of the data.

Procedure

The procedure for applying the Box-Cox transformation is as follows:

1. **Identify the Appropriate λ**: Determine the optimal value of λ that makes the data as close to normal as possible. This can be done through graphical methods or statistical tests.

2. **Transform the Data**: Apply the Box-Cox transformation formula to each data point in your dataset:

$$Y(\lambda) = \begin{cases} \frac{X^\lambda - 1}{\lambda} & \text{if } \lambda \neq 0 \\ \ln(X) & \text{if } \lambda = 0 \end{cases} \tag{4.1}$$

3. **Analyze the Transformed Data**: Perform your statistical analysis on the transformed data. This may include regression, analysis of variance, or any other relevant statistical techniques.

4. **Back-Transform (if needed)**: If you performed any analyses on the transformed data, you may need to back-transform the results to their original scale to make meaningful interpretations.

The Wilcoxon Rank Sum Test

The Wilcoxon Rank Sum Test, also known as the Mann-Whitney U test, is a non-parametric statistical test used to determine if there is a significant difference between two independent groups. It is a valuable alternative to the t-test when the data do not meet the assumptions of normality and equal variances. In this section, we explore the principles, procedures, and applications of the Wilcoxon Rank Sum Test.

Principles of the Wilcoxon Rank Sum Test

The Wilcoxon Rank Sum Test is based on the following principles:

1. **Ranking Data**: It involves ranking all the data points from both groups together, regardless of their group membership.

2. **Comparison of Ranks**: The test compares the sum of ranks of one group to the sum of ranks of the other group. The test statistic, U, is calculated based on this comparison.

3. **Null Hypothesis**: The null hypothesis (H_0) posits that there is no significant difference between the two groups, while the alternative hypothesis (H_1) suggests that there is a difference.

Procedure

The procedure for conducting the Wilcoxon Rank Sum Test is as follows:

1. **Combine and Rank Data**: Combine the data from both groups and rank them. Assign lower ranks to smaller values and higher ranks to larger values.

2. **Calculate Test Statistic U**: Compute the test statistic U using the formula:

$$U = R_1 - \frac{n_1 \cdot (n_1 + 1)}{2} \tag{4.2}$$

   where R_1 is the sum of ranks for group 1, n_1 is the sample size of group 1.

3. **Compare to Critical Value**: Compare the calculated U statistic to a critical value from the Wilcoxon Rank Sum Test table or use a statistical software package to determine if the result is significant at a chosen alpha level.

4. **Report Results**: Report the test statistic, the critical value, and whether the null hypothesis is rejected or not.

we examine the necessity of applying spatial registration to the perfusion profiles. The analysis was conducted by processing the data presented in Figure 4.6 in two distinct ways, with a singular exception: in one set of profiles, spatial registration was applied before performing PCA clutter filtering, while in the other set, the filtering was applied directly to the unregistered echo frames. The primary objective of this investigation is to determine whether tissue motion during the acquisition of echo frames has a significant impact on the perfusion profiles.

To facilitate a more robust analysis, a Box-Cox transformation was applied to the mean PD-US measurements for all data points within a given perfusion profile.

Subsequently, both parametric and non-parametric statistical tests were employed to evaluate differences between the perfusion profiles obtained with and without the application of spatial registration. The following tests were conducted:

1. **Parametric Two-Sided t-Test:** This test was used to assess the mean differences between the two sets of perfusion profiles.

2. **Non-Parametric Kruskal-Wallis Test:** The Kruskal-Wallis test was employed to determine whether there are significant differences between the ranked data distributions of the profiles.

3. **Wilcoxon Rank Sum Test:** The Wilcoxon Rank Sum Test was used to evaluate differences in median values between the two sets of profiles.

The significance level for all three tests was set at $p = 0.05$.

Analysis Results

The results of our statistical analyses revealed that, for all three tests, we were unable to reject the null hypothesis at the $p = 0.05$ significance level. Therefore, when considering the entire perfusion profile in the analysis, spatial registration before PCA clutter filtering did not significantly modify the PD-US-based perfusion profiles. These findings suggest that the impact of tissue motion during the acquisition of echo frames may be considered negligible in our specific experimental context.

Additionally, we conducted an assessment of mean differences between registered and unregistered data at individual time points using the Wilcoxon Rank Sum Test without applying the Box-Cox transformation. Remarkably, only five out of 88 point-wise comparisons indicated that spatial registration before clutter filtering resulted in significantly different mean values compared to unregistered data. Notably, these outliers were often observed near the perfusion profile minima, primarily around days 1 and 2. As a result, we opted to employ spatially registered PD-US profiles for the comparison of ischemic parameters, as described in Section 4.2.10 and presented in Figures 4.9 - 4.11, as only a portion of the perfusion profile contributed to those parameter estimates.

Analysis Scope

In our analysis, we specifically focused on testing the null hypothesis between two groups that differed in terms of a single biological variable. For instance, we tested for differences between healthy and diabetic mice within the sedentary female groups. However, we did not conduct tests for differences between sedentary diabetic males and exercised healthy females. These findings provide valuable insights into the impact of spatial registration on the analysis of perfusion profiles and underscore the importance of carefully considering the context and goals of the analysis when making decisions regarding spatial registration.

4.3 Results

4.3.1 Temporal Perfusion Profiles

This section presents a comprehensive analysis of temporal perfusion profiles, with a focus on Figure 4.6, which summarizes PD-US measurements describing muscle perfusion over the course of a four-week study relative to pre-ligation baseline values (pre). The abscissa of the figure marks the time elapsed after right femoral ligation, a pivotal event in the study. It is important to note that spatial registration was not applied prior to PCA clutter filtering during the generation of these data.

The measurements presented in Figure 4.6 pertain to both male and female mice, with the data divided into four distinct panels:

1. Panels (a) and (b) depict measurements for male mice.
2. Panels (c) and (d) depict measurements for female mice.

Within each panel, comparisons are made between measurements on the intact left hindlimb and measurements taken on the ischemic right hindlimb following femoral ligation. This division allows for the assessment of perfusion changes in response to the ligation procedure.

Further subdivision is provided based on the four experimental groups:

1. Healthy Exercised (HE)
2. Healthy Sedentary (HS)
3. Diabetic Exercised (DE)
4. Diabetic Sedentary (DS)

Each of these groups is represented by a distinct curve in the respective panels of Figure 4.6, facilitating a comparative analysis of how muscle perfusion evolves over time within each group. Additionally, to provide context for the analysis, the sample sizes for each group are listed below the time axes. It's worth noting that these sample sizes can vary throughout the study due to factors such as the progression of the experimental protocol, variations in data collection, and potential attrition of subjects. Understanding these variations in sample sizes is crucial for interpreting the results and assessing the robustness of the findings.

In summary, Figure 4.6 and the associated data present a rich source of information for studying temporal changes in muscle perfusion in response to femoral ligation across different gender and experimental groups. The absence of spatial registration before PCA clutter filtering underscores the need to carefully consider the potential impact of spatial factors in the subsequent analysis. The following sections will delve deeper into the specific findings and implications of this data in the context of the research objectives and hypotheses.

4.3.2 Spatial Registration and the PCA Clutter Filter Threshold

Herein, we will address the critical aspects of spatial registration and the determination of the PCA clutter filter threshold. Our examination builds upon the findings akin to those depicted in Figure 4.6, where echo frames underwent spatial registration before any clutter filtering. The pivotal observation is that spatial registration of echo frames, when performed prior to PCA clutter filtering, did not yield significantly different perfusion profiles. This intriguing result underscores the effectiveness of a pragmatic approach in

this study—rigidly fixing the position of the US probe and gently binding the hindlimbs with Velcro straps proved highly efficient in mitigating clutter, or tissue, motion. The implications of this are profound, as it suggests that sophisticated registration techniques may not always be imperative in achieving high-quality data.

This finding stands in contrast to a previously conducted invasive vascular study [37], where in-plane tissue motion greater than 0.01 mm was frequently observed and was found to exert a substantial influence on the PD-US signal unless spatial registration of the echo frames was diligently performed. This contrast highlights the context-specific nature of the spatial registration requirement and underscores the importance of tailoring methodologies to the specific characteristics of the study.

Figures 4.7 and 4.8 provide visual representations to shed light on why spatial registration had minimal influence on PD-US estimates in this study. In Figure 4.7 a, a representative Doppler spectrum is presented at various stages of processing. Two notable spectra, the "original" and "registered," are symmetric about zero frequency, a characteristic of diffuse blood-cell-scatterer motion. Peaks in the original spectrum at ± 2.5 Hz, associated with respiration, are significantly attenuated after spatial registration. However, it's noteworthy that the PCA "filtered" and "registered & filtered" spectra exhibit remarkable similarity, regardless of whether the echo frames were initially spatially registered. In both cases, the PCA filter threshold is set to allow the passage of all singular values except the first. It's these filtered Doppler spectra that serve as the basis for PD-US estimates, as their area under the spectrum is proportional to these estimates.

Figure 4.7 b complements these findings by illustrating the singular-value spectra, which are analogous to the Fourier spectra from Figure 4.7 a. The "original" singular spectrum is derived before spatial registration is applied, while the "registered" spectrum is generated post-registration. The most notable impact of registration on PD-US estimates is the enhancement of separation between the first two singular values. This separation is pivotal, as it informs the selection of the PCA filter threshold. Notably, this threshold is crucial, as it effectively delineates the boundary between the clutter-echo and blood-echo subspaces. Our analysis demonstrates that spatial registration plays a pivotal role in increasing the disparity between the first two singular values, effectively reducing the overlap between the clutter and blood subspaces. This finding highlights the key contribution of spatial registration to the separation of these crucial parameters.

However, it is noteworthy that, regardless of whether spatial registration is employed, the same filter threshold, as indicated by the dashed lines in Figure 4.8, consistently distinguishes the first and second singular values at every point in time. This suggests that coherent tissue motion, measuring less than 0.01 mm, does not alter the PCA filter threshold between the clutter and blood subspaces. In essence, the filter threshold remains robust under these conditions. Only with greater tissue motion does a single threshold no longer suffice to separate adjacent singular values, necessitating the preliminary spatial registration of echo signals. An additional indicator of minimal tissue motion between frames is the correlation coefficient among the pre-filtered echo frames. It remained consistently above 0.8 for unregistered frames and above 0.9 for registered frames, corroborating the assertion that little tissue motion occurred between frames [24]. This insight is essential for understanding the reliability of the data and the validity of the subsequent analysis.

Figure 4.7 complements this perspective by revealing a substantial difference in the filtered power-spectral density at zero frequency with and without spatial registration. However, this difference, which remains relatively consistent across all measurement times during the four-week study, is effectively mitigated by normalizing the PD-US estimates with respect to the pre-ligation baseline value. Normalization not only addresses variations attributable to the registration process but also enhances the comparability of data points across different measurement times.

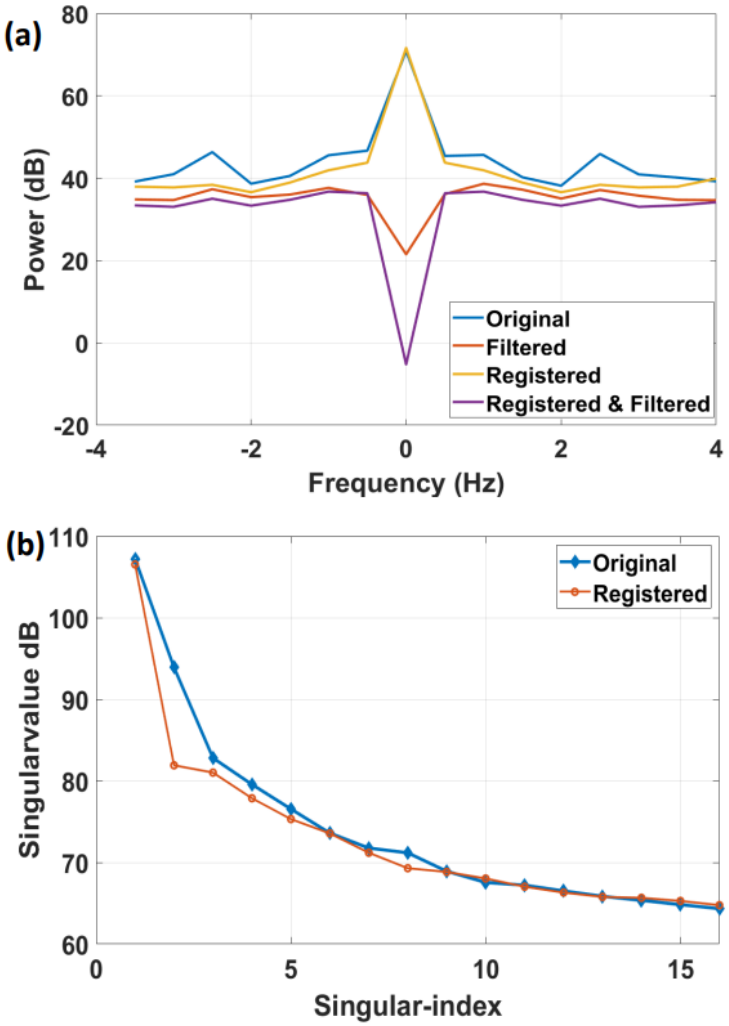

Figure 4.7: (a) Doppler spectra are displayed at different levels of processing. "Original" indicate the power spectral density for echo data as it was recorded. "Registered" labels the spectrum obtained after spatially registering the 16 echo frames in a 2 s acquisition. "Filtered" and "Registered & Filtered" are spectra obtained after applying a PCA clutter filter without and with spatial registration, respectively. (b) Singular spectra are shown from SVD processing of the same data shown in (a) with and without spatial registration. From Elsevier with permission.

The subsequent section will delve into the sensitivity of each perfusion profile to diabetic changes, exploring the influence of sex and fitness level. This analysis represents a pivotal step in understanding the broader implications of the study's findings and their relevance to the overarching research objectives.

4.3.3 Perfusion Profiles for Healthy and Diabetic Hindlimb Muscles

This section focuses on the detailed examination of perfusion profiles for hindlimb muscles in the context of health and diabetes. The discussion begins with the depiction of the perfusion profiles for the ligated right hindlimb (Figures 4.6 b and 4.6 d). Initially, these profiles exhibit a notable decrease in perfusion. However, at approximately 20 minutes post-ligation, a sudden 2-3 dB burst of perfusion is observed across all mouse groups. Subsequently, perfusion continues to decline between 30 minutes and 1-2 days, reaching a minimum value of -5 dB to -7 dB, which corresponds to approximately 20-32% of the baseline perfusion level. It's essential to note that the rate of this decline is correlated with the properties of the specific mouse groups under examination.

Figures 4.6 a and 4.6 c provide a crucial point of comparison, illustrating the muscle perfusion profiles for the left hindlimb, which serves as a control measurement. These figures indicate that irrespective of the mouse group, no significant changes in muscle perfusion are observed for the left hindlimb. The perfusion levels remain essentially constant within ± 1 dB of the baseline values. This consistency underscores the fact that the right femoral ligation, which induces changes in the blood flow of the right hindlimb, does not generate systemic effects that manifest as alterations in the perfusion of the left peripheral muscles.

Furthermore, it's worth noting that no significant differences in baseline perfusion measurements were identified among the eight groups under investigation, although this information is not presented here. The exception to this uniformity was observed in baseline PD-US estimates for females, which consistently registered 2-3 dB higher than their male counterparts. This sex-related difference in baseline PD-US estimates may hold implications for the interpretation of subsequent results and should be taken into consideration.

In summary, the analysis of perfusion profiles for healthy and diabetic hindlimb muscles provides valuable insights into the temporal dynamics of perfusion changes following right femoral ligation. The distinctive responses observed in Figures 4.6 b and 4.6 d, as well as the consistency of the control measurements in 4.6 a and 4.6 c, reveal the nuanced interplay between local and systemic factors in the context of perfusion dynamics.

4.3.4 Minimum Perfusion ($P_{\mathbf{min}}$)

Here, we explore the critical parameter of Minimum Perfusion ($P_{\min}$), which provides insights into the lowest recorded perfusion levels experienced by different mouse groups following the ligation procedure. The findings in Figure 4.9 depict a consistent trend among all mouse groups, as they collectively exhibited reduced perfusion to a value between one-fifth and one-third of the baseline levels. While it may appear that healthy animals experienced a nominally greater reduction in perfusion compared to their diabetic counterparts, it is essential to note that the only statistically significant difference was observed between the healthy and DS male groups. This particular disparity underscores the importance of accounting for sex, fitness level, and health status when interpreting the physiological responses to vascular perturbations.

The observation of reduced perfusion levels following ligation raises pertinent questions about the underlying mechanisms and potential clinical implications. This decline in perfusion, while consistent across the groups, suggests a substantial disruption in blood flow to the affected hindlimb muscles. However, the identification of

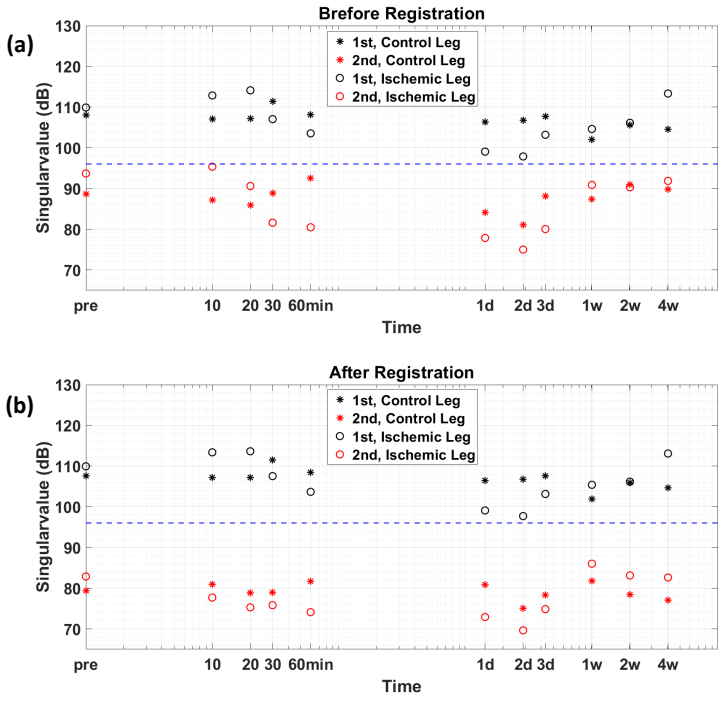

Figure 4.8: The first two singular values from singular spectra obtained at each muscle measurement time are plotted for the ischemic (right) and control (left) hindlimbs. Comparing values before spatial registration of the echo frames (a) with those after registration (b) shows that spatial registration increases the difference between the first and second singular values. Greater separation generates less overlap between the clutter and blood subspaces, thus increasing the reliability of clutter filtering. From Elsevier with permission.

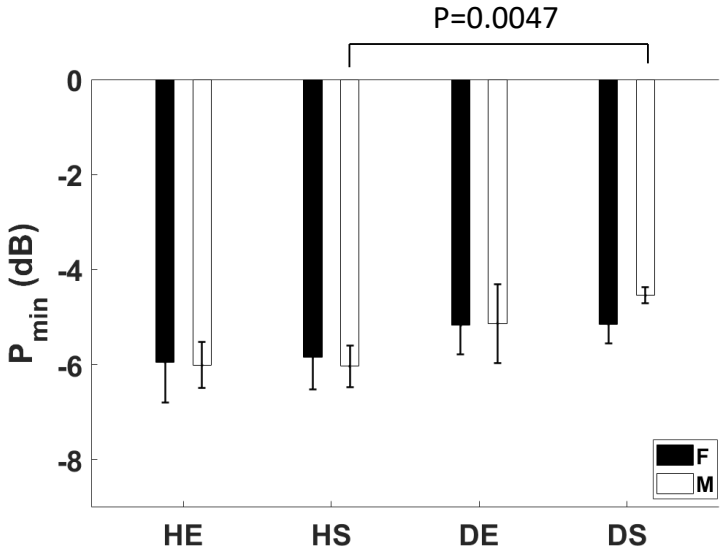

Figure 4.9: The average reduction in perfusion relative to baseline within the right hindlimb muscles, $P_{\min}$, is shown for the eight mouse groups. Significant differences are indicated by p values between compared groups. Error bars indicate ± 1 SE. From Elsevier with permission.

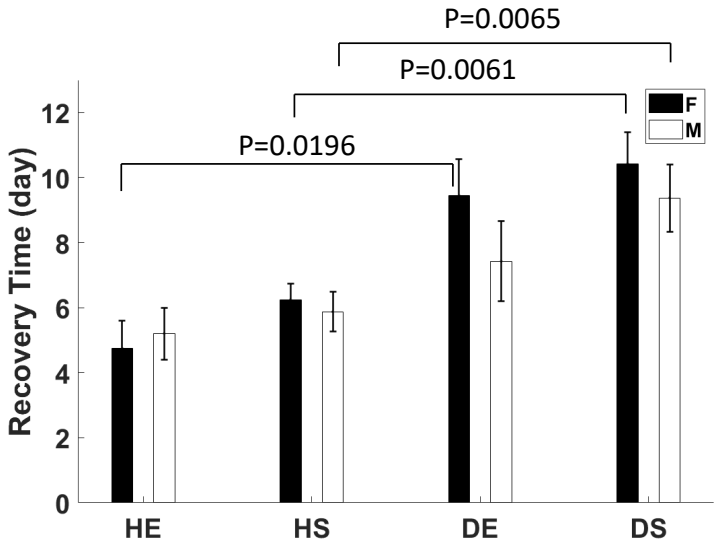

Figure 4.10: The time following ligation when perfusion returned to baseline values T [days] is shown for the eight mouse groups. Significant differences (p ¡ 0.05) were found between healthy and diabetic females and diabetic males. Error bars indicate ±1 SE. From Elsevier with permission.

a significant difference between healthy and DS males may hold implications for understanding how diabetes interacts with other biological factors in shaping the vascular response to ligation.

4.3.5 Recovery Time ((T)

Our attention now shifts to the crucial parameter of Recovery Time (T), which sheds light on the duration it takes for muscle perfusion to return to baseline levels following the vascular perturbation. The insights presented in Figure 4.10 illustrate notable differences in recovery times between various groups of mice. Observations reveal that muscle perfusion recovery is more rapid in healthy female mice compared to diabetic female mice, irrespective of their exercise regimen. A similar trend is observed in males. These findings suggest that diabetes may have an impact on the rate of perfusion recovery, with diabetic females, in particular, requiring more time to return to baseline perfusion levels when compared to diabetic males.

Furthermore, an intriguing trend emerges concerning the role of exercise in the recovery process. It appears that diabetic animals, both male and female, that engaged in exercise tend to recover more swiftly than their sedentary diabetic counterparts. However, it's important to note that while these trends are evident in the data, they do not reach the threshold of statistical significance. The differential rate of recovery observed between healthy and diabetic mice, as well as the potential influence of exercise, holds implications for understanding the interplay between diabetes, exercise, and vascular responses. These findings may contribute to a broader comprehension of the dynamics of vascular recovery and inform potential therapeutic strategies in the context of vascular health.

4.3.6 $P_{\max}$, FMD, and RH: Insights into Vascular Dynamics

We will now take a closer look at the critical parameters of $P_{\max}$, FMD, and RH to gain a deeper understanding of the vascular dynamics in the context of the ischemic hindlimbs, as illustrated in Figures 4.6 b and 4.6 d.

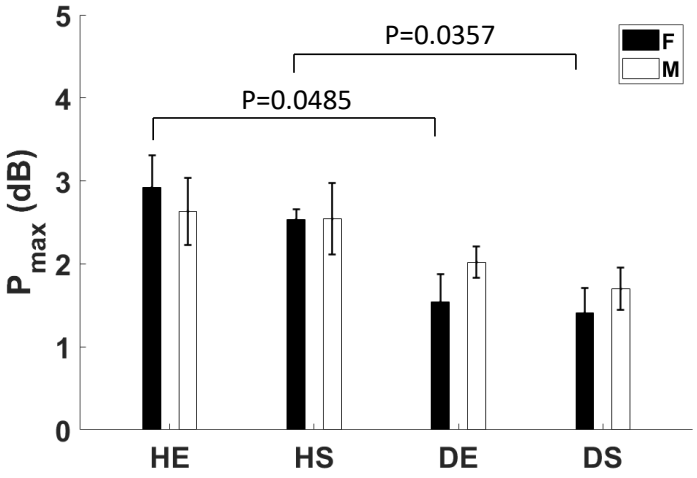

Figure 4.11: The magnitude of the spike in muscle perfusion appearing 20 min post-ligation $P_{\min}$ in Figure 6 is shown for the eight mouse groups. Error bars indicate ±1 SE. From Elsevier with permission.

One prominent feature within the perfusion profiles is the appearance of a 2-3 dB spike in muscle perfusion approximately 20 minutes after the femoral ligation procedure. This transient surge in perfusion is a notable characteristic that can be seen across all eight experimental groups, and it is represented in Figure 4.11 as $P_{\max}$ estimates. This figure highlights significant differences between paired healthy and diabetic groups, signifying variations in this particular parameter.

A plausible explanation for this brief surge in perfusion is related to changes in the tone of resistance arteries and arterioles due to the release of NO from collateral vessels that are adapting to the sudden ischemia following femoral ligation. This hypothesis is further validated by results from a side study, as summarized in Figure 4.12. In this side study, we repeated perfusion measurements in mice during the first 60 minutes after ligation, represented by solid lines showing the average PD-US estimates in the ligated and control hindlimbs of four mice. Subsequently, we injected the NOS inhibitor, L-NAME, into an additional five mice 60 minutes before ligation and repeated the measurements. The results of this side study confirm the high correlation between the 20-minute perfusion peak and endothelium-dependent NO activity. Notably, the administration of L-NAME completely eliminated the 20-minute peak without significantly altering perfusion in the control hindlimb. Consequently, it is reasonable to conclude that the lower peak perfusion observed in diabetic mice (Figure 4.11) is a consequence of endothelial dysfunction related to NO regulation.

To further explore the extent and localization of endothelial dysfunction, we conducted measurements of both FMD and RH before femoral ligation, utilizing a 5-minute pressure-cuff occlusion. The results, presented in Figure 4.13, indicate a reduction in FMD in DS mice when compared with HS mice. This suggests that exercise provides a degree of protection against endothelial dysfunction in the conduit arteries of diabetic mice. Additionally, Figure 4.13 b illustrates a reduction in the RH index for all diabetic groups, implying that endothelial dysfunction extends to resistance vessels. These findings provide compelling evidence of diabetic-induced alterations in endothelial function, affecting both conduit and resistance vessels.

It's worth noting that the data in Figures 4.11 and 4.13 consistently support the presence of diabetic-related changes in endothelial function. However, FMD and RH measurements are more sensitive indicators

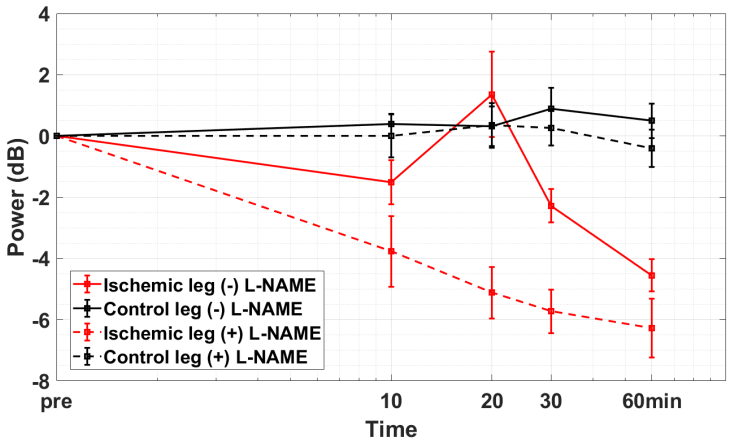

Figure 4.12: PD-US measurements for the ischemic hindlimb (red) and control hindlimb (black) up to 60 min post ligation for HS male mice. The dashed lines describe perfusion in mice receiving an i.p. injection of NOS inhibitor L-NAME 60 min before ligation (N = 5). Solid lines describe perfusion in mice without L-NAME injections (N = 4). Error bars indicate ±1 SE. From Elsevier with permission.

compared to $P_{\max}$, as they provide a deeper insight into vascular dynamics. To enhance the robustness of our analysis, male and female groups were combined for the measurements reported in Figure 4.13, thereby increasing the sample size to 10.

In summary, the evaluation of $P_{\max}$, FMD, and RH offers valuable insights into the vascular responses in the context of diabetes, exercise, and endothelial function. These findings contribute to an understanding of the intricate interplay between vascular parameters and health-related factors.

4.3.7 Changes in Body Weight: A Consideration in Perfusion Profiles

Here, we address the aspect of changes in body weight and its potential implications for the comparison of perfusion profiles between healthy and diabetic mice. The motivation for this investigation arose from the findings of Belcik et al. [75], which highlighted a correlation between insulin resistance, often linked to increased body weight and reduced microvascular blood flow and capillary blood volume in skeletal muscle. This correlation prompted our exploration of the complex influence of body weight when analyzing perfusion profiles. The observations, as summarized in Table 4.1, reveal that the diabetic groups were significantly heavier than their healthy counterparts at the time of the baseline measurements. Moreover, Figure 4.14 provides an additional perspective on these weight changes. It is evident that all mice experienced a weight loss ranging from 4 to 8 grams during the week following the right femoral ligation procedure. While this weight loss continued over the subsequent four-week trial in sedentary animals, it stabilized in animals that adhered to an exercise regimen.

One interesting aspect to highlight is that exercise emerged as the variable most correlated with time-dependent weight loss among the eight experimental groups. Despite this strong correlation, it is noteworthy that exercise had no significant effect on perfusion, as reported in Figures 4.9 -4.11. Therefore, it is reasonable to conclude that variations in mouse body weight had little effect on the relative perfusion profiles. These findings are significant as they suggest that, while changes in body weight are evident across the experimental groups, these variations do not significantly impact the perfusion profiles. This observation is particularly valuable as it implies that other factors, such as diabetes and exercise, may play more dominant roles in

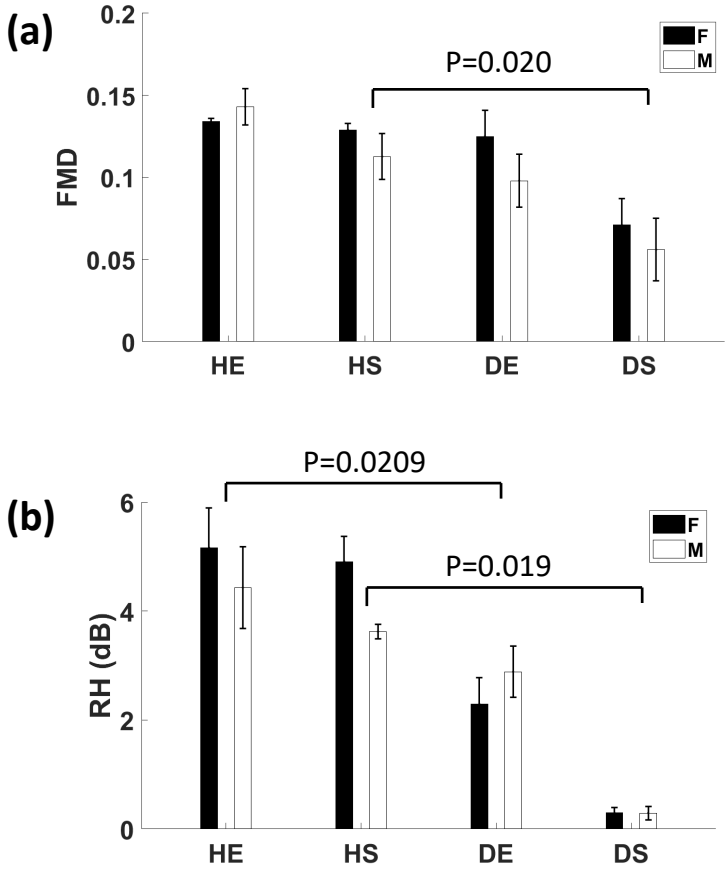

Figure 4.13: (a) FMD of the femoral artery applied to the control (left) hindlimb before right femoral ligation. (b) RH index estimated for the same groups measured at the same time as FMD describes the peak in excess muscle perfusion following 5 min pressure cuff occlusion. Error bars indicate ±1 SD. From Elsevier with permission.

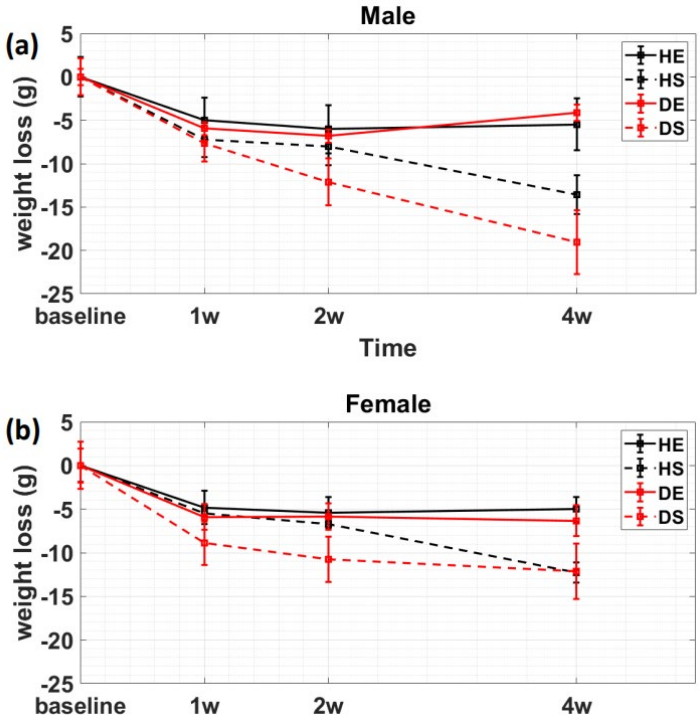

Figure 4.14: The change in mean body weight for each of the eight mouse groups during the four-week study. While all mice lost at least 4 g during the first week after ligation, the weight of animals that exercised stabilized while that of sedentary mice declined. From Elsevier with permission.

shaping the observed perfusion dynamics.

4.4 Discussion

4.4.1 Recovery Time

The results presented in this study illuminate the sensitivity of PD-US estimates to the diabetes-related changes in perfusion experienced during ischemic challenges. Our investigation revealed that all mice in the study managed to recover their baseline levels of muscle perfusion within four weeks following femoral ligation. However, what stands out prominently is the fact that the perfusion recovery time (T) exhibited substantial increases, with an average of 47% in diabetic males and 74% in diabetic females when compared with their non-diabetic counterparts. This protracted recovery period in diabetic mice holds significant clinical relevance. Notably, our findings align with the observations of other investigators [76] and [77], who reported incomplete recovery after 14 days when monitoring perfusion at the surface of the foot and calf muscles in diabetic mouse models compared with non-diabetic controls. While the specific ischemic response may exhibit variations based on the details of each experimental approach, the consistent findings of diminished and delayed perfusion recovery underscore the vascular endothelial damage anticipated during persistent hyperglycemia in insulin-resistant mice [78]. This emphasizes the critical role of endothelial function in the context of diabetes and its implications for vascular responses.

4.4.2 The Effect Of Exercise

A key aspect of our investigation was to assess the potential influence of exercise on vascular responses. The literature reports that exercise training has the capacity to enhance overall endothelial function in humans with no clinical evidence of vascular disease [79]. Our study corroborates these observations, as we found that exercise effectively preserved endothelial function in diabetic mice, as illustrated in Figure 4.13. However, it is noteworthy that our data also indicate that, aside from endothelial function, fitness levels had a minimal effect on the perfusion profile describing ischemic recovery.

4.4.3 The Effect Of Body Weight

The impact of body weight on the experimental outcomes is another aspect we scrutinized. Our findings revealed that, in the group of animals that adhered to an exercise regimen, body weight tended to stabilize within a week following surgery. In contrast, sedentary animals continued to lose weight over the entire four-week duration of the study, as depicted in Figure 4.14. This observation correlates with the active behavior of healthy animals, irrespective of their fitness levels, after surgery. It was evident that greater activity was linked to stable body weight and deeper ischemia, as indicated by the lower values of P_{min} in Figure 4.9.

4.4.4 The Effect Of Age

The most consistent parametric differences observed in this study were evident when comparing sedentary healthy and sedentary diabetic mice, a pattern observed in both male and female groups. An intriguing aspect that should not be overlooked is the age factor, as highlighted in Table 4.1. Age, indeed, emerges as a confounding factor in perfusion recovery, compounded by the presence of diabetes. It is essential to recognize the intricate interplay of these variables in shaping vascular responses. A noteworthy study by Farber et al. [51] provides insights into the impact of age on vascular responses. Their findings revealed that healthy older mice exhibited fewer and smaller-diameter native collateral vessels, leading to increased severity of ischemic injury following ligation and slower perfusion recovery. Similarly, Westvik et al. [80] reported delayed recovery in older healthy mice compared to their younger counterparts when subjected to ischemic hindlimb challenges. Despite the higher capillary density observed in older mice, suggesting a vigorous angiogenic response to ischemia, perfusion recovery remained attenuated due to significantly impaired arteriogenic responses.

4.4.5 Diagnosis of PAD

One crucial aspect that surfaces from our findings is the long-term loss of endothelium-dependent vasodilation in both conduit and resistance arteries. This phenomenon holds profound implications, particularly in the context of PAD, which escalates a patient's risk of developing coronary artery and cerebrovascular diseases [81] [82]. While there is no direct evidence of mice developing PAD during our experiment, the apparent diabetes-related endothelial dysfunction in these mice parallels the prominent vascular challenges faced by patients in the process of developing PAD. Consequently, the paradigm for addressing intermittent claudication and vascular health in humans is shifting towards interventions that prioritize the enhancement of endothelial function [83], particularly in resistance vessels that are most profoundly affected by metabolic diseases [49]. The insights garnered from this study reinforce the significance of investigating the influence of age, diabetes, and their combined effects on vascular responses. The findings in this context contribute to

a broader understanding of the complexities underlying perfusion dynamics and their relevance to clinical scenarios.

4.4.6 RH Index

Peripheral arterial tonometry (RH-PAT) is a well-established clinical technique employed for the assessment of endothelial function in resistance vessels [49], [84], [85]. RH-PAT devices provide a non-invasive means of measuring arterial pulsatile volume changes at the fingertip or forearm during RH following short-duration ischemic episodes [77]. In this context, PD-US imaging offers a site-specific alternative to RH-PAT, where ultrasonic echo-signal power, primarily originating from the motion of red blood cells, is spatially mapped. It is essential to highlight the assessment of the intra-subject coefficient of variation (CV) in the context of RH-PAT. Reports indicate that in young human males, the CV for RH-PAT measurements falls within the range of 15-22% [84]. In comparison, the CV for PD-US-based RH measurements, as depicted in Figure 4.13 b for healthy male mice, ranges from 8-29%, and this variability increases to 16-46% in diabetic males. This variation in PD-US measurement reproducibility is notably influenced by several factors, including the accuracy of selecting a consistent ROI in the muscle, the day-to-day perfusion changes linked to activity, and our ability to minimize tissue motion during echo acquisition to optimize the effectiveness of PCA clutter filtering.

4.4.7 NO Peak

One intriguing observation from our study is the absence of literature reports regarding the 20-minute perfusion peak seen in Figure 4.6 and quantified in Figure 4.11. Figure 4.12 provides a clear depiction of the correlation between this peak and NO-mediated dilation. While the height of this peak is linked to endothelial function, it is important to note that this measurement exhibits less sensitivity compared to other established methods such as FMD and the RH index when implemented via PD-US measurements.

In conclusion, this study highlights the intricate interplay of various factors that impact perfusion recovery, including age and diabetes, and their broader implications for vascular health. The observed endothelial dysfunction in mice parallels pathophysiological processes seen in patients developing PAD, opening avenues for further investigation aimed at enhancing clinical interventions for vascular diseases. These findings underscore the complexity of perfusion dynamics and offer valuable insights with the potential to improve our understanding and management of vascular health.

4.5 Summary

This study aimed to investigate the capabilities of power-Doppler ultrasonic (PD-US) imaging without contrast enhancement in monitoring changes in muscle perfusion over time. Ischemic recovery was examined in male and female mice, both healthy and type II diabetic, with and without exercise interventions. The study also included perfusion measurements during and after 5-minute ischemic periods, as well as during the four-week recovery phases following irreversible femoral ligation. The primary goal was to assess how diabetes-related changes in endothelial function influenced perfusion. The key findings of this study are as follows:

1. The average recovery time following ligation increased by 47% in diabetic males and 74% in diabetic females compared to non-diabetic mice, underscoring the impact of diabetes on skeletal muscle's ability

to recover from ischemic challenges.

2. Sedentary diabetic mice exhibited a significant decline in FMD in conduit arteries and the RH index in resistive vessels, with values approximately halved compared to sedentary non-diabetic mice. These results emphasize the detrimental effects of diabetes on endothelial function.

3. Exercise interventions were found to mitigate the loss of endothelial function associated with diabetes in both male and female mice, highlighting the potential of exercise as a therapeutic strategy to counteract diabetes-related vascular dysfunction.

4. Reproducibility of perfusion measurements was limited primarily due to challenges in consistently selecting the same region in muscle and effectively filtering out tissue clutter.

In conclusion, this study has demonstrated that PD-US measurements can accurately track site-specific changes in skeletal muscle perfusion over time, particularly in the context of diabetes. The results address the need for reliable techniques capable of continuously monitoring atherosclerotic processes. These findings contribute to our understanding of the intricate relationship between diabetes, vascular health, and the potential benefits of exercise interventions, shedding light on avenues for improved clinical management of vascular diseases. In the Next Phase of our study, we scale the animal model up to be more compatible with human size. For this we use a pig model that Expands on rodent findings, using 5-MHz ultrasound pulses for deeper muscle perfusion measurements. We utilize a method to induce progressive muscle ischemia during a 1 to 4-week observation.

Chapter 5

Monitoring Peripheral Perfusion in a Porcine Model of Progressive Hindlimb Ischemia using PD-US

5.1 Study Overview

This section builds upon prior Mice-model studies to advance our understanding of PAD by employing a pig-model approach 4. This study introduces two crucial enhancements aimed at facilitating more accurate PD-US estimates for clinical assessments.

First, we employ a 5-MHz ultrasound pulse combined with a handheld probe to assess muscle perfusion at depths ranging from 2 to 4 cm. This represents a notable departure from previous mouse studies which utilized a fixed-position 24-MHz probe, focusing on much shallower depths of 2 to 5 mm. The deeper penetration capability of the 5-MHz US pulses is particularly advantageous for evaluating muscle perfusion in the context of PAD.

Second, we surgically placed an ameroid ring constrictor (ARC) on the right superficial femoral artery of each pig in our study. This procedure induced gradual and progressive muscle ischemia over a span of 2 to 4 weeks. This approach contrasts with the acute ligation of the mouse hindlimb in a previous study 4. The benefit of the ARC-induced ischemia model is that it more accurately mimics the gradual development of atherosclerosis in PAD patients over many years, in contrast to the abrupt occlusion observed in acute ligation. This distinction is vital because Yang et al. [86] have shown that the rate of arterial occlusion significantly influences the mechanisms governing blood-flow recovery. By inducing ischemia in a gradual manner, we allow the animal's body to adapt to the diminishing blood supply, mirroring the conditions experienced by PAD patients.

It is important to note that the pigs in our study were chosen for their young age and the absence of known PAD risk factors, such as inflammation, endothelial dysfunction, and hypertension. This selection was deliberate to eliminate confounding factors that could contribute to the development of atherosclerotic conditions. Nonetheless, the temporal changes in deep muscle perfusion observed in this human-scale model of progressive ischemia provide invaluable insights that anticipate the dynamic characteristics often encountered when monitoring PAD patients in clinical settings. These enhancements in our experimental approach pave

the way for more accurate and clinically relevant assessments of muscle perfusion in the context of PAD.

5.2 Methods

In the course of this research, we selected four healthy, 4-month-old castrated male Yucatan miniature pigs from Premier BioSource, located in Rensselaer, Indiana. These pigs were individually identified as #613, #614, #615, and #618. They were housed in pairs, creating a social and comfortable environment to ensure their well-being throughout the study. During the research period, the pigs had unrestricted access to both water and feed.

All experimental procedures were carried out in strict adherence to ethical guidelines established by the Institutional Animal Care and Use Committee (IACUC) at the University of Illinois at Urbana-Champaign. The research also conformed to the principles outlined by the American Veterinary Medical Association, emphasizing the paramount importance of ensuring the welfare and ethical treatment of the animals involved in the study.

5.2.1 Anesthesia and Surgical Preparation

Before the surgical procedures, each pig underwent a 12-hour fasting period to minimize the risk of complications. Anesthesia was initiated through the administration of premedications via the intramuscular (IM) route. The premedications included:

- Ketamine at a dosage of 10 mg/kg
- Midazolam at 0.2 mg/kg
- Morphine at 0.5 mg/kg
- Dexmedetomidine at 25 $\mu g/kg$

Additionally, a single dose of ceftiofur at 5 mg/kg was administered before surgery to reduce the risk of respiratory infection.

Isoflurane anesthesia was introduced by exposing each pig to 2% isoflurane in oxygen via a mask. Subsequently, endotracheal intubation was performed using a cuffed endotracheal tube, ensuring a secure airway for the pigs. The anesthesia was maintained at 2% isoflurane in 100% oxygen throughout the surgical procedures to ensure consistent and appropriate levels of anesthesia. Post-surgery, maropitant at a concentration of 10 mg/ml was administered intravenously (IV) at a dose of 0.5 mg/kg to prevent nausea and vomiting, which are common side effects of anesthesia. The depth of anesthesia was continually monitored by closely observing the vital signs of the pigs to ensure their safety and well-being throughout the surgical procedures.

5.2.2 Surgical Procedure

The surgical procedure was performed with strict adherence to aseptic techniques to minimize the risk of infection. A 9-cm incision was meticulously made in the skin and subcutaneous tissues along the longitudinal axis of the medial right hindlimb, starting from the inguinal ligament and extending towards the stifle muscle. The incision was carefully carried out using a #10 blade. Following the incision, the right superficial femoral

artery was isolated from the vein and surrounding tissues. This was achieved through a combination of both blunt and sharp dissection techniques using Metzenbaum scissors, ensuring the delicate handling of the tissues. A crucial component of the surgical procedure involved the placement of a 3.5 mm ameroid ring constrictor (ARC; Research Instruments NW, Lebanon, OR) around the proximal portion of the vessel. To secure the ring in place, Kelly hemostatic forceps were employed, allowing for the insertion of the key to complete the ring formation. This precise placement was vital to achieve the intended constriction of the artery. To further secure the ring proximally and prevent any unintended slippage distally, a single interrupted suture of 3-0 PDS was meticulously placed. This suture passed through the fascia and muscle of the pectineus muscle and through the lumen of the ARC. This step was crucial in maintaining the constriction and ensuring the success of the procedure.

For postoperative pain management and analgesia, liposomal bupivacaine at a concentration of 13.3 mg/ml was injected into the incised tissues at a dose of 2.6 mg/kg. The specific product used for this purpose was Nocita^{TM} by Elanco, Greenfield, IN. Additionally, for inflammation control and pain management, a single IV administration of flunixin meglumine at a dose of 1 mg/kg was given postoperatively. To further address postoperative pain, buprenorphine at a concentration of 1.8 mg/ml was administered once, IM, at a dose of 0.02 mg/kg. The meticulous execution of this surgical procedure, combined with comprehensive postoperative pain management and analgesia, ensured the well-being and comfort of the subjects, and the successful implementation of the experimental model.

5.2.3 Postoperative Care and Monitoring

Following the successful completion of the surgical procedures and the recovery of the pigs from anesthesia, they were discharged from the hospital and transferred to an institutional research farm. During their stay on the farm, the animals were subject to daily observation over the four-week study period. This systematic and continuous observation was crucial to ensuring their well-being and tracking their progress.

Given the absence of established pain scales designed specifically for pigs, the evaluation of postoperative pain required a comprehensive approach. Clinical parameters were meticulously monitored during the initial 3-5 days post-operatively to assess any signs of pain or discomfort. These parameters included the assessment of respiratory rate (RR). Abnormal findings related to RR were defined as any of the following:

- RR exceeding 60 breaths per minute (bpm).
- Rapid and shallow breathing patterns.
- Manifestation of dyspnea.
- Any aberrant or unusual behavior.

In cases where signs of pain were observed, appropriate pain medication was administered as needed. The careful and individualized management of postoperative pain was a priority to ensure the pigs' comfort and recovery. It is noteworthy that, throughout the study, no animal exhibited excessive pain necessitating rescue analgesia, and there were no significant postoperative complications. This observation underscores the effectiveness of the surgical and postoperative care procedures in place, demonstrating the successful management of the animal subjects during the study. The comprehensive clinical monitoring and attentive postoperative care contributed to the overall success and ethical handling of the research subjects.

5.2.4 Ameroid Ring Constrictors (ARCs)

ARCs represent a valuable medical tool employed in clinical veterinary practice. They are primarily used to gradually occlude extrahepatic portosystemic shunts, offering an alternative to traditional suture ligation techniques [87]. These shunts involve abnormal vascular connections that bypass the liver, and their occlusion is crucial to redirect blood flow through the liver for proper metabolic processing. The ARC itself possesses a distinctive doughnut-shaped design, featuring an outer surface made of stainless steel (Figure 5.1a). Its interior is filled with a unique ameroid material, which consists of compressed casein, a highly hygroscopic milk protein derivative. This material exhibits a distinctive property - it expands when exposed to body fluids. As the ameroid material gradually absorbs fluids from the surrounding tissue, it undergoes expansion. This expansion process triggers the formation of fibrous clots, effectively occluding the target vessel. Studies have reported that ARCs are capable of reducing femoral arterial flow by more than 80% within a relatively short timeframe of 2-4 weeks [88].

For visual reference, Figure 5.1 illustrates the implantation of an ARC into pig 613, providing a clear depiction of this crucial component of the surgical procedure. The deployment of ARCs in medical practice, as highlighted in this context, plays a pivotal role in the gradual and controlled occlusion of specific vessels, ensuring successful and well-regulated physiological changes in the subjects under study.

5.2.5 Ultrasound Scanning

The process of ultrasound scanning played a pivotal role in our study, enabling us to monitor critical physiological changes in the subjects. Each animal underwent weekly ultrasound imaging sessions, commencing one week after the surgical procedure. The measurements obtained during the first week served as a reference baseline against which subsequent measurements were compared, allowing us to describe alterations in muscle perfusion and femoral artery blood velocity over time.

Upon the animals' arrival from the research farm, a specific anesthesia regimen was administered to prepare them for ultrasound scanning. Each animal received a calculated dose of 0.05 mL per kilogram of body weight of TKX. This anesthetic blend comprised as following per milliliter of solution:

- 50 mg of tiletamine
- 50 mg of zolazepam
- 80 mg of ketamine
- 20 mg of xylazine.

This ensured the safe induction of anesthesia. The anesthetized animals were carefully weighed and subsequently placed on a scanning table. To maintain anesthesia throughout the ultrasound session, the animals were intubated and received a continuous supply of 1-4% isoflurane in 100% oxygen, tailored to their individual requirements, for a duration of up to two hours. The ultrasound scans were systematically recorded in three scan planes on both hindlimbs. The animals were positioned either in the prone or lateral positions, as illustrated in Figures 5.2 a and 5.2 b. To minimize body movements during echo acquisition, ventilation was temporarily halted for approximately 30 seconds, ensuring the stability of the ultrasound probe relative to the target area. The three scan planes represented in Figure 5.2 specifically targeted three distinct muscle groups:

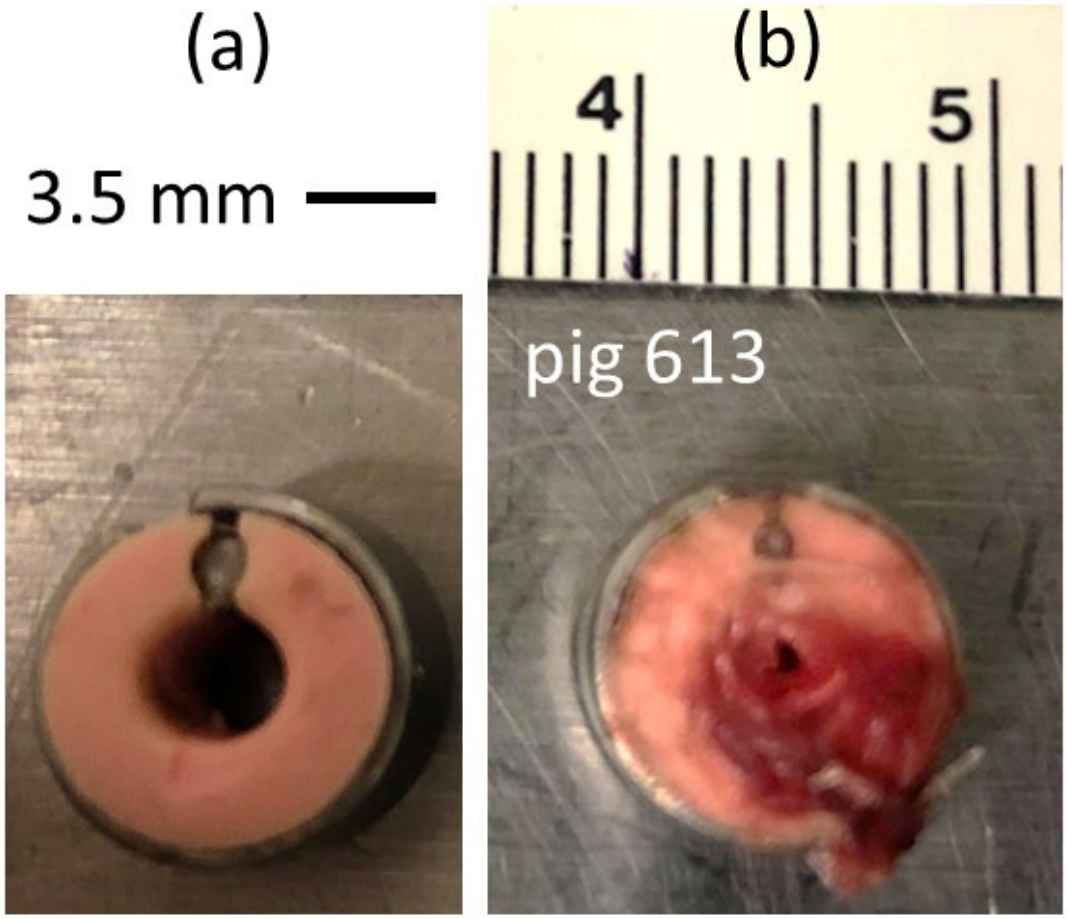

Figure 5.1: The 3.5 mm ARC before implantation into pig 613 (a) and recovered four weeks after implantation (b).

1. the vastus lateralis (S1)
2. the vastus medialis (S2)
3. the tensor fasciae latae (S3).

These scans were instrumental in estimating muscle perfusion via PD-US. Additionally, S1 was employed for spectral Doppler measurements to estimate the relative blood velocity in the femoral artery. To validate that these selected muscles were indeed perfused by the superficial femoral artery, a separate postmortem study was conducted. This involved visualizing the distribution of dye within each muscle following the arterial infusion of a contrast agent, as exemplified in Figure 5.2 g. The ultrasound scanning procedure, combined with targeted measurements and anatomical verification, offered a comprehensive means of assessing the subjects' physiological changes, providing valuable insights into the effects of the surgical intervention over time.

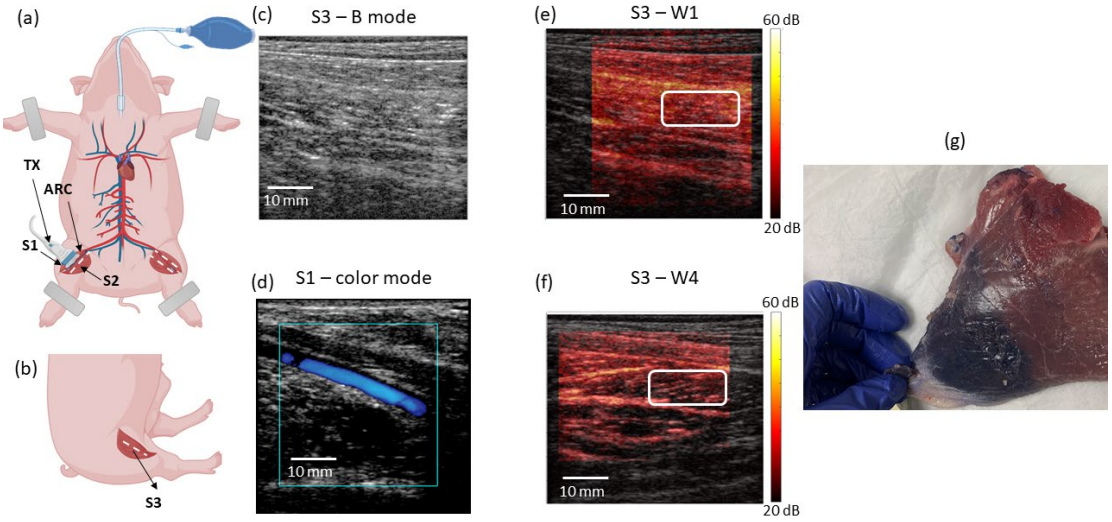

Figure 5.2: (a, b) Scan planes S1, S2, and S3 and location of the ARC are illustrated in the ischemic pig hindlimb muscle. Similar scan planes were selected for the control left hindlimb. An example B-mode image from S3 (c) and a color-flow image from S1 (d) from which Doppler spectra are estimated (Figure 5.3 c). (e, f) PD-US images are presented as color overlays onto B-mode images of muscle at S3 at one week (W1) and four weeks (W4) following surgery to install the ARC. White boxes indicate the 1×2 cm regions over which spatially averaged PD-US values (Fig. 3a and 3b) are estimated. (g) A postmortem injection of blue dye into the occluded artery indicates regions most likely to be ischemic. The blue color guided scan plane selection. Illustrations in (a) and (b) were created with BioRender.com.

Imaging and Data Collection

The four pigs were subjected to ultrasound imaging for the assessment of muscle perfusion and the Blood Flow in the superficial femoral artery. Pigs 615 and 618 were imaged for a duration of two weeks, whereas pigs 613 and 614 were monitored over a period of four weeks. Interestingly, the results for pig 615 revealed no significant changes in muscle perfusion and no notable alterations in the inner diameter of the ARC. Consequently, the perfusion data for pig 615 were not included in the analysis.

Ultrasound Imaging Setup

Hindlimb imaging was performed using a Sonix RP 410 ultrasonic imaging system manufactured by Ultrasonix Medical Corporation, located in Richmond, British Columbia, Canada. The system was equipped with an L14-5 linear array transducer that transmitted 5 MHz pulses.

Data Acquisition

RF echo signals were acquired at 20 MHz from both broadband B-mode echo frames (see Figure 5.2 c) and narrowband C-mode echo frames using the scanner's research mode. All perfusion data estimates based on PD-US were generated offline from the CF mode recordings.

5.2.6 Additional Measurements

In addition to perfusion data, CF images (as depicted in Figure 5.2 d) and pulsed-Doppler spectra (as shown in Figure 5.3 c) were recorded to estimate peak systolic blood velocities in the femoral artery distal to the ARC.

Animal Body Weights

The body weights of all animals were measured at regular intervals throughout the study and are presented in Table 5.1 for reference.

Pig #	Week 1	Week 2	Week 3
615	25 Kg	28 Kg	-
618	29 Kg	31 Kg	-
614	25 Kg	30 Kg	31 Kg
613	28 Kg	31 Kg	32 Kg

Table 5.1: Mini-pig body weight measurements (kg) during the four-week study.

These comprehensive imaging and data collection methods were employed to provide a thorough assessment of muscle perfusion and related parameters in the study animals.

5.2.7 Frame Sampling and Doppler Frame Analysis

In the ultrasound imaging process, frame sampling played a crucial role in capturing relevant echo signals for the analysis of muscle perfusion. Specifically, the following steps were taken:

Color Box Adjustment

Within each scan plane, the size of the color box for CF acquisitions was meticulously adjusted to encompass the echo signals originating from the pertinent muscles of interest. This adjustment was necessary due to variations in the size and depth of the color box.

Pulse-Repetition Frequency (PRF) Adjustment

To accommodate the variable size and depth of the color box, the pulse repetition frequency (PRF) for the 10-frame ensemble recorded within each Doppler frame was automatically adjusted. This PRF adjustment led to PRF values ranging between 1.5 to 3 kHz. Each Doppler frame contained 10 CF frames, which were recorded at the adjusted PRF. The PRF adjustment had a direct impact on the velocity range and resolution of PD-US estimates, as discussed below.

Temporal Sampling Interval

PD-US estimates were compiled throughout the scan plane from a total of 60 Doppler frames, recorded at a rate between 9 to 16 fps. The acquisition time, during which tissue motion was minimized, varied between 3.75 seconds and 6.67 seconds. The 60 Doppler frames were organized into three groups of 20 frames each. Within each Doppler-frame ensemble, the first, fifth, and tenth CF frames were selected for subsequent analysis. The temporal sampling interval for power Doppler estimates was determined by the Doppler frame

rate and ranged from 1/16 seconds to 1/9 seconds. This ensured a comprehensive assessment of the dynamic changes in muscle perfusion.

5.2.8 Velocity Resolution and Range

The total time encompassed in each PD-US estimate ranged from 20/16 seconds to 20/9 seconds. As a result, the Doppler frequency resolution ranged between 9/20 Hz and 16/20 Hz over a measurement bandwidth that extended from ±9/2 Hz to ±16/2 Hz. Doppler frequencies (u) were converted into blood-cell velocities (v) by applying the pulsed Doppler equation:

$$v = cu/\left(2f_0 \cos\theta\right) \tag{5.1}$$

where $c = 1.54\,\mathrm{mm}/\mu\mathrm{s}$ is the speed of sound in tissue, $\theta = 60^\circ$ is the Doppler angle, and $f_0 = 5\,\mathrm{MHz}$ is the pulse transmission frequency.

The resulting velocity resolution was 0.139 mm/s at the low end and 0.246 mm/s at the high end, covering a net range of ±1.39 mm/s and ±2.46 mm/s, respectively. These parameters were carefully selected to encompass the typical range of blood cell velocities in the microvasculature, with an average velocity of approximately 0.3 mm/s and a peak value of 2 mm/s.

5.2.9 Aliasing Considerations

In the context of the collected data, it is important to note that between 5-15 samples within the blood-signal bandwidth were included in each PD-US estimate. Furthermore, it was observed that the aliasing of blood signals did not introduce distortions in the PD-US estimates, ensuring the accuracy and reliability of the data. The meticulous frame sampling and Doppler frame analysis procedures described above were essential for obtaining detailed insights into muscle perfusion and related parameters during the study.

5.2.10 Echo Registration and Clutter Filtering

During the acquisition process, it was observed that tissues exhibited motion of up to approximately one millimeter in relation to the beam axis of the handheld probe. This motion roughly corresponds to three wavelengths at the 5 MHz frequency used. To address this challenge and ensure the accuracy of the data, a spatial registration method was employed, as detailed second chapter [24]. Tissue echoes were meticulously aligned over the 20 sequential Doppler frames that were analyzed for each PD-US estimate.

Once the echoes were successfully registered, the SVD clutter filter was applied to the signals within the defined analysis region. The filter was set at a fixed threshold, as further described in the subsequent section. This process allowed us to effectively eliminate unwanted clutter and artifacts from the data. Subsequently, the filtered signal power at each spatial position within the PD-US image was computed. To improve the accuracy and quality of the PD-US images, temporal averaging was performed. The following steps were taken:

Measurement Bandwidth Averaging

Signal power within the measurement bandwidth was averaged over three sequential 20-frame time intervals at each spatial location within the tissue. This temporal averaging strategy aided in reducing noise and

enhancing the SNR.

Color Frame Selection

For each of the 20-frame time intervals, power measurements were obtained from the first, fifth, and tenth color frames within the ensemble. This selective frame sampling was instrumental in reducing the impact of tissue and blood cell motion while preserving the key information needed for the analysis.

Uncoupling Measurements

Given the relatively slow speeds of perfusing blood cells and the high PRF of the imaging system designed for flow assessment, estimating signal power from every fifth frame within the ensemble provided adequate temporal uncoupling of the measurements. This approach significantly reduced uncertainty during the temporal averaging process, resulting in more accurate and reliable data.

Image Formation

The final step in the data analysis involved mapping the PD-US estimates onto B-mode images using a color overlay. This technique allowed for the visualization and interpretation of the perfusion data, as illustrated in Figures 5.2 e and 5.2 f.

In summary, the combined processes of echo registration, clutter filtering, and temporal averaging were pivotal in enhancing the quality of the PD-US images and ensuring the accuracy of the results presented in this study.

5.2.11 Spatial Averaging for Temporal Perfusion Profiles

In order to provide a comprehensive representation of the temporal perfusion profiles, each data point presented in Figures 5.3 a and 5.3 b underwent further spatial averaging. This spatial averaging was carried out over the pixels contained within a specific 1 cm x 2 cm window, as indicated in Figures 5.2 e and 5.2 f.

Degrees of Freedom Adjustment

When computing the standard deviation after spatial averaging, it was essential to appropriately adjust the degrees of freedom. This adjustment was necessary to account for the 5-MHz speckle correlation area, estimated to be approximately 0.081 mm^2 [24]. Correctly assigning degrees of freedom played a crucial role in accurately representing the error bars reported in Figures 5.3 a and 5.3 b. The RF echo-sampling interval was 0.039 mm along the beam and 0.30 mm lateral to the beam axis, resulting in approximately 7 samples per speckle correlation area $0.081/(0.039 \times 0.3) \approx 7$. To account for this, the degrees of freedom were adjusted to $\frac{N}{\sqrt{7}} - 1$ during the computation of error bars.

Spatiotemporal Mean Calculation

The net spatiotemporal mean at a specific point in time for an individual animal was further averaged over the total number of animals included in the study. This averaging process allowed for the generation of an overall mean value, along with the corresponding SE. The results of this analysis, along with the calculated means and standard errors, are visually represented in 5.3 a and 5.3 . Sample sizes for each data point are indicated by numbers in proximity to the plotted points. These figures provide a clear and concise presentation of the

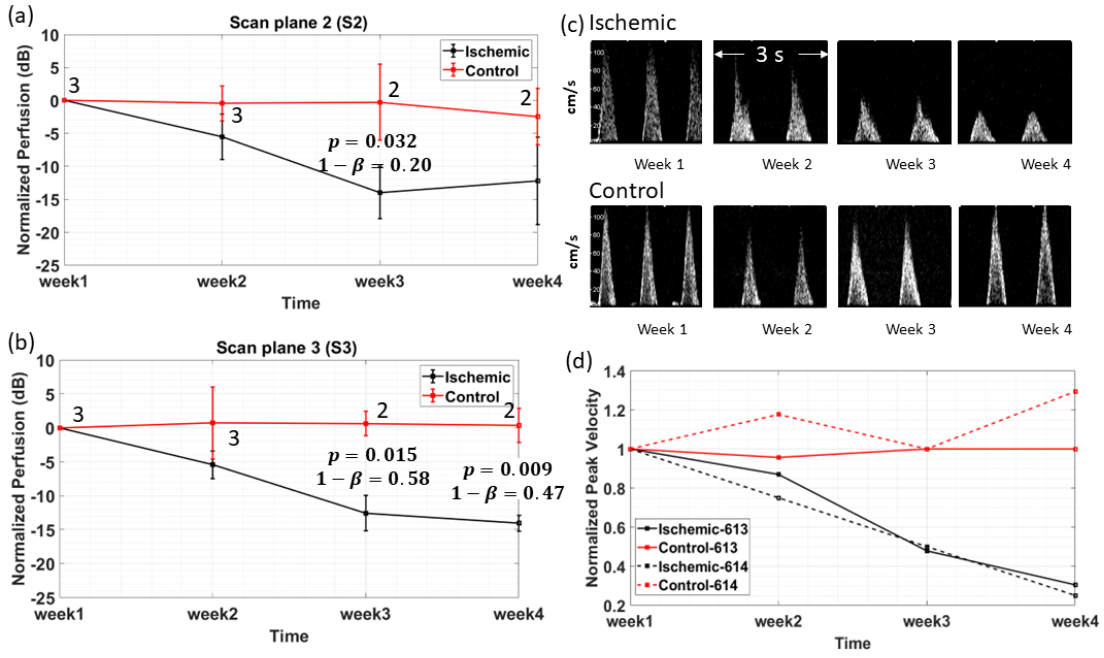

Figure 5.3: PD-US estimates of muscle perfusion for the ischemic and control hindlimbs over four weeks in scan planes S2 (a) and S3 (b). The anatomical locations of scan planes are marked in Figure 5.2. Values are normalized (0 dB) by the week 1 baseline values. Numbers 2 and 3 appearing near plot points indicate the number of animals included in the mean value, and error bars indicate ±1 SE. t-test results where differences between ischemic and control measurements were significant at the $p < 0.05$ level are shown along with statistical power estimate, 1- β. (c) Doppler spectra acquired over 3 s for pig 613 are shown for the ischemic and control hindlimbs over the four-week study. (d) Changes in mean peak systolic blood velocity are shown for the femoral artery of two animals relative to week 1 values.

findings, allowing for a comprehensive understanding of the temporal perfusion profiles and their associated uncertainties.

Accurate spatial and temporal averaging, along with proper degrees of freedom assignment, were essential in ensuring the robustness and reliability of the results presented in this study.

5.3 Results

5.3.1 Muscle Perfusion and Blood Velocity Estimation

The study aimed to assess muscle perfusion and blood velocity in the weeks following the placement of an ARC around the right superficial femoral artery. The results are presented in Figures 5.3 a and 5.3 b. Due to the unavailability of baseline perfusion values before ARC placement, we selected measurements from week 1 as the baseline. The changes in mean PD-US estimates are displayed for the right ischemic hindlimb (in black) and the left control hindlimb (in red) relative to this chosen baseline. Perfusion measurements were taken from one animal each week for two weeks and from two animals each week for four weeks. Figures 5.3 a and 5.3 b depict perfusion changes in scan planes S2 and S3, situated within the anterior-side and posterior-side hindlimb muscles, respectively. It is important to note that these muscle regions are typically perfused by the occluded artery, as confirmed by post-mortem dye infusions conducted during a pilot study.

The findings reveal that PD-US estimates for the control hindlimb remain relatively stable over time. In contrast, the ischemic hindlimb experiences a decline of 10 dB in S2 and 14 dB in S3 between weeks 1 and 4. By week 4, the average perfusion change amounts to -12 dB, indicating a significant 94% loss of perfusing blood-signal power in the ischemic hindlimb when compared to the control. This substantial loss in perfusion aligns with the observations in Figure 5.1, where the inner lumen diameter of the ARC for pig 613 decreased from 3.5 mm to less than 1 mm after 4 weeks. To evaluate these differences statistically, the null hypothesis was tested at each time point, comparing ischemic and control perfusion values in the S2 and S3 regions. The p-values representing differences at the 5% significance level are listed in Figures 5.3 a and 5.3 b. Additionally, the statistical power $(1-\beta)$ was calculated at time points with significant differences and is also provided in the figures.

Figures 5.3 c and 5.3 d illustrate that peak femoral artery blood velocity decreases to 30% of the baseline value between weeks 1 and 4. This velocity decline demonstrates an approximately linear trend over time, with velocity decreasing each week to 67% of the value observed in the previous week. Notably, there were no discernible systematic changes in femoral blood flow in the control hindlimbs.

These results offer valuable insights into the impact of ARC placement on muscle perfusion and blood velocity, providing an understanding of the observed changes over the study period.

5.3.2 Verifying Assumptions

In the pursuit of reliable muscle perfusion assessment using PD-US, it is imperative to validate the underlying assumptions and processes. Figures 5.4 and 5.5 provide insight into intermediate steps in the PD-US estimation process, offering a means to ensure the success of clutter filtering—a critical factor in establishing the reliability of the PD-US measurements presented in Figure 5.3.

Significance of Successful Clutter Filtering

Successful clutter filtering is fundamental in ensuring that the PD-US measurements accurately reflect muscle perfusion. The following figures serve as a visual representation of the validation process, examining the range of tissue movement, the efficacy of spatial registration, and the effects of alignment errors on the inter-frame echo correlation coefficient. Furthermore, they assess the potential impact of out-of-plane probe motion. Both Figures 5.4 and 5.5 delve into the assessment of tissue movement and the steps taken to mitigate its effects. These figures capture a spectrum of tissue motion scenarios encountered during freehand scanning, encompassing both relatively large tissue movements in Figure 5.4 and relatively small tissue motion in Figure 5.5.

In-Plane and Out-of-Plane Movement

In both figures, (a) quantifies the extent of in-plane motion detected by the spatial registration algorithm along the axial (beam axis) and lateral (perpendicular to the beam axis) dimensions. Predominantly, the detected motion corresponds to lateral probe translations, which can significantly impact the quality of the acquired data. The plots in (b) depict the residual motion that remains after the spatial registration process has been completed. This element is crucial in evaluating the effectiveness of the registration process and the extent to which it compensates for tissue movement. The figures collectively serve as an essential means of verifying that the assumptions and processes underlying the PD-US estimation methodology are robust and

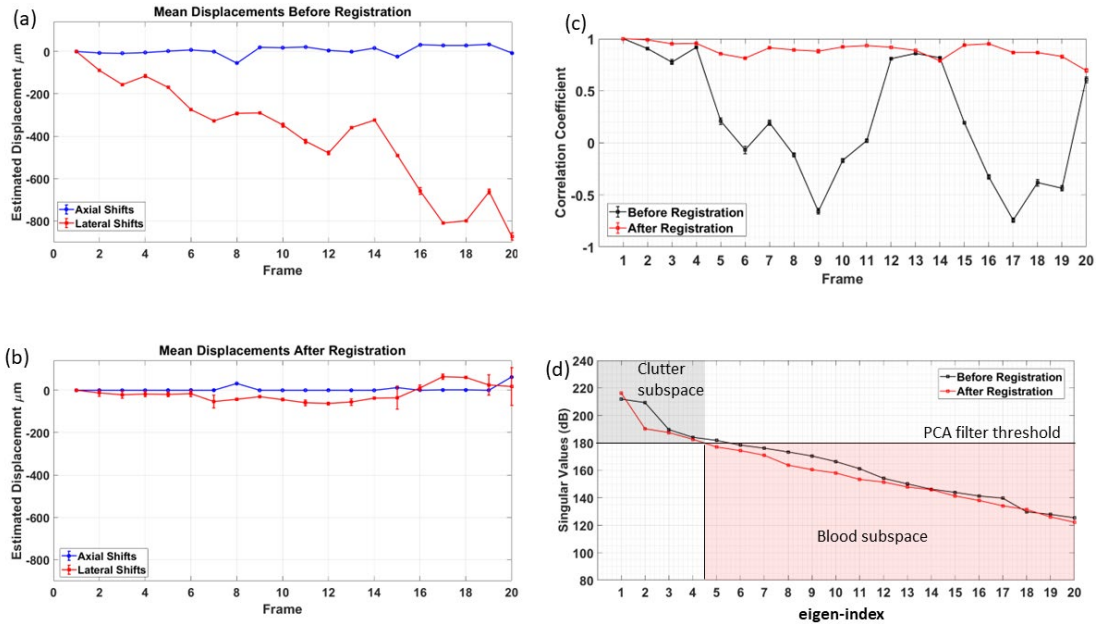

Figure 5.4: (a) Intermediate results during processing of one of the PD-US estimates in Figure 3a, where there is a relatively large (0.8 mm) lateral translation of tissue relative to the sound beam and a small (0.05 mm) axial translation. The movement occurred during a 1.25 s echo acquisition of 20 Doppler frames. (b) The residual translation of Doppler echo frames after spatial registration to align the frames, showing alignment errors ¡ 0.05 mm. Error bars denote ±1 SD. (c) Correlation coefficients for echo signals relative to the first frame are shown before and after spatial registration is applied. Spatial registration increased the average interframe echo correlation coefficient above 0.8. Smaller values indicate out-of-plane tissue movement. (d) The singular values for this 20-frame acquisition are shown before and after spatial registration is applied. Differences across the singular-value bandwidth show that large tissue motions generate broad-spectrum clutter-signal power that overlaps the blood-signal power unless the frames are spatially registered. A fixed clutter filter threshold at 180 dB determines the clutter and blood subspaces.

that the collected data accurately reflects muscle perfusion. This validation process ensures the integrity and reliability of the study's results.

5.3.3 Validation of Spatial Registration for Clutter Filtering

To validate the effectiveness of spatial registration in the context of clutter filtering, Figures 5.4 and 5.5 provide a detailed analysis of tissue movement and the associated registration process.

Figure 4: Large Tissue Motion

In Figure 5.4 a, it is evident that the net tissue translation amounts to 0.8 mm, equivalent to approximately 2.6 wavelengths, over the course of 20 frames. After spatial registration, as shown in Figure 5.4 b, the signals are precisely aligned within a minuscule range of 0.05 mm, or about 0.2 wavelengths. This exceptional alignment highlights the accuracy of the spatial registration process. The slight variation observed in the alignment of frames post-registration suggests that, in addition to in-plane motion, some probe motion perpendicular to the scan plane might have occurred. It is important to note that out-of-plane clutter motion, while increasing the uncertainty in displacement estimates for registration, does not introduce biases, staying

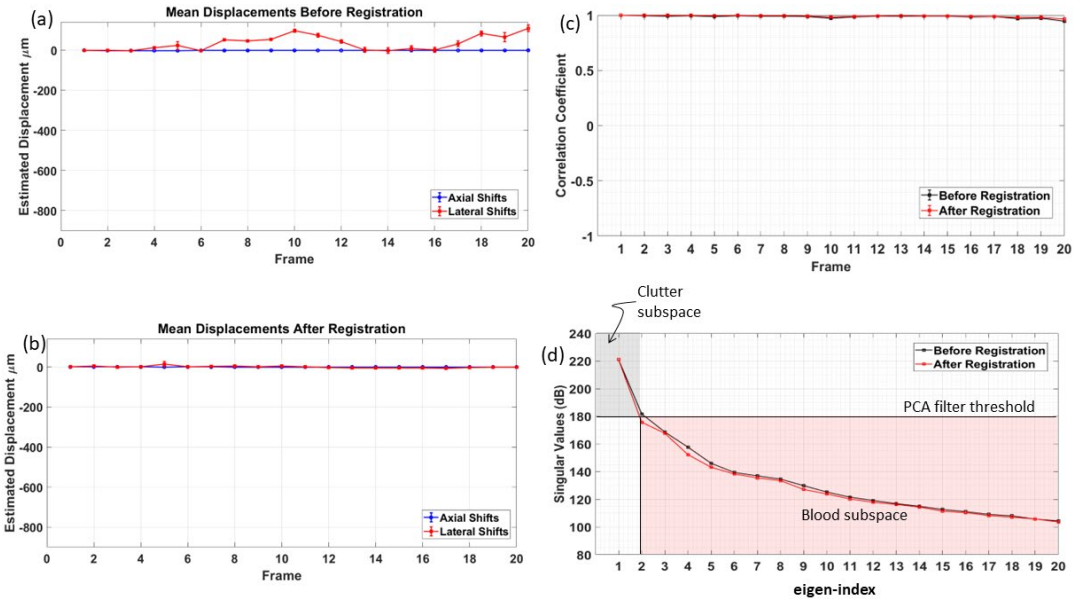

Figure 5.5: (a) Intermediate results during PD-US processing of one estimate in Figure 3a are shown, where there is a relatively small (0.1 mm) lateral translation of tissue and negligible axial translation during a 1.25 s acquisition. (b) The residual translation of Doppler frames after spatial registration is less than 0.005 mm. (c) Alignment is confirmed by the correlation coefficient for echo signals relative to the first frame are shown before and after spatial registration is applied. (d) The singular values for this 20-frame acquisition before spatial registration are like those after registration because the tissue motion is small. The clutter filter threshold set to 180 dB determines the boundary between the clutter and blood subspaces. With negligible tissue motion and homogeneous echogenicity over the analysis region, clutter power is confined to the first singular value.

within the limits documented in [24].

To enhance the precision of displacement estimates during registration, an innovative approach was employed. The size of the window for spatial averaging (indicated by white boxes in Figures 5.2 e and 5.2 f) was extended to the maximum extent possible while remaining within the muscle region in each scan plane. It's worth noting that tissue motions other than in-plane translations generate inter-frame echo decorrelations that cannot be restored using rigid registration techniques.

Figure 5: Small Tissue Motion

Figure 5.5 a presents a different acquisition scenario where the net tissue motion over 20 Doppler frames is minimal, measuring less than 0.1 mm laterally, which is approximately 0.33 wavelengths. In this case, the spatial registration algorithm successfully aligns these small subsample translations, as demonstrated in Figure 5.5 b. Given that the interframe correlation, as depicted in Figure 5.5 c, remains unaltered after registration, spatial registration proves unnecessary in such scenarios. Importantly, when spatial registration is applied, it does not introduce significant new displacement errors that would compromise the effectiveness of Singular Value Decomposition (SVD) filtering.

Advantages of Spatial Registration for Clutter Filtering

The benefits of spatial registration for clutter filtering are vividly illustrated in Figures 5.4 d and 5.5 d for cases involving both large and small tissue translations. In scenarios with significant tissue motion, spatial registration effectively adjusts the singular values across the entire spectrum (Figure 5.4d), ultimately eliminating clutter power contamination from the blood components. Conversely, in cases where clutter motion is minimal (Figure 5.5 d), the change in the singular spectrum before and after registration is likewise small. The comparative analysis in Figures 5.4 and 5.5 serves as a crucial validation, confirming that initially misaligned tissue-echo frames are successfully aligned through spatial registration. This alignment process enables the subsequent application of SVD clutter filtering with a fixed threshold, contributing to the success and reliability of the estimation process.

5.3.4 Clutter Filter Threshold

In all the data collected for this study, we employed an SVD filter threshold for the purpose of clutter rejection within the singular spectrum. Specifically, we set the threshold at 180 dB. Under this thresholding scheme, singular values below this threshold were retained as blood echoes, while those above the threshold were set to zero, effectively removing clutter from the dataset. It is important to note that the clutter-blood threshold value is sensitive to acoustic output and gain settings. Therefore, once determined, these values were consistently preset when tracking individuals over time. At this threshold setting, small tissue motion, as illustrated in Figure 5.5, typically results in only the first singular value being assigned to the clutter subspace for elimination by the SVD filter. This first singular value quantifies the echo power of the fundamental spatial mode that remains temporally stationary between Doppler frames. However, in cases involving larger tissue movements, such as those shown in Figure 5.4, the first four singular values are assigned to clutter and subsequently eliminated by the SVD filter. While there may be some blood-signal contributions within these singular values, simulations [24] indicate that the PD-US estimates more accurately reflect blood-signal power when all intense clutter elements are filtered.

5.3.5 Noise Filtering

In our approach, we did not set a secondary upper threshold in the singular spectrum to distinguish between blood and noise power. As we discussed in Chapter 2, under simulated conditions, where blood cells primarily move in a single direction [24], the inclusion of a noise filter can enhance the accuracy of blood-power estimates. This is because an interface between the blood and noise subspaces can be distinctly defined. However, in the context of in vivo muscle perfusion assessments, blood flow is typically spatially diffuse. This spatial distribution makes it challenging to establish a reliable noise threshold [37]. Given that our instruments maintained a consistent echo SNR of 30 dB [24], which remained constant over time, there was no necessity for noise filtering to monitor relative changes in PD-US estimates over time.

This choice in noise filtering reflects the unique characteristics of in vivo muscle perfusion assessments and the stability of our instrument's SNR, further supporting the reliability of the study's findings.

5.4 Discussion

5.4.1 Translation of Techniques to Lower Frequency

The techniques initially developed at 24 MHz for mouse studies were successfully translated to 5 MHz measurements in pigs with minimal modifications. Despite the larger probe movements introduced by handheld probes during mouse acquisitions compared to fixed probes, our spatial registration algorithm effectively aligned Doppler frames in both scenarios, ensuring the efficacy of clutter filtering. A notable aspect of our scanning technique was the temporary cessation of breathing in the animals for approximately 30 seconds to facilitate the recording of echo data. These scanning limitations obviate the need for injectable contrast agents when assessing relative changes in regional muscle perfusion over time.

5.4.2 Variations in Arterial Occlusion

One prominent distinction between the mouse and pig studies pertains to the nature of arterial occlusion. While muscle perfusion in mice displayed a recovery between 5-10 days post-ligation [63], the pig study revealed a steady decline over four weeks, as evidenced in Figures 5.3 a and 5.3 b. PD-US estimates in acutely ligated mouse hindlimbs consistently declined over two days post-ligation, reaching approximately -7 dB (80% reduction) of the pre-ligation baseline value. In contrast, PD-US estimates in the progressively occluded pig study decreased to -12 dB (94%) relative to the week-1 baseline value.

Comparative Studies

While there are no identical studies to compare with the substantial reduction in muscle perfusion observed in pigs, some related studies draw parallels. For instance, Hansen et al. [89] applied a tourniquet to the hindlimb of a 1-year-old Yorkshire female pig, observing a 95% decrease in muscle perfusion. They reported that perfusion returned to normal values within 30 minutes after releasing the tourniquet. Additionally, several studies have explored changes in vascular flow and blood velocity following acute femoral ligation in pigs. One such study indicated an immediate reduction in blood flow in the iliac artery to one-third of the baseline, with iliac flow subsequently restored to 73% of baseline within two weeks through arteriogenic processes acting on collateral vessels [90]. Another study found that acute femoral ligation initially reduced peak systemic blood velocity in the femoral artery distal to the ligation site to zero, followed by a gradual rise over seven weeks to approximately 30% of baseline values [91]. These studies suggest that a longer observation period may have revealed perfusion recovery in our pig study, highlighting the role of experimental design specifics and investigator-selected features in study outcomes.

5.4.3 Sample Size and Study Design

Another key distinction lies in the sample size used in the mouse study, allowing for statistical significance testing when drawing conclusions. In contrast, the pig study, which solely examined healthy animals, leans more toward an anecdotal case study approach. Nonetheless, it provides support for the utility of PD-US without contrast enhancement in monitoring changes in tissue perfusion over extended periods, a crucial aspect of following patients with PAD.

5.4.4 Blood Velocity Changes Post-Implantation

An anticipated outcome was the expected increase in blood velocity in the femoral artery post-implantation, assuming that the arterial response cuff (ARC) primarily narrowed the femoral lumen through external force. However, others [92] have reported that the ARC reduces arterial blood flow by inducing a fibrous thrombus within the artery at the ARC site, ultimately leading to complete occlusion of the vessel [93]. In this context, the gradual reduction in blood velocity depicted in Figures 5.3 c and 5.3d can be explained. It is noteworthy that there was a 5 dB reduction in perfusion loss during week 4 when perfusion was measured immediately after anesthesia administration.

5.4.5 Frequency and Tissue Scattering

Despite the lower frequencies employed (5 MHz), which result in a lower blood-to-tissue scattering ratio, the effectiveness of PD-US estimates remained intact. This underscores the advantages of ultrasound over LSCI in terms of its ability to probe deeper into tissues.

5.4.6 Relevance to PAD and Clinical Applications

It is important to acknowledge that while the ARC model does not yield a perfect representation of PAD, it is a notable improvement over acute ligation. Moreover, the observed responses in the ARC model are distinct, suggesting a more complex pathophysiological context. These findings may have implications for future studies exploring the pathophysiology of PAD. In a clinical context, quantitative perfusion measurements using PD-US estimates can serve as a valuable baseline for serial assessments of peripheral perfusion changes over time, benefiting patients with PAD and related conditions.

Chapter 6

Conclusions

6.1 Registration and Filtering Techniques

The core of this thesis has been an in-depth examination of the transformative role that spatial registration and SVD clutter filtering techniques play in refining PD-US imaging for PAD diagnosis. The meticulous process of spatial registration, aimed at optimizing the correlation coefficient among echo frames, significantly enhances the clarity and accuracy of PD-US estimates. This optimization is crucial for the effective application of SVD clutter filtering, which distinguishes blood flow from surrounding tissue echoes. Through detailed simulations and experimental validations, the research has confirmed the critical assumptions underpinning successful spatial registration, the spatial coherence of tissue scatterer movement and the significant contrast between tissue and blood echo intensities. These findings not only validate the technique's robustness but also pave the way for its application in complex in vivo settings, where dynamic tissue movements and varying echo characteristics present unique challenges. This work sets a new standard for accuracy in non-invasive PAD diagnostics by addressing and mitigating potential distortions from out-of-plane clutter motion.

6.2 Large and Small Animal Models

Exploring the application of PD-US across different animal models has shed light on the challenges and opportunities presented by varying anatomical and physiological contexts.

6.2.1 Small Animal Models: Precision and High-Frequency Ultrasound

In small animal studies, particularly rodents, PD-US employs high-frequency ultrasound pulses (24 MHz) to acquire data on blood flow in muscle tissues. This high frequency is advantageous due to the increased scattering of ultrasound waves by blood cells compared to tissue, enhancing the contrast and resolution of perfusion images. Rodent models have facilitated the development of disease models, such as acute femoral ligation, to induce and subsequently measure changes in muscle perfusion. These studies have been instrumental in validating PD-US's capability to monitor perfusion dynamics and assess endothelial function, critical for understanding PAD's pathophysiology. The precision and scalability of PD-US in small animal models demonstrate its potential for early-stage research and therapeutic evaluations.

6.2.2 Large Animal Models: Bridging the Gap to Clinical Relevance

The transition to large animal models, specifically pigs, marks a critical step towards clinical applicability. Utilizing lower-frequency ultrasound pulses (5 MHz) allows for the penetration needed to assess muscle perfusion at greater depths (2-4 cm), aligning closer with human anatomical conditions. This adaptation acknowledges the physiological differences between small and large animals, particularly in terms of tissue thickness and blood flow dynamics. The introduction of an ameroid ring constrictor to induce progressive muscle ischemia in pigs simulates the slow, gradual progression of PAD in humans, offering a more relevant model for studying the disease's long-term implications. This approach underscores the versatility and adaptability of PD-US techniques across varying model complexities, highlighting its potential for broader clinical diagnostic applications.

6.2.3 Technique Adaptations and Challenges

While both small and large animal studies have underscored PD-US's utility in perfusion imaging, they also reveal the nuances of adapting the technique to different models. Small animal studies benefit from high-resolution imaging capabilities but are limited by the depth of penetration. Conversely, large animal models address depth penetration but face challenges in achieving the high-resolution images possible in small animals. Furthermore, the studies emphasize the importance of minimizing movement artifacts through limb restraint and probe stabilization, which are crucial for accurate perfusion measurement.

6.3 Assessing Endothelial Functions through Reactive Hyperemia

The innovative application of PD-US in assessing endothelial functions through reactive hyperemia has introduced a non-invasive, relatively precise method for evaluating the vascular health of patients with PAD. This research offers a comprehensive view of endothelial responsiveness in both conduit and resistance vessels by integrating the RH-index with FMD measurements. This dual-assessment approach is pivotal for a difficult understanding of vascular health, providing valuable insights into the endothelial dysfunction characteristic of PAD. The RH-index enables a more localized evaluation of endothelial function, offering a promising alternative to traditional methods. This research highlights the potential of PD-US not just for diagnosing PAD but also for monitoring the vascular effects of the disease over time, offering a powerful tool for tracking disease progression and response to treatment. The detailed examination of endothelial function assessment through PD-US signifies a major advancement in non-invasive vascular imaging, setting the stage for more targeted and effective PAD management strategies.

6.4 Future Work

The culmination of this thesis marks a significant advancement in the field of non-invasive vascular imaging, particularly in the management and understanding of PAD. Through the development and meticulous validation of advanced spatial registration and SVD clutter filtering techniques, this work has significantly enhanced the precision and applicability of PD-US imaging. The exploration of PD-US across both small and large animal models has not only demonstrated the technique's versatility and adaptability but also its potential to bridge the gap between preclinical research and clinical practice. Furthermore, the application of PD-US in assessing endothelial function via reactive hyperemia has opened new avenues for comprehensive

vascular health evaluation, providing a non-invasive, relative tool for monitoring PAD progression and treatment efficacy. As we look to the future, the insights gained from this research hold the promise of transforming PAD diagnostics and treatment, moving towards more personalized, non-invasive, and effective management strategies. The potential of PD-US to revolutionize vascular medicine is vast, paving the way for improved patient outcomes and advancing our understanding of vascular diseases.

References

[1] U. O. Abaraogu, E. F. Ezenwankwo, P. M. Dall, and C. A. Seenan, "Living a burdensome and demanding life: A qualitative systematic review of the patients' experiences of peripheral arterial disease," *PLoS One*, vol. 13, no. 11, e0207456, 2018. DOI: 10.1371/journal.pone.0207456. [Online]. Available: https://doi.org/10.1371/journal.pone.0207456.

[2] M. H. Criqui and V. Aboyans, "Epidemiology of peripheral artery disease," *Circ. Res.*, vol. 116, pp. 1509–1526, 2015. DOI: 10.1161/CIRCRESAHA.116.303849. [Online]. Available: https://doi.org/10.1161/CIRCRESAHA.116.303849.

[3] P. W. Fok and P. Lanzer, "Media sclerosis drives and localizes atherosclerosis in peripheral arteries," *PLoS One*, vol. 13, no. 10, e0205599, 2018. DOI: 10.1371/journal.pone.0205599. [Online]. Available: https://doi.org/10.1371/journal.pone.0205599.

[4] A. T. Hirsch, L. Hartman, R. J. Town, and B. A. Virnig, "National health care costs of peripheral arterial disease in the medicare population," *Vasc Med*, vol. 13, no. 3, pp. 209–15, 2008. DOI: 10.1177/1358863X08089277. [Online]. Available: https://doi.org/10.1177/1358863X08089277.

[5] F. G. Fowkes, D. Rudan, I. Rudan, V. Aboyans, J. O. Denenberg, and M. M. McDermott, "Comparison of global estimates of prevalence and risk factors for peripheral artery disease in 2000 and 2010: A systematic review and analysis," *Lancet*, vol. 382, pp. 1329–1340, 2013.

[6] A. W. Gardner and A. Afaq, "Management of lower extremity peripheral arterial disease," *J. Cardiopulm. Rehabil. Prev.*, vol. 28, pp. 349–355, 2008.

[7] A. B. Newman, K. Sutton-Tyrrell, G. H. Rutan, J. Locher, and L. H. Kuller, "Lower extremity arterial disease in elderly subjects with systolic hypertension," *J. Clin. Epidemiol.*, vol. 44, pp. 15–20, 1991.

[8] S. Misra and et al., "C: A scientific statement from the american heart association," *Circulation*, vol. 140, no. 12, e657–e672, 2019.

[9] K. Senda, T. Miura, T. Kato, *et al.*, "Association of the prognosis of ankle-brachial index improvement one year following endovascular therapy in patients with peripheral artery disease: Data from the i-pad nagano registry," *Internal Medicine*, vol. 60, no. 13, pp. 1999–2006, 2021. [Online]. Available: https://www.jstage.jst.go.jp/article/internalmedicine/60/13/60_6117-20/_article/-char/en.

[10] R. Stein, I. Hriljac, J. L. Halperin, S. M. Gustavson, V. Teodorescu, and J. W. Olin, "Limitation of the resting ankle-brachial index in symptomatic patients with peripheral arterial disease," *Vasc Med*, vol. 11, no. 1, pp. 29–33, Feb. 2006. DOI: 10.1191/1358863x06vm663oa.

[11] J. Allen and K. Howell, "Microvascular imaging: Techniques and opportunities for clinical physiological measurements," *Physiol. Meas.*, vol. 35, no. 7, R91–R141, 2014.

[12] O. Mironov, R. Zener, N. Eisenberg, K. T. Tan, and G. Roche-Nagle, "Real-time quantitative measurements of foot perfusion in patients with critical limb ischemia," *Vasc. Endovascular Surg.*, vol. 53, no. 4, pp. 310–315, 2019.

[13] M. R. Stacy, W. Zhou, and A. J. Sinusas, "Radiotracer imaging of peripheral vascular disease," *J. Nucl. Med. Technol.*, vol. 43, no. 3, pp. 185–192, 2015.

[14] O. A. Gimnich, J. Singh, J. Bismuth, D. J. Shah, and G. Brunner, "Magnetic resonance imaging-based modeling of microvascular perfusion in patients with peripheral artery disease," *J. Biomech.*, vol. 93, pp. 147–158, 2019.

[15] T. Nguyen and B. P. Davidson, "Contrast enhanced ultrasound perfusion imaging in skeletal muscle," *J. Cardiovasc Imaging*, vol. 27, no. 3, pp. 163–177, 2019.

[16] C. Huang, P. Song, P. Gong, J. D. Trzasko, A. Manduca, and S. Chen, "Debiasing-based noise suppression for ultrafast ultrasound microvessel imaging," *IEEE Trans. Ultrason. Ferroelectr. Freq. Control*, vol. 66, no. 8, pp. 1281–1291, 2019.

[17] A. Humeau, W. Steenbergen, H. Nilsson, and T. Strömberg, "Laser doppler perfusion monitoring and imaging: Novel approaches," *Medical & Biological Engineering & Computing*, vol. 45, no. 5, pp. 421–435, 2007.

[18] C. Gallippi and G. Trahey, "Adaptive clutter filtering via blind source separation for two-dimensional ultrasonic blood velocity measurement," *Ultrason. Imaging*, vol. 24, no. 4, pp. 193–214, 2002.

[19] S. Bjærum, H. Torp, and K. Kristoffersen, "Clutter filters adapted to tissue motion in ultrasound color flow imaging," *IEEE Transactions on Ultrasonics Ferroelectrics and Frequency Control*, vol. 49, no. 6, pp. 693–704, 2002.

[20] A. C. Yu and L. Lovstakken, "Eigen-based clutter filter design for ultrasound color flow imaging: A review," *IEEE Transactions on Ultrasonics Ferroelectrics and Frequency Control*, vol. 57, no. 5, pp. 1096–1111, 2010.

[21] L. A. Ledoux, P. J. Brands, and A. P. Hoeks, "Reduction of the clutter component in doppler ultrasound signals based on singular value decomposition: A simulation study," *Ultrasonic Imaging*, vol. 19, no. 1, pp. 1–18, 1997.

[22] L. Løvstakken, S. Bjaerum, K. Kristoffersen, R. Haaverstad, and H. Torp, "Real-time adaptive clutter rejection filtering in color flow imaging using power method iterations," *IEEE Transactions on Ultrasonics Ferroelectrics and Frequency Control*, vol. 53, no. 9, pp. 1597–1608, 2006.

[23] D. E. Kruse and K. W. Ferrara, "A new high resolution color flow system using an eigendecomposition-based adaptive filter for clutter rejection," *IEEE Transactions on Ultrasonics Ferroelectrics and Frequency Control*, vol. 49, no. 10, pp. 1384–1399, 2002.

[24] M. F. Insana, B. Dai, S. Babaei, and C. K. Abbey, "Combining spatial registration with clutter filtering for power-doppler imaging in peripheral perfusion applications," *IEEE Trans Ultrason Ferroelectr Freq Control*, vol. 69, no. 12, pp. 3243–3254, 2022. DOI: 10.1109/TUFFC.2022.3211469.

[25] J. Tierney, C. Coolbaugh, T. Towse, and B. Byram, "Adaptive clutter demodulation for noncontrast ultrasound perfusion imaging," *IEEE Trans Med Imaging*, vol. 36, pp. 1979–91, 2017.

[26] M. W. Kim, Y. Zhu, J. Hedhli, W. L. Dobrucki, and M. F. Insana, "Multi-dimensional clutter filter optimization for ultrasonic perfusion imaging," *IEEE Trans Ultrason Ferroelectr Freq Control*, vol. 65, pp. 2020–9, 2018.

[27] C. Demençe, T. Deffieux, M. Pernot, B. F. Osmanski, V. Biran, and J. L. Gennisson, "Spatiotemporal clutter filtering of ultrafast ultrasound data highly increases doppler and ultrasound sensitivity," *IEEE Trans Med Imaging*, vol. 34, pp. 2271–85, 2015.

[28] B. Dai, S. Babaei, C. K. Abbey, and M. F. Insana, "Registration methods in power doppler ultrasound for peripheral perfusion imaging," in *Medical Imaging 2022: Ultrasonic Imaging and Tomography*, vol. 12038, 2022, 120380F. DOI: 10.1117/12.2612640.

[29] C. K. Abbey, N. Q. Nguyen, and M. F. Insana, "Effects of frequency and bandwidth on diagnostic information transfer in ultrasonic b-mode imaging," *IEEE Transactions on Ultrasonics, Ferroelectrics, and Frequency Control*, vol. 59, no. 6, pp. 1115–1126, 2012. DOI: 10.1109/TUFFC.2012.2301.

[30] R. Zemp, C. Abbey, and M. Insana, "Linear system models for ultrasonic imaging: Application to signal statistics," *IEEE Transactions on Ultrasonics, Ferroelectrics, and Frequency Control*, vol. 50, no. 6, pp. 642–654, 2003. DOI: 10.1109/TUFFC.2003.1238898.

[31] E. Franceschini, F. Yu, F. Destrempes, and G. Cloutier, "Ultrasound characterization of red blood cell aggregation with intervening attenuating tissue-mimicking phantoms," *Journal of the Acoustical Society of America*, vol. 127, no. 2, pp. 1104–1115, 2010. DOI: 10.1121/1.3290983.

[32] K. Topp and W. O. Jr, "Anisotropy of ultrasonic propagation and scattering properties in fresh rat skeletal muscle in vitro," *Journal of the Acoustical Society of America*, vol. 107, no. 2, pp. 1027–1033, 2000. DOI: 10.1121/1.428328.

[33] J. Lagarias, J. A. Reeds, M. H. Wright, and P. E. Wright, "Convergence properties of the nelder-mead simplex method in low dimensions," *SIAM Journal on Optimization*, vol. 9, no. 1, pp. 112–147, 1998.

[34] C. Hoerig, J. Ghaboussi, and M. Insana, "Data-driven elasticity imaging using cartesian neural network constitutive models and the autoprogressive method," *IEEE Trans. Med. Imaging*, vol. 38, no. 5, pp. 1150–1160, 2019.

[35] R. Wagner, M. Insana, and S. Smith, "Fundamental correlation lengths of coherent speckle in medical ultrasonic images," *IEEE Trans. Ultrason. Ferro. Freq. Control*, vol. 35, no. 1, pp. 34–44, 1988.

[36] M. F. Insana, Y. Zhu, S. Babaei, D. M. Almora, L. W. Dobrucki, and C. K. Abbey, "Clutter filtering strategies for peripheral muscle perfusion imaging using ultrasound," in *Medical Imaging 2021: Ultrasonic Imaging and Tomography*, B. C. Byram and N. V. Ruiter, Eds., vol. 11602, International Society for Optics and Photonics (SPIE), 2021, pp. 115–131.

[37] S. Babaei, B. Dai, C. K. Abbey, Y. Ambreen, W. L. Dobrucki, and M. F. Insana, "Monitoring muscle perfusion in rodents during short-term ischemia using power doppler ultrasound," *Ultrasound in Medicine & Biology*, vol. 49, no. 6, pp. 1465–1475, 2023, ISSN: 0301-5629. DOI: 10.1016/j.ultrasmedbio.2023.02.013. [Online]. Available: https://www.sciencedirect.com/science/article/pii/S0301562923000650.

[38] R. A. Brenes, C. C. Jadlowiec, M. Bear, P. Hashim, C. D. Protack, X. Li, *et al.*, "Toward a mouse model of hind limb ischemia to test therapeutic angiogenesis," *J Vasc Surg*, vol. 56, pp. 1669–1679, 2012.

[39] D. Briers, D. D. Duncan, E. Hirst, S. J. Kirkpatrick, M. Larsson, W. Steenbergen, *et al.*, "Laser speckle contrast imaging: Theoretical and practical limitations," *J Biomed Opt*, vol. 18, p. 066 018, 2013.

[40] J. Hedhli, M. Kim, H. J. Knox, J. A. Cole, T. Huynh, M. Schuelke, *et al.*, "Imaging the landmarks of vascular recovery," *Theranostics*, vol. 10, pp. 1733–1745, 2020.

[41] J. P. H. Neale, J. T. Pearson, K. N. Thomas, H. Tsuchimochi, H. Hosoda, M. Kojima, *et al.*, "Dysregulation of ghrelin in diabetes impairs the vascular reparative response to hindlimb ischemia in a mouse model: Clinical relevance to peripheral artery disease," *Sci Rep*, vol. 10, p. 13 651, 2020, Erratum in: Sci Rep 2020;10:17556.

[42] R. Rosenberry and M. D. Nelson, "Reactive hyperemia: A review of methods, mechanisms, and considerations," *Am J Physiol Regul Integr Comp Physiol*, vol. 318, R605–18, 2020.

[43] T. Kochi, Y. Imai, A. Takeda, Y. Watanabe, S. Mori, M. Tachi, *et al.*, "Characterization of the arterial anatomy of the murine hindlimb: Functional role in the design and understanding of ischemia models," *PLoS One*, vol. 8, e84047, 2013.

[44] D. Celermajer, K. Sorensen, V. Gooch, *et al.*, "Non-invasive detection of endothelial dysfunction in children and adults at risk of atherosclerosis," *The Lancet*, vol. 340, pp. 1111–1115, 1992.

[45] K. Goto and T. Kitazono, "Endothelium-dependent hyperpolarization (edh) in diabetes: Mechanistic insights and therapeutic implications," *International Journal of Molecular Sciences*, vol. 20, p. 3737, 2019.

[46] T. Kato, "Which is the best method in clinical practice for assessing improvement in vascular endothelial function after successful smoking cessation—flow-mediated dilation (fmd) or reactive hyperemic peripheral arterial tonometry (rh-pat)?" *Hypertens Res*, vol. 44, pp. 120–121, 2021.

[47] P. Vanhoutte, H. Shimokawa, M. Feletou, and E. Tang, "Endothelial dysfunction and vascular disease—a 30th-anniversary update," *Acta Physiologica*, vol. 219, pp. 22–96, 2017.

[48] A. Huang, A. Silver, E. Shvenke, D. Schopfer, E. Jahangir, M. Titas, *et al.*, "Predictive value of reactive hyperemia for cardiovascular events in patients with peripheral arterial disease undergoing vascular surgery," *Arteriosclerosis, Thrombosis, and Vascular Biology*, vol. 27, pp. 2113–2119, 2007.

[49] N. M. Hamburg, J. Palmisano, M. G. Larson, L. M. Sullivan, B. T. Lehman, R. S. Vasan, *et al.*, "Relation of brachial and digital measures of vascular function in the community: The framingham heart study," *Hypertension*, vol. 57, pp. 390–396, 2011.

[50] Z. W. Zhuang, L. W. Dobrucki, and R. Ju, "Multi-modality imaging of angiogenesis and arteriogenesis of swimming-induced nitric oxide protection against hindlimb ischemia," *Circulation*, vol. 120, S361, 2009, Abstract Only.

[51] P. Robinet, D. M. Milewicz, L. A. Cassis, N. J. Leeper, H. S. Lu, and J. D. Smith, "Consideration of sex differences in design and reporting of experimental arterial pathology studies—statement from atvb council," *Arterioscler Thromb Vasc Biol*, vol. 38, pp. 292–303, 2018.

[52] T. Yokoyama, Y. Tosa, K. Kadomatsu, K. Sato, and Y. Hosaka, "A novel approach for preventing the development of persistent vasospasms after microsurgery for the extremities: Intermittent topical lidocaine application," *Journal of Reconstructive Microsurgery*, vol. 26, pp. 79–85, 2010.

[53] J. Jernbeck and U. Samuelson, "Effects of lidocaine and calcitonin gene-related peptide (cgrp) on isolated human radial arteries," *Journal of Reconstructive Microsurgery*, vol. 9, pp. 361–365, 1993.

[54] D. Briers, "Video capability revives interest in laser method," *Optics & Laser Europe*, vol. 147, pp. 15–16, 2007.

[55] E. Franceschini, F. Yu, F. Destrempes, and G. Cloutier, "Ultrasound characterization of red blood cell aggregation with intervening attenuating tissue-mimicking phantoms," *J Acoust Soc Am*, vol. 127, pp. 1104–1115, 2010.

[56] J. Rubin, R. Bude, P. Carson, R. Bree, and R. Adler, "Power doppler US: A potentially useful alternative to mean frequency-based color doppler US," *Radiology*, vol. 190, pp. 853–856, 1994.

[57] M. Kim, C. Abbey, J. Hedhli, W. Dobrucki, and M. Insana, "Expanding acquisition and clutter filter dimensions for improved perfusion sensitivity," *IEEE Trans Ultrason Ferroelectr Freq Control*, vol. 64, pp. 1429–1438, 2017.

[58] L. Azzi, M. El-Alfy, C. Martel, and F. Labrie, "Gender differences in mouse skin morphology and specific effects of sex steroids and dehydroepiandrosterone," *J Invest Dermatol*, vol. 124, pp. 22–27, 2005.

[59] W. Song, L. Zhou, K. Kot, H. Fan, J. Han, and J. Yi, "Measurement of flow-mediated dilation of mouse femoral artery in vivo by optical coherence tomography," *J Biophotonics*, vol. 11, e201800053, 2018.

[60] D. Schuler, R. Sansone, T. Freudenberger, A. Rodriguez-Mateos, G. Weber, and e. a. Momma TY, "Measurement of endothelium-dependent vasodilation in mice—brief report," *Arterioscler Thromb Vasc Biol*, vol. 34, pp. 2651–7, 2014.

[61] F. Leo, T. Krenz, G. Wolff, M. Weidenbach, C. Heiss, and e. a. Kelm M, "Assessment of tissue perfusion and vascular function in mice by scanning laser doppler perfusion imaging," *Biochem Pharmacol*, vol. 176, p. 113 893, 2020.

[62] S. Doshi, K. Naka, N. Payne, C. Jones, M. Ashton, and e. a. Lewis MJ, "Flow-mediated dilatation following wrist and upper arm occlusion in humans: The contribution of nitric oxide," *Clin Sci (Lond)*, vol. 101, pp. 629–635, 2001.

[63] S. Babaei, W. L. Dobrucki, and M. F. Insana, "Power-doppler ultrasonic imaging of peripheral perfusion in diabetic mice," *IEEE Transactions in Biomedical Engineering*,

[64] K. Fukumoto, Y. Takemoto, N. Norioka, *et al.*, "Predictors of the effects of smoking cessation on the endothelial function of conduit and digital vessels," *Hypertension Research*, vol. 44, pp. 63–70, 2021.

[65] I. Hoefer, N. van Royen, I. Buschmann, J. Piek, and W. Schaper, "Time course of arteriogenesis following femoral artery occlusion in the rabbit," *Cardiovascular Research*, vol. 49, pp. 609–617, 2001.

[66] S. Iyer and B. Annex, "Therapeutic angiogenesis for peripheral artery disease: Lessons learned in translational science," *Journal of the American College of Cardiology: Basic to Translational Science*, vol. 2, pp. 503–512, 2017.

[67] S. Grundmann, J. Piek, G. Pasterkamp, and I. Hoefer, "Arteriogenesis: Basic mechanisms and therapeutic stimulation," *European Journal of Clinical Investigation*, vol. 37, no. 10, pp. 755–766, 2007.

[68] H. Baribault, "Mouse models of type ii diabetes mellitus in drug discovery," *Methods in Molecular Biology*, vol. 1438, pp. 153–175, 2016.

[69] R. Burcelin, V. Crivelli, A. Dacosta, A. Roy-Tirelli, and B. Thorens, "Heterogeneous metabolic adaptation of c57bl/6j mice to high-fat diet," *American Journal of Physiology - Endocrinology and Metabolism*, vol. 282, no. 4, E834–E842, 2002.

[70] J. Rozman, B. Rathkolb, S. Neschen, *et al.*, "Glucose tolerance tests for systematic screening of glucose homeostasis in mice," *Current Protocols in Mouse Biology*, vol. 5, pp. 65–84, 2015. DOI: 10.1002/9780470942390.mo140111.

[71] A. King, "The use of animal models in diabetes research," *British Journal of Pharmacology*, vol. 166, no. 3, pp. 877–894, 2012.

[72] T. Reuter, "Diet-induced models for obesity and type 2 diabetes," *Drug Discovery Today: Disease Models*, vol. 4, no. 1, pp. 3–8, 2007.

[73] S. Colberg, R. Sigal, J. Yardley, *et al.*, "Physical activity/exercise and diabetes: A position statement of the american diabetes association," *Diabetes Care*, vol. 39, no. 11, pp. 2065–2079, 2016.

[74] G. E. Box and D. R. Cox, "An analysis of transformations," *Journal of the Royal Statistical Society: Series B (Methodological)*, vol. 26, no. 2, pp. 211–243, 1964.

[75] J. T. Belcik, B. P. Davidson, T. Foster, *et al.*, "Contrast-enhanced ultrasound assessment of impaired adipose tissue and muscle perfusion in insulin-resistant mice," *Circ. Cardiovasc. Imaging*, vol. 8, no. 4, 2015. DOI: 10.1161/CIRCIMAGING.114.002684.

[76] C. Emanueli, A. Caporali, N. Krankel, B. Cristofaro, S. Van Linthout, and P. Madeddu, "Type-2 diabetic lepr(db/db) mice show a defective microvascular phenotype under basal conditions and an impaired response to angiogenesis gene therapy in the setting of limb ischemia," *Frontiers in Bioscience*, vol. 12, pp. 2003–2012, 2007. DOI: 10.2741/2205.

[77] R. P. Schnall, J. Sheffy, and T. Penzel, "Peripheral arterial tonometry–pat technology," *Sleep Medicine Reviews*, vol. 61, p. 101 566, 2022.

[78] U. A. Okonkwo and L. A. DiPietro, "Diabetes and wound angiogenesis," *International Journal of Molecular Sciences*, vol. 18, no. 7, p. 1419, 2017. DOI: 10.3390/ijms18071419.

[79] D. J. Green, J. H. Walsh, A. Maiorana, V. Burke, R. R. Taylor, and J. G. O'Driscoll, "Comparison of resistance and conduit vessel nitric oxide-mediated vascular function in vivo: Effects of exercise training," *Journal of Applied Physiology*, vol. 97, pp. 749–755, 2004.

[80] J. E. Farber, H. Zhang, R. M. Lassance-Soares, *et al.*, "Aging causes collateral rarefaction and increased severity of ischemic injury in multiple tissues," *Arteriosclerosis, Thrombosis, and Vascular Biology*, vol. 31, no. 8, pp. 1748–1756, 2011.

[81] E. Tajima, M. Sakuma, S. Tokoi, *et al.*, "The comparison of endothelial function between conduit artery and microvasculature in patients with coronary artery disease," *Cardiology Journal*, vol. 27, no. 1, pp. 38–46, 2020.

[82] J. A. Suwaidi, S. Hamasaki, S. T. Higano, R. A. Nishimura, D. R. J. Holmes, and A. Lerman, "Long-term follow-up of patients with mild coronary artery disease and endothelial dysfunction," *Circulation*, vol. 101, no. 9, pp. 948–954, 2000.

[83] J. D. Allen, T. Giordano, and C. G. Kevil, "Nitrite and nitric oxide metabolism in peripheral artery disease," *Nitric Oxide*, vol. 26, no. 4, pp. 217–222, 2012.

[84] J. Liu, J. Wang, Y. Jin, H. J. Roethig, and M. Unverdorben, "Variability of peripheral arterial tonometry in the measurement of endothelial function in healthy men," *Clinical Cardiology*, vol. 32, no. 12, pp. 700–704, 2009.

[85] A. J. Flammer, T. Anderson, D. S. Celermajer, *et al.*, "The assessment of endothelial function: From research into clinical practice," *Circulation*, vol. 126, no. 6, pp. 753–767, 2012.

[86] Y. Yang, G. Tang, J. Yan, *et al.*, "Cellular and molecular mechanisms regulating blood flow recovery in acute versus gradual femoral artery occlusion are distinct in the mouse," *J. Vasc. Surg.*, vol. 48, no. 6, pp. 1546–1558, 2008.

[87] M. L. Mehl, A. E. Kyles, E. M. Hardie, *et al.*, "Evaluation of ameroid ring constrictors for treatment of single extrahepatic portosystemic shunts in dogs: 168 cases (1995-2001)," *J. Am. Vet. Med. Assoc.*, vol. 226, no. 12, pp. 2020–2030, 2005.

[88] G. B. Hunt, W. T. Culp, K. N. Mayhew, P. Mayhew, M. A. Steffey, and A. Zwingenberger, "Evaluation of in vivo behavior of ameroid ring constrictors in dogs with congenital extrahepatic portosystemic shunts using computed tomography," *Vet. Surg.*, vol. 43, no. 7, pp. 834–842, 2014.

[89] S. M. Hansen, L. E. Schepers, R. Pratihar, *et al.*, "Hemodynamic assay of hind limb in multiple animal models," *Mil. Med.*, vol. 186, no. Suppl 1, pp. 351–357, Jan. 2021.

[90] I. R. Buschmann, M. Voskuil, N. van Royen, *et al.*, "Invasive and non-invasive evaluation of spontaneous arteriogenesis in a novel porcine model for peripheral arterial obstructive disease," *Atherosclerosis*, vol. 167, no. 1, pp. 33–43, 2003.

[91] C. A. Long, L. H. Timmins, P. Koutakis, *et al.*, "An endovascular model of ischemic myopathy from peripheral arterial disease," *J. Vasc. Surg.*, vol. 66, no. 3, pp. 891–901, 2017.

[92] M. F. Besancon, A. E. Kyles, S. M. Griffey, and C. R. Gregory, "Evaluation of the characteristics of venous occlusion after placement of an ameroid constrictor in dogs," *Vet. Surg.*, vol. 33, no. 6, pp. 597–605, 2004.

[93] J. C. Vogt, D. J. J. Krahwinkel, R. M. Bright, G. B. Daniel, R. L. Toal, and B. Rohrbach, "Gradual occlusion of extrahepatic portosystemic shunts in dogs and cats using the ameroid constrictor," *Vet. Surg.*, vol. 25, pp. 495–502, 1996.